Investigating Parton Energy Loss in the Quark-Gluon Plasma with Jet-hadron Correlations and Jet Azimuthal Anisotropy at STAR

A Dissertation
Presented to the Faculty of the Graduate School
of
Yale University
in Candidacy for the Degree of
Doctor of Philosophy

by
Alice Elisabeth Ohlson

Dissertation Director: John Harris

December 2013

Abstract

Investigating Parton Energy Loss in the Quark-Gluon Plasma with Jet-hadron Correlations and Jet Azimuthal Anisotropy at STAR

Alice Elisabeth Ohlson

2013

In high-energy collisions of gold nuclei at the Relativistic Heavy Ion Collider (RHIC) and of lead nuclei at the Large Hadron Collider (LHC), a new state of matter known as the Quark-Gluon Plasma (QGP) is formed. This strongly-coupled, deconfined state of quarks and gluons represents the high energy-density limit of quantum chromodynamics. The QGP can be probed by high-momentum quarks and gluons (collectively known as partons) that are produced in hard scatterings early in the collision. The partons traverse the QGP and fragment into collimated "jets" of hadrons. Studies of parton energy loss within the QGP, or medium-induced jet quenching, can lead to insights into the interactions between a colored probe (a parton) and the colored medium (the QGP).

Two analyses of jet quenching in relativistic heavy ion collisions are presented here. In the jet-hadron analysis, the distributions of charged hadrons with respect to the axis of a reconstructed jet are investigated as a function of azimuthal angle and transverse momentum (p_{T}). It is shown that jets that traverse the QGP are softer (consisting of fewer high-p_{T} fragments and more low-p_{T} constituents) than jets in p+p collisions. There are also indications that the shapes of the distributions of charged hadrons about the jet axis are modified by interactions with the QGP. The results are quantitatively consistent with two models of medium-induced radiative

parton energy loss.

A measurement of jet v_2, defined as the correlation between reconstructed jets and the reaction plane or 2^{nd}-harmonic participant plane (approximated by the 2^{nd}-harmonic event plane), provides information about the medium-induced pathlength-dependence of parton energy loss. The event plane is reconstructed with detectors at forward pseudorapidity in order to reduce the artificial jet – event plane bias, which results from jet fragments being included in the event plane calculation. A non-zero jet v_2 is measured, indicating that more jets are reconstructed with a higher energy in-plane compared to out-of-plane, which demonstrates that the parton energy loss depends on the length of the parton's path through the QGP.

The data analyzed here were collected in $\sqrt{s_{NN}} = 200$ GeV Au+Au and p+p collisions at the STAR detector at RHIC. A novel method for measuring jet v_n is also proposed and tested in simulation.

Acknowledgments

Throughout my educational career and my life so far I have been blessed to have many incredible teachers and mentors, who have all played a part in making me the person I am today. I cannot thank them all here, but it is to them that this thesis is dedicated.

First and foremost, I would like to thank Professors John Harris, Helen Caines, and Jörn Putschke for making the Yale Relativistic Heavy Ion Group such a great environment in which to do research and to learn. To John, my advisor, thank you for being so supportive, for encouraging me to work on cool projects, and for all the opportunities you have given me in the last four years. To Helen, thank you for all of our discussions in which I have learned so much, and for answering all my questions no matter how silly they may have been. To Jörn, thank you for teaching me so much, for guiding me as I learned the ropes in STAR, and for answering all of my many questions with patience. It is thanks to the three of you that, after four years of graduate school, I am a better physicist, a better scientist, and a better person.

I also wish to give many thanks to the members of the Yale Relativistic Heavy Ion Group (past and present), who have made coming into work every day a pleasure: Andrew Adare, Salvatore Aiola, Tomas Aronsson, Stephen Baumgart, Diego Caballero Orduna, Elena Bruna, Megan Connors, Raymond Ehlers, Mark Heinz, Ben Hicks, Per Thomas Hille, Stephen Horvat, Anders Knospe, Rongrong Ma, Christine Nattrass, Hanseul Oh, Rosi Reed, Tim Schuster, Nikolai Smirnov, and Thomas Ullrich. Also thanks to my friends in the physics department, who have made grad school so much fun: Tomomi Sunayama, Katrina Sliwa, Dustin Ngo, Genna Voronov, and many others.

I would like to thank my collaborators in STAR who have contributed so much

to my education in this field, particularly the members of the jet-like correlations PWG – led by the convenors Jörn Putschke, Fuqiang Wang, Saskia Mioduszewski, and Lanny Ray, and the EMC^2 group – especially Will Jacobs and Justin Stevens.

I have had many helpful physics discussions about flow and v_n with Paul Sorensen, Art Poskanzer, and Sergei Voloshin, and I am very grateful for their thoughtful suggestions on the jet v_n method paper. The jet-hadron paper was improved thanks to the hard work by the members of the GPC: Carl Gagliardi, Saskia Mioduszewski, Aihong Tang, Kolja Kauder, and Jerry Hoffmann, as well as Xin Dong. Also, many thanks to Thorsten Renk for all the conversations that we have had about jet theory (among other topics). Finally, I would like to thank the members of my thesis committee: Professors John Harris, Helen Caines, Sarah Demers, and Yoram Alhassid, and my outside reader, Professor Sevil Salur, for reading my thesis and offering their valuable comments for improvements.

In middle school, high school, and college, I was fortunate to have teachers who made science and math fun, exciting, and accessible. Early on, Mrs. Lucia, Mr. Leonard, Mr. Latham, and Dr. Dell actively encouraged me to pursue these subjects. I would not be where I am today without Mr. Latham, who first made me love particle physics, and Prof. Matthews, who got me started in nuclear physics. I also owe a lot to Prof. Becker, who taught me how to give talks, an absolutely crucial skill. I would also like to thank my first scientific mentor, Dr. Michelle Shinn, who (among other things) gave me the best piece of advice for a young scientist: "Remember to stay humble before Nature's wonders. Work to learn a few!"

Finally, I would like to thank my parents, who have supported all my wildest hopes and dreams every step of the way. Without their infinite love none of this would have been possible. It has been a wonderful ride so far, and I cannot wait to see what the future holds!

Contents

List of Figures

List of Tables

Chapter 1

Introduction

In high-energy collisions of heavy nuclei, a hot and dense medium of deconfined quarks and gluons is formed, known as the Quark-Gluon Plasma (QGP). Nuclear matter can be studied under extreme conditions in Au+Au collisions at a center-of-mass energy per nucleon-nucleon pair of $\sqrt{s_{\rm NN}} = 200$ GeV in the Relativistic Heavy Ion Collider (RHIC). The Solenoidal Tracker at RHIC (STAR) detector is designed to measure charged and neutral particles produced in collisions of heavy ions (Au+Au and other species) as well as in p+p and d+Au collisions. The properties of the QGP can be studied by using high-momentum quarks and gluons (collectively known as partons) as probes of the medium. By comparing the fragmentation of partons into jets in Au+Au and p+p collisions, and by investigating the correlations of jets with the geometry of the medium, we can learn about parton interactions in the QGP.

1.1 Quantum Chromodynamics

The theory of the strong interaction, quantum chromodynamics (QCD), is an non-abelian gauge field theory which exhibits both confinement and asymptotic freedom [1, 2]. In strong interactions, the coupling constant (α_s) depends on Q^2, the mo-

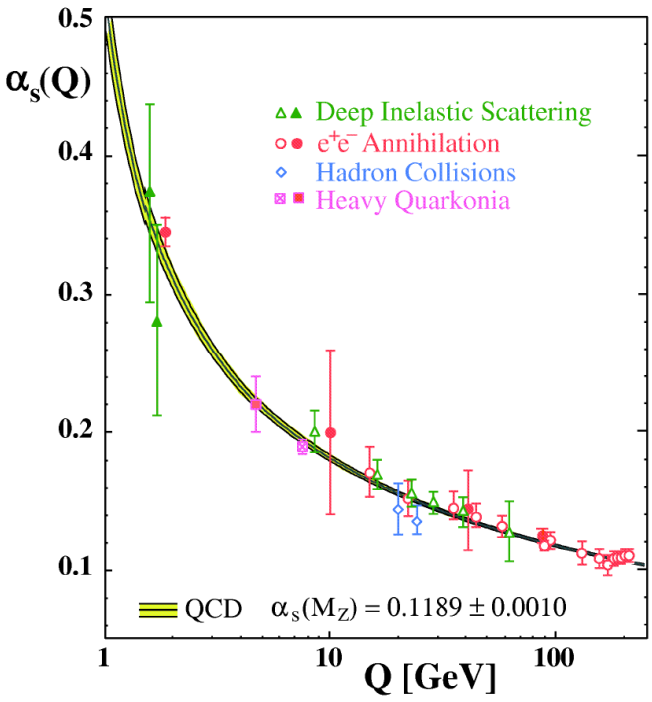

Figure 1.1: The running strong coupling constant, α_s [3].

mentum transferred. The behavior of α_s described within QCD is shown in Fig. 1.1, along with measurements of α_s from multiple experiments.

In the "confinement" regime at low Q^2, α_s is large, indicating that at low momentum and large distance scales, quarks are tightly bound together. However, at high Q^2 (large momentum transfer, probing small length scales), α_s approaches zero, and QCD asymptotically approaches a free field theory. This behavior of α_s accounts for two seemingly-contradictory observations:

1. Free quarks are never observed in nature, instead they are always bound into hadrons. In particular, they are always found in color-neutral configurations, either in $q\bar{q}$ pairs (mesons) or in qqq or $\bar{q}\bar{q}\bar{q}$ triplets (baryons).

2. Deep-inelastic scattering measurements indicate that the quarks within hadrons behave as free particles [4, 5].

1.2 The Quark-Gluon Plasma

It was proposed that in systems with high nuclear density, quarks will no longer be bound into mesons and baryons. In such an environment, long-range interactions are screened by the high density of color charges. Since short-range interactions in QCD are weak, the partons behave as nearly free particles. One environment in which these high nuclear densities can be achieved is in high energy collisions of heavy nuclei [6].

The transition from confinement to asymptotic freedom defies analytical treatment because QCD is non-perturbative in the low-Q^2 regime. Therefore physical quantities must be obtained from computational methods, such as explicitly evaluating the QCD Lagrangian on a space-time lattice. Lattice QCD (lQCD) calculations show that there is a critical temperature, T_c, where there is a sharp increase in the quantity ε/T^4 (where ε is the energy density and T is the temperature) [7, 8], shown in Figure 1.2. Since this quantity is proportional to the number of degrees of freedom in the system, this result indicates that as T increases nuclear matter undergoes a phase transition to a state in which the relevant degrees of freedom are no longer nucleons but quarks and gluons. While lQCD calculations support the expectation that quarks and gluons are deconfined in high temperature and high density environments, they also show significant deviation from the Stefan-Boltzmann (ideal gas) expectation (as shown in Fig. 1.2). Although the quarks and gluons are not confined into hadrons, there are still sizable strong (non-perturbative) interactions between them.

In heavy ion collisions, the temperature and energy density exceed the lQCD predictions for where the QGP is expected to form. While the values of T_c obtained from lQCD calculations vary depending on modeling methods (i.e. the number of

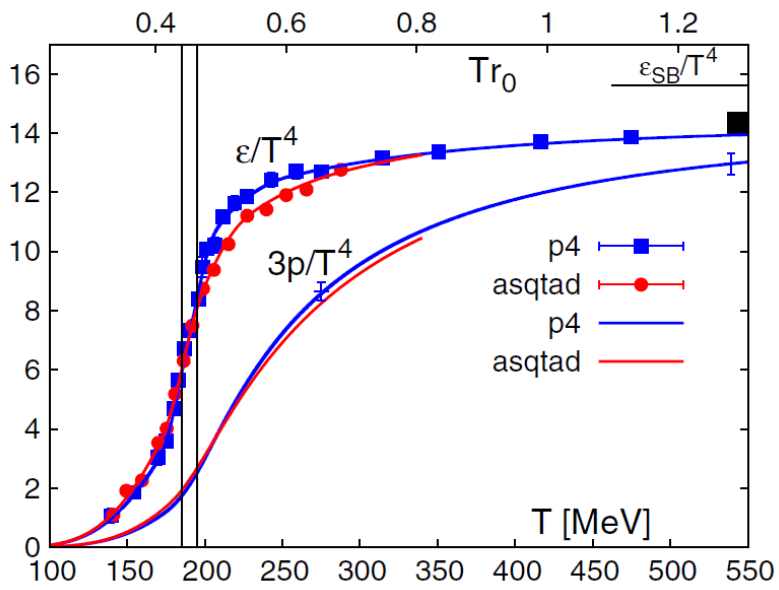

Figure 1.2: A lattice QCD calculation of energy density divided by temperature to the fourth power which indicates a significant increase in the number of degrees of freedom in the hadronic system at a critical temperature $T_c \sim 185-195$ MeV [8]. The Stefan-Boltzmann (ideal, non-interacting gas) limit is marked on the right vertical axis.

quark flavors included, etc.), and are continually being refined as computational techniques improve (see Ref. [9] for a recent review), they are generally believed to be in the region of $185 - 195$ MeV. Measurements of direct photons indicate that a temperature in excess of 220 MeV is achieved in central Au+Au collisions at $\sqrt{s_{\rm NN}} = 200$ GeV, well above the transition from a hadron gas to a QGP [10].

1.3 Jets

In the early stages of heavy ion collisions, hard (high Q^2) scatterings produce back-to-back pairs of partons with high transverse momentum ($p_{\rm T}$). As these partons recoil they fragment into collimated clusters of particles, known as "jets." Since jets originate in high-Q^2 processes, α_s is small and perturbation theory is applicable. Perturbative QCD (pQCD) calculations describe measurements of jet production in

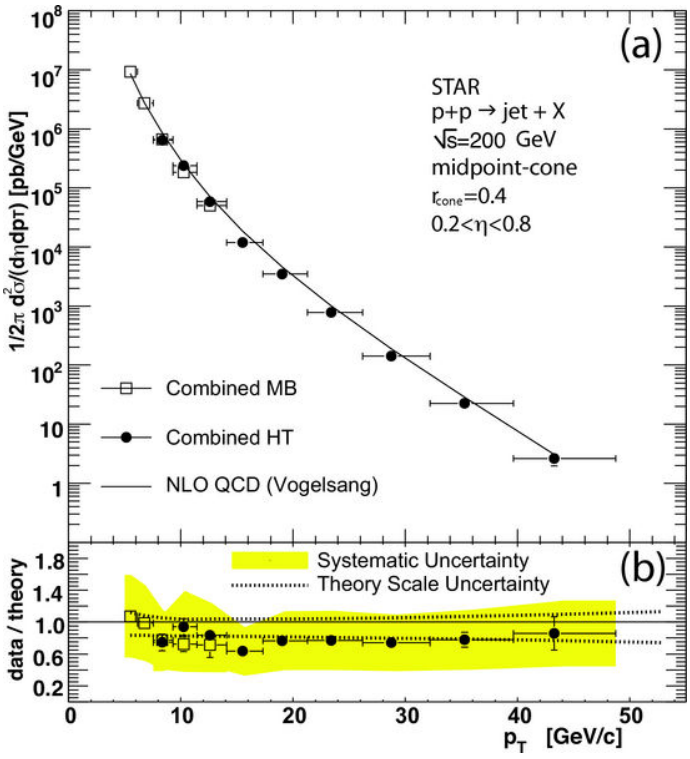

Figure 1.3: The jet cross-section in p+p collisions is described by NLO pQCD over seven orders of magnitude. [12]

elementary collisions (p+p, e^+e^-) with high accuracy [11]. For example, the inclusive jet cross-section was measured in p+p collisions ($p + p \rightarrow \text{jet} + X$) at STAR and compared to a next-to-leading order pQCD calculation, shown in Fig. 1.3 [12]. The result shows excellent agreement over seven orders of magnitude.

The QGP created in heavy ion collisions cannot be studied with conventional probes, such as lasers or particle beams, because of its small size and short lifetime. However, since the production of high-p_{T} partons is well-understood in elementary collisions, they can be used as internally-generated probes of the QGP. By comparing jets in heavy ion collisions with jets in elementary collisions, the interactions of colored probes (partons) with a colored medium (the QGP) can be studied.

1.4 Outline

This thesis will discuss two experimental analyses of parton interactions with the QGP: jet-hadron correlations and jet v_2. Relevant characteristics of the QGP and previous experimental results will be reviewed in Chapter 2. Chapter 3 will give an overview of the RHIC accelerator and the STAR experiment. The jet-hadron correlations analysis and results will be presented in Chapter 4, and the jet v_2 analysis and results in Chapter 5. A new method for calculating jet v_n will be described in Chapter 6. Finally, a summary and conclusions will be offered in Chapter 7.

Chapter 2

Background

2.1 Evolution of a Heavy Ion Collision

In collisions of heavy nuclei accelerated to relativistic speeds, the system evolves through several stages. Prior to the collision, the ions are highly Lorentz-contracted. (For example, at RHIC's top collision energy of $\sqrt{s_{\mathrm{NN}}} = 200$ GeV, gold ions are boosted to 99.995% of the speed of light and are Lorentz-contracted by a factor of $\gamma \sim 100$.) The inter-penetration time is the first ~ 0.3 fm/c of the collision, after which the nucleons that did not interact (known as the "spectators") continue in the direction of the beam, and the remaining energy is deposited into a small volume of space.

For the first ~ 1 fm/c of the collision, the system evolves from a non-equilibrium state to a state with regions of local equilibrium. The strongly-interacting thermally-equilibrated matter that results is the QGP. (Experimental evidence seems to suggest significant thermalization and equilibration throughout the QGP, although these measurements may just be an average over smaller regions of local equilibrium at different temperatures and values of the baryochemical potential. Theoretical de-

scriptions of the mechanisms involved in thermally equilibrating the QGP over short time scales and large regions in phase space are still being developed.) The system continues to interact as it expands and cools over the next $\sim 10 - 15$ fm/c. As the QGP cools and hadronizes (likely passing through some sort of mixed phase in which hadrons and the QGP coexist), it undergoes chemical freeze-out – after which there are no inelastic flavor-changing scatterings – followed by thermal (kinetic) freeze-out – when elastic scatterings between the particles cease. After kinetic freeze-out, the hadrons free-stream to the detectors.

The QGP phase appears to exhibit thermal equilibrium such that statistical quantities (temperature, pressure, etc.) are meaningful, particle production can be described within the Grand Canonical Ensemble [13], and bulk properties of the system can be observed.

2.2 Bulk Dynamics

The majority of particles produced in heavy ion collisions result from the hadronization of the QGP, and are collectively correlated with respect to the initial geometry of the collision in a way that suggests that the QGP exhibits hydrodynamic flow on the parton level.

2.2.1 Collision Geometry & Definitions

Many physical observables in relativistic heavy ion collisions are sensitive to the shape and density profile of the QGP, which are determined by the spatial distribution of the nucleons which interact during the collision (the "participants"). Figure 2.1 shows the participant distributions simulated within a Monte Carlo Glauber model for two collisions with different geometries. The distribution of the participant nu-

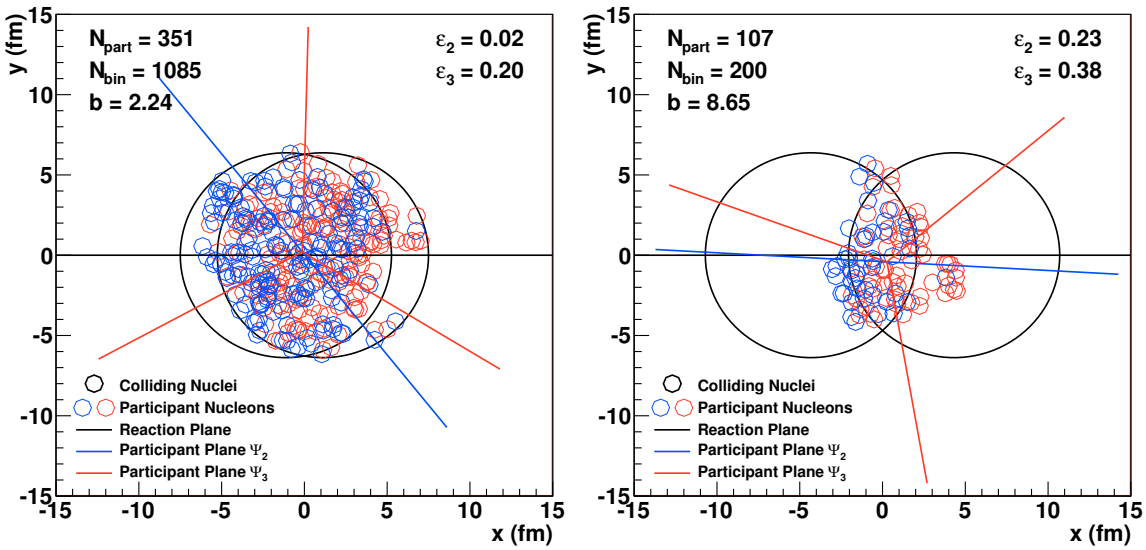

Figure 2.1: Two events from a Monte Carlo Glauber simulation[†] illustrate several of the terms defined in the text. The colliding nuclei are shown in black circles, and the participating (interacting) nucleons from each nucleus are shown as red and blue circles. The left plot shows a central event (from the 0-5% centrality bin) and the right is a more peripheral event (from the 30-40% centrality bin). Straight lines show the orientation of the reaction plane (black), second-order participant plane (blue), and third-order participant plane (red). Also shown are: the number of participating nucleons ($N_{\rm part}$), the number of binary collisions ($N_{\rm bin}$), the impact parameter (b), the eccentricity (ε_2), and the triangularity (ε_3).

cleons is correlated with the "centrality" of the collision, which is determined by the magnitude of the impact parameter of the nucleus-nucleus collision. In "central" collisions, where the impact parameter is small, the geometrical overlap of the colliding nuclei is roughly circular and the number of participants is high. Only a few nucleons participate in "peripheral" collisions, where the impact parameter is large, and the transverse overlap region is more almond-shaped. Centrality is quantified as a percentile of the interaction cross-section, from 0% being the most central to 100% being the most peripheral.

In non-central collisions, the orientation of colliding heavy nuclei can be described

[†]Created with code written and adapted by S. Voloshin, P. Sorensen, and J. Putschke.

by the "reaction plane," which is the plane defined by the impact parameter (the vector connecting the centers of the two nuclei) and the beam direction. However, the positions of the nucleons within each nucleus fluctuate event-to-event, so the participant distribution is not perfectly described by the geometrical overlap of the colliding nuclei. Thus, the geometry of the resultant matter distribution cannot be described by the reaction plane alone. For this reason, the concept of "participant planes" was introduced [14, 15]. The azimuthal angle of the n^{th}-harmonic participant plane is defined by the n^{th}-order axis of symmetry of the participating nucleon distribution. The reaction plane as well as the second- and third-order participant planes are shown in Fig. 2.1.

Due to the almond-shaped geometrical overlap region of the colliding nuclei, in semicentral events the distribution of participant nucleons is roughly elliptical in coordinate space, on average. The minor axis of the ellipse is the 2^{nd}-order participant plane, which is closely aligned with the reaction plane. The 3^{rd}-harmonic participant plane is uncorrelated with the 2^{nd}-harmonic participant and reaction planes [16].

The reaction plane and participant planes are properties of the initial participant distribution and are not directly observable from the final state hadrons that are detected in experiments. The experimental approximations of the reaction plane and participant planes are the n^{th}-order "event planes." Methods for reconstructing the event planes are discussed in Chapters 5 and 6.

2.2.2 Bulk Dynamics – Partonic Elliptic Flow

Since the density profile of the QGP is not azimuthally symmetric, the pressure gradients that build up within the QGP are also anisotropic. Larger pressure gradients along the participant planes boost particles preferentially in the direction of the participant planes, thus converting the initial coordinate-space eccentricity into

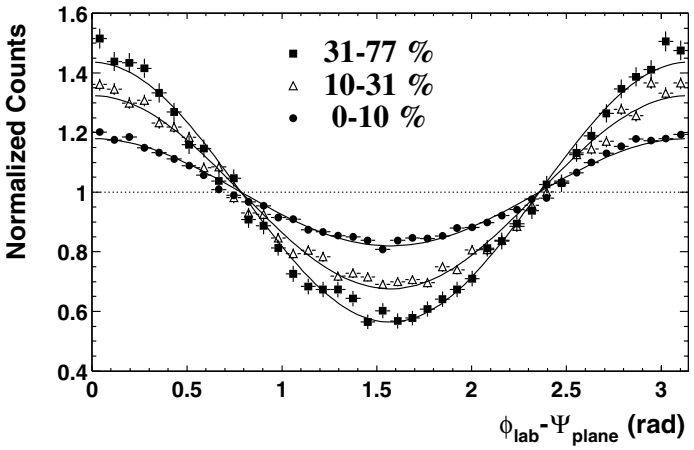

Figure 2.2: The correlation of charged hadrons ($2 < p_{\mathrm{T}} < 6$ GeV/c) with the event plane in three centrality bins [18].

an anisotropy in momentum-space [17]. As a result, more particles are observed to be aligned with the participant planes, and fewer particles are observed out-of-plane. This was demonstrated in the early days of RHIC in the correlation of charged hadrons with the 2$^{\mathrm{nd}}$-harmonic event plane, shown in Fig. 2.2.

The azimuthal angular (ϕ) distribution of the particles can be expanded in Fourier coefficients with respect to the azimuthal angle of the reaction plane (Ψ_{RP}), as shown in Eq. (2.1), or any order participant plane ($\Psi_{\mathrm{PP},m}$), as in Eq. (2.2) [19]:

$$\frac{\mathrm{d}N}{\mathrm{d}\left(\phi - \Psi_{\mathrm{RP}}\right)} \propto 1 + \sum_{n=1}^{\infty} 2v_n \cos\left[n\left(\phi - \Psi_{\mathrm{RP}}\right)\right] \tag{2.1}$$

$$\frac{\mathrm{d}N}{\mathrm{d}\left(\phi - \Psi_{\mathrm{PP},m}\right)} \propto 1 + \sum_{n=1}^{\infty} 2v_n \cos\left[n\left(\phi - \Psi_{\mathrm{PP},m}\right)\right] \tag{2.2}$$

Since the QGP has a predominantly elliptical shape, which is translated to an elliptical distribution in momentum-space by pressure gradients, as discussed above, the $\cos(2(\phi - \Psi_2))$ modulation dominates the particle distribution shown in Fig. 2.2. Therefore the v_2 parameter is dominant compared to the other v_n coefficients, in

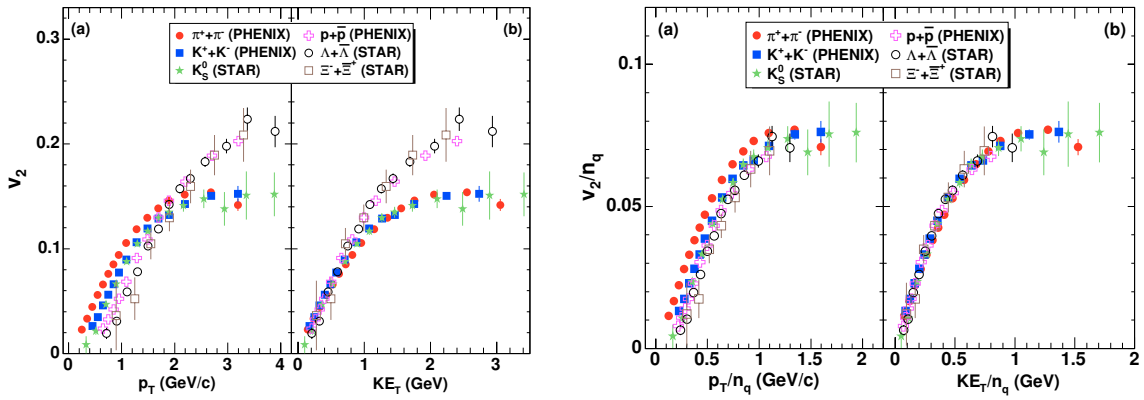

Figure 2.3: $v_2(p_{\mathrm{T}})$ and $v_2(KE_{\mathrm{T}})$ are shown for several particle species (left), and then shown again with all the relevant quantities scaled by the number of constituent quarks (n_q) (right) [26].

all but the most central collisions. Recent theoretical [20, 21, 22] and experimental [23, 24] work has shown that fluctuations in the initial state can also result in nonzero higher-order odd v_n coefficients when calculated with respect to the n^{th}-order participant plane. In particular, v_3 (measured with respect to $\Psi_{\mathrm{PP},3}$) is the most significant v_n coefficient in ultracentral collisions [25], in which the nuclear overlap area is essentially circular but initial state fluctuations give rise to third-harmonic shapes in the initial energy density distribution.

Detailed measurements have been made of v_2 as a function of momentum, centrality, particle species, collision energy, rapidity, etc. (Similar studies of v_3 and higher harmonics are ongoing.) Of particular importance are the results in Fig. 2.3, which show measurements of $v_2(p_{\mathrm{T}})$ and $v_2(KE_{\mathrm{T}})$ for several particle species. At low p_{T}, a mass ordering is observed in $v_2(p_{\mathrm{T}})$. Hydrodynamic behavior driven by pressure gradients would imply that the low-p_{T} behavior of v_2 should scale with the transverse kinetic energy, $KE_{\mathrm{T}} = m_{\mathrm{T}} - m$, and this is observed in the measurement of $v_2(KE_{\mathrm{T}})$. Furthermore $v_2(KE_{\mathrm{T}})$ splits into baryon and meson branches at high-p_{T}. When v_2 and KE_{T} are divided by the number of constituent quarks (n_q) in each hadron species, the results lie on a universal curve. This n_q-scaling was taken as

evidence that the degrees of freedom in the flowing medium in heavy ion collisions are quarks instead of hadrons [26].

2.2.3 The "Perfect" Liquid

Results of elliptic flow measurements can be compared to hydrodynamic models in order to obtain the ratio of shear viscosity to entropy density. The extracted η/S value is very small [27]. Calculations within quantum kinetic theory and within an AdS/CFT framework propose an absolute lower bound of $\eta/S > 1/4\pi$ [28]. The demonstration that the QGP appears to be closer to this limit than any other known liquid led to the claim that the QGP is a nearly "perfect liquid."

2.3 Jets & Jet quenching

While hard-scattered partons can make excellent probes of the QGP, accurately reconstructing the parton energy and direction from the resulting jet fragments is a non-trivial task, particularly in a heavy ion environment. Therefore, high-p_{T} hadrons, which are produced in the fragmentation of high-p_{T} partons, have been used as jet proxies. The modification of "jets" in heavy ion collisions is observed in the suppression of high-p_{T} particles in heavy ion collisions compared to collision systems where no QGP is formed (p+p, d+Au, p+Pb, etc.). The suppression is seen in both inclusive single-particle measurements and in correlation analyses.

2.3.1 R_{AA} and Dihadron correlations

Particle production in heavy ion collisions is compared to elementary collisions in the ratio of the p_{T} spectra in the two systems, known as R_{AA}. The ratio, shown in Eq. 2.3, is scaled by the number of binary collisions (N_{bin}), a geometric factor which

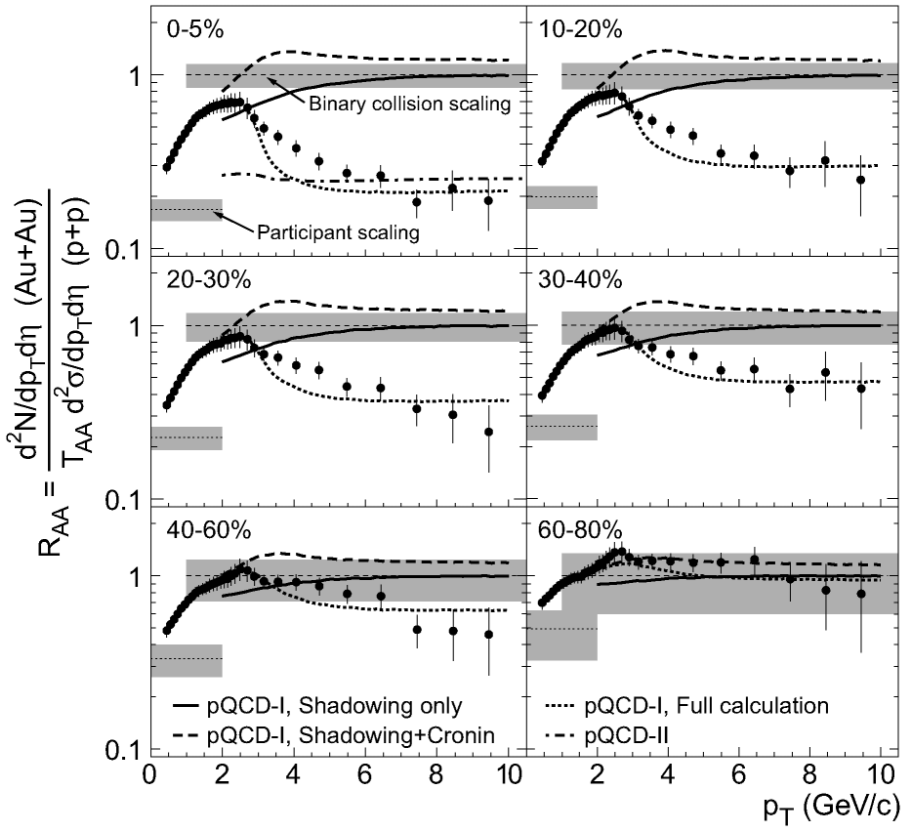

Figure 2.4: R_{AA} measured by STAR for six centrality bins at $\sqrt{s_{NN}} = 200$ GeV. High-p_{T} suppression is observed in central Au+Au collisions, when compared to p+p collisions. [29]

is calculated with a Glauber Monte Carlo model.

$$R_{AA}(p_{\mathrm{T}}) = \frac{\sigma^{pp}_{\mathrm{inel.}}}{\langle N_{\mathrm{bin}} \rangle} \frac{d^2N^{AA}/dp_{\mathrm{T}}d\eta}{d^2\sigma^{pp}/dp_{\mathrm{T}}d\eta} \tag{2.3}$$

If Au+Au collisions behaved as nothing more than a superposition of independent p+p collisions, then R_{AA} would be unity at high p_{T}. (In the soft regime, at low-p_{T}, particle production is expected to scale with a combination of N_{bin} and N_{part}.) It was observed that the number of high-p_{T} particles is suppressed in central Au+Au collisions compared to p+p collisions [29], as shown in Fig. 2.4. Furthermore, when the binary-scaled ratio of the charged hadron spectra in d+Au and p+p was mea-

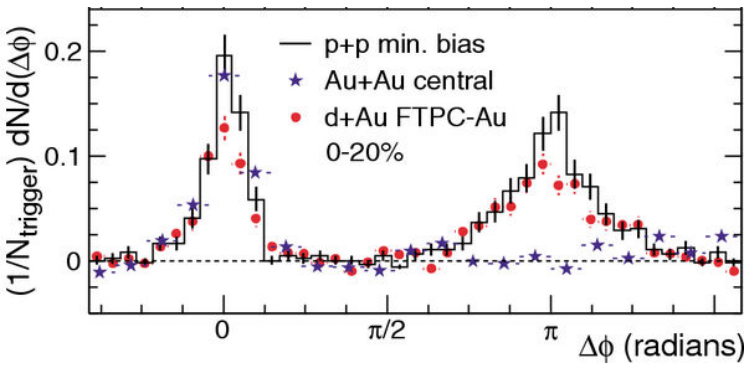

Figure 2.5: Dihadron correlations for $4 < p_{\mathrm{T}}^{\mathrm{trig}} < 6$ GeV/c and $2 < p_{\mathrm{T}}^{\mathrm{assoc}} < p_{\mathrm{T}}^{\mathrm{trig}}$ in Au+Au collisions at $\sqrt{s_{NN}} = 200$ GeV. (In this analysis, $|\eta| < 0.7$.) [30]

sured, no such high-p_{T} suppression was observed [30]. This indicated that high-p_{T} suppression arises from interactions within the hot nuclear matter created in Au+Au collisions.

Analyses of the angular correlations of produced particles are also indicative of jet quenching. In "dihadron" correlation analyses, the distributions of the relative azimuthal angle ($\Delta\phi$) between a "trigger" particle and all "associated" particles in an event are constructed. These correlations can be done differentially with respect to the p_{T}, η, or species of both the trigger particle and the associated particles. In some studies dihadron correlations are investigated in relative pseudorapidity ($\Delta\eta$) as well.

Dihadron correlations of charged hadrons with respect to high-p_{T} trigger particles are used to study jet phenomena. By selecting high-p_{T} hadrons as triggers, the probability is increased that the selected events contain jets, and that the jet is located near $\Delta\phi = 0$. In the $\Delta\phi$ distributions, a peak is observed around $(\Delta\phi, \Delta\eta) = (0, 0)$, which consists of the hadrons associated with the jet containing the trigger hadron. Another peak is typically observed near $\Delta\phi = \pi$ (although extended in $\Delta\eta$), which consists of the hadrons associated with the recoil jet. These jet peaks can be studied with respect to the p_{T} of the constituent hadrons, and lead to insights about

jet structure.

An early result from RHIC was the "disappearance" of the awayside jet [31]. As shown in Fig. 2.5, in a given p_{T} range, the nearside jet peaks are similar in p+p, d+Au, and Au+Au. However, the awayside jet peak, which is similar in p+p and d+Au, is entirely suppressed in central Au+Au collisions in this $p_{\mathrm{T}}^{\mathrm{assoc}}$ range.

2.3.2 Jet reconstruction

While measurements of R_{AA} and dihadron correlations have led to important conclusions about jet energy loss in the QGP, the ability to fully reconstruct jets would allow access to the kinematics of the underlying parton in jet quenching studies. However, finding jets and accurately determining their energy in a heavy ion environment is challenging because the jet signal is embedded within a background of hundreds or thousands of particles from other physical processes in the same heavy-ion event. It is necessary to construct jet algorithms that are well-defined experimentally and theoretically, and develop techniques for handling the large combinatoric background present in heavy ion collisions. Cone-type algorithms have been successfully utilized in elementary collisions, but in heavy ion collisions the sequential recombination algorithms – specifically k_{T} and anti-k_{T} – are preferred.

The sequential recombination algorithms start with a list of "proto-jets," which can be single particles, clusters of energy in a detector, or other objects. The distance between every pair of proto-jets, d_{ij}, and the distance of every proto-jet to the beam, d_{iB}, are defined according to Eq. 2.4:

$$\begin{aligned} d_{ij} &= \min\left(k_{\mathrm{T}i}^{2p}, k_{\mathrm{T}j}^{2p}\right) \frac{((y_i - y_j)^2 + (\phi_i - \phi_j)^2)}{R^2} \\ d_{iB} &= k_{\mathrm{T}i}^{2p} \end{aligned} \tag{2.4}$$

where $k_{\mathrm{T}i}$ is the transverse momentum (equivalent to p_{T}), y_i is the rapidity (in practice the pseudorapidity, η_i, is used), and ϕ_i is the azimuthal angle of any proto-jet i. For any pair, if $d_{ij} < d_{iB}$, then the two proto-jets are merged to form a new proto-jet which is added to the list. If the distance to the beam for proto-jet i is smaller than any d_{ij}, then i is a jet. The procedure continues until all proto-jets have been clustered into jets or no more merging can occur.

When the exponent p is positive, the proto-jets are clustered in order of increasing transverse momentum. When p is negative, the clustering process starts with high-p_{T} proto-jets and works downwards. In particular, $p = 1$ is known as the k_{T} algorithm [32, 33] while $p = -1$ is the anti-k_{T} algorithm [34] (the special case of $p = 0$ is the Cambridge/Aachen algorithm [35, 36]). The characteristic size scale of the jets is set by the resolution parameter R. In particular, anti-k_{T} tends to form jets which are basically circular with radius R.

It is important that jet-finding algorithms have the properties of infrared and collinear safety. Theoretically, infrared safety means that the jet cross-section is insensitive to infrared divergences that appear in higher-order diagrams. Experimentally, an algorithm must be stable if a soft particle ($E_{\mathrm{T}} \to 0$) is added in order to be infrared-safe. Collinear safety requires that the reconstructed jets are stable if one proto-jet is replaced by two proto-jets with lower energy. Anti-k_{T} and k_{T} have been shown to be collinear and infrared safe [34].

In this thesis, jet reconstruction is performed with the anti-k_{T} algorithm utilizing the FastJet software package [37, 38, 39].

Chapter 3

RHIC & STAR

The Relativistic Heavy Ion Collider (RHIC) [40] at Brookhaven National Laboratory on Long Island, New York, is capable of colliding various ion species, from protons to uranium, at energies from $\sqrt{s_{NN}} = 7.7 - 200$ GeV. It can also collide polarized protons (in both longitudinal and transverse polarization states) up to $\sqrt{s_{NN}} = 500$ GeV, and is therefore used to investigate the spin of the proton in addition to the heavy ion program. The Solenoidal Tracker at RHIC (STAR) experiment is one of the large multi-purpose detectors on the RHIC ring that records the results of the collisions.*

3.1 Relativistic Heavy Ion Collider (RHIC)

Ions are accelerated in several stages at the RHIC accelerator complex, shown in Fig. 3.1. The process of accelerating ions to relativistic speeds begins in a Tandem Van de Graaf accelerator, where negatively-charged ($q = -1$) gold ions are extracted from a pulsed sputter ion source and accelerated through a +14MV potential. They

*In Sections 3.1 and 3.2 the RHIC accelerator chain and the STAR detector are described in their 2006/2007 configurations, when the data presented in this thesis were collected. Changes to RHIC and STAR since 2007 are summarized in Section 3.3.

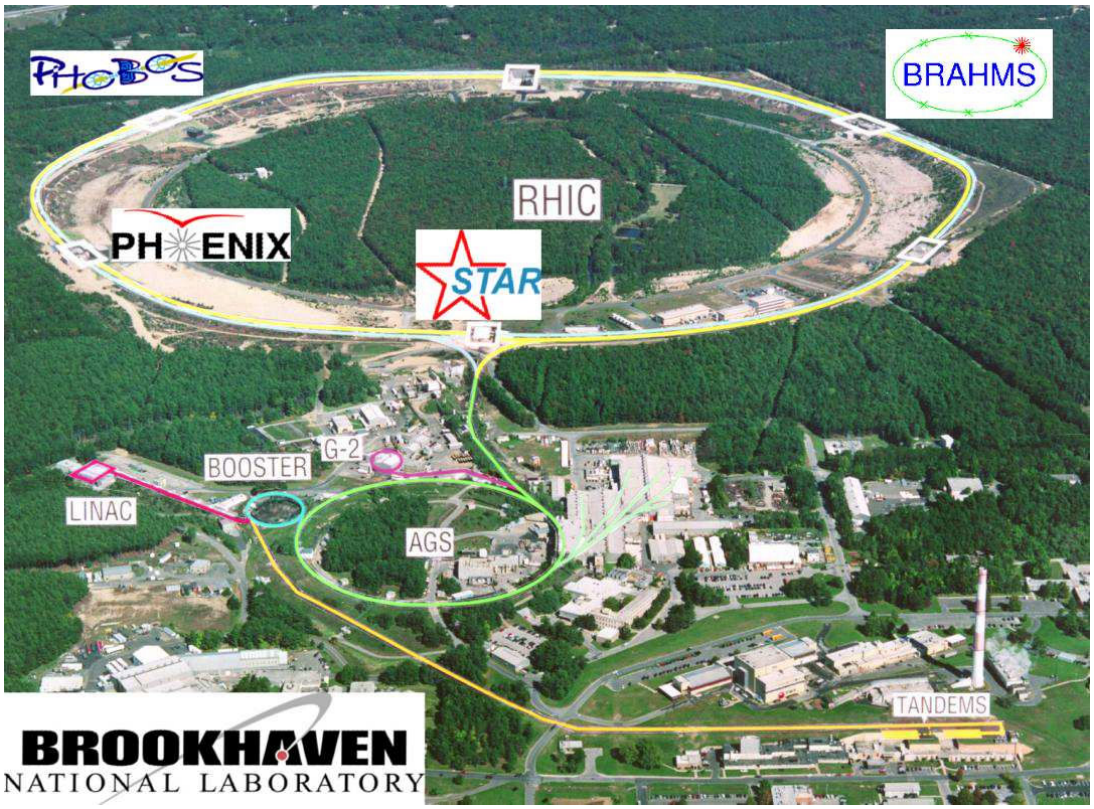

Figure 3.1: The Relativistic Heavy Ion Collider and accelerator chain at Brookhaven National Laboratory (shown in its 2006/2007 configuration).

are then partially stripped of electrons and the positive ions are accelerated back to ground potential. The ions are stripped further, exiting the Tandem with a charge $q = +32$ and kinetic energy of approximately 1 MeV per nucleon, before traveling through a transfer line to the Booster. In the Booster, the ion beam is bunched and accelerated to 95 MeV/nucleon, and stripped of more electrons to achieve a charge state of $q = +77$, before being transferred to the Alternating Gradient Synchrotron (AGS). In the AGS, the beam is debunched, rebunched, and accelerated to 8.86 GeV/nucleon before the ions are stripped of the last two electrons and transferred to the RHIC ring. Once in RHIC, the ions are accelerated from injection energy to top energy (typically 100 GeV/nucleon, but other energies are possible).

When protons are collided at RHIC, they undergo a different acceleration pro-

cess. The protons are first accelerated in a linear accelerator (linac) before being transferred to the Booster, then to the AGS, and finally to RHIC. It is also possible to collide two different ion species at RHIC (such as d+Au or Cu+Au). For this purpose, a second Tandem Van de Graaf accelerator is available, in parallel to the first.

RHIC is a 3.8km (circumference) ring with six interaction points. Originally, four of the interaction regions contained detectors: STAR, PHENIX, PHOBOS, and BRAHMS. The other two house machinery for measuring the polarization of the proton beams, and the RF system. PHOBOS and BRAHMS, the smaller experiments, completed their physics programs after five years and have since been decommissioned. STAR and PHENIX have been operating since 2000.

3.2 Solenoidal Tracker at RHIC (STAR)

The STAR detector [41], shown in Fig. 3.2, was designed with the primary purpose of measuring charged and neutral hadrons, as well as photons and electrons, over a large region in phase space. The principal subsystem in STAR, the Time Projection Chamber (TPC) [42], provides charged particle tracking for a wide range of transverse momentum ($0.15 < p_{\mathrm{T}} < 50$ GeV/c) over full azimuth ($0 < \phi < 2\pi$) and a large spread in pseudorapidity ($|\eta| < 1$). The Barrel Electromagnetic Calorimeter (BEMC) [43] is used for neutral energy detection in the same region, as well as for triggering. The Forward Time Projection Chambers (FTPCs) [44] are capable of detecting charged tracks at forward rapidities ($2.8 < |\eta| < 3.7$), and are used here to determine the event plane. These detector subsystems and others sit within a 0.5 T solenoidal magnet. Finally, the Zero Degree Calorimeters (ZDCs) [45] detect spectator neutrons and are used for triggering; with the addition of Shower Maxi-

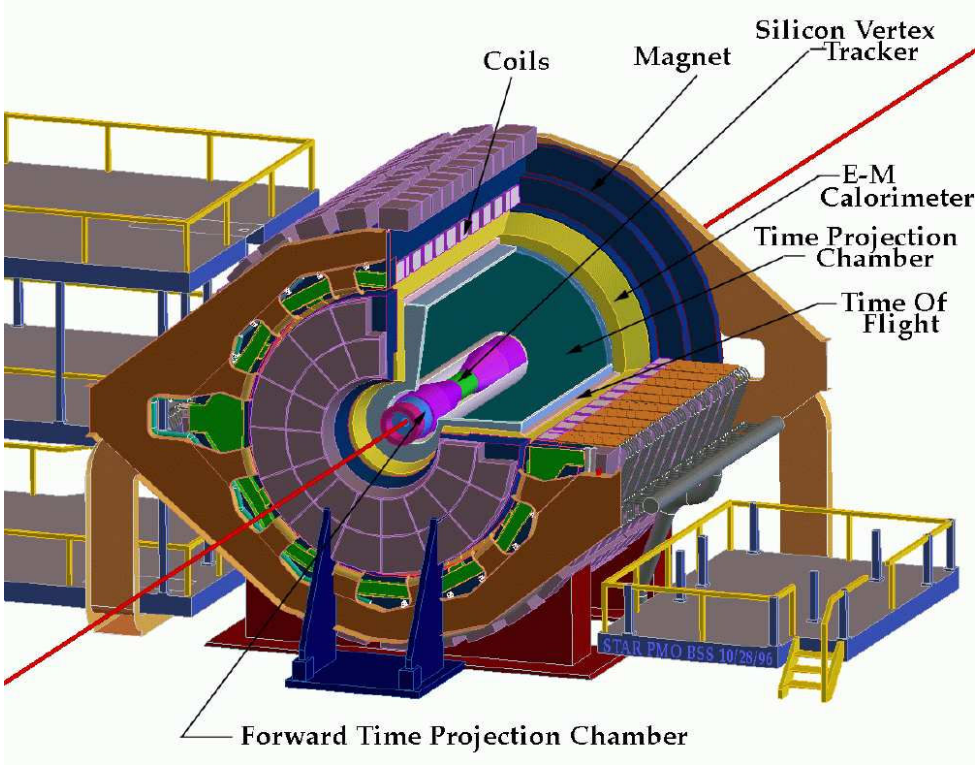

Figure 3.2: The STAR detector. The Time Projection Chamber (TPC), E-M Calorimeter (BEMC), and Forward Time Projection Chambers (FTPCs) are discussed in the text.

mum Detectors (SMDs) [46], which are sensitive to the spatial distribution of the neutrons, the ZDCs can also be used for event plane determination.

3.2.1 Time Projection Chamber (TPC)

At the time it was built, the cylindrical STAR TPC [42, 47] was the largest time projection chamber in the world, with an outer radius of 2 m, inner radius of 0.5 m, and length of 4.2 m. The volume of the TPC is filled with P10 gas (10% methane, 90% argon) in a uniform electric field of $\sim$ 135 V/cm parallel to the beam pipe. The electric field is generated by the Central Membrane, a thin conductive disk perpendicular to the beam pipe at the center of the TPC; the inner and outer field cage cylinders; and the end caps. The Central Membrane is held at 28 kV and the

end caps are at 0 V.

As charged particles traverse the TPC volume they ionize the gas along their path, releasing electrons and positively-charged ions. In the electric field the electrons drift away from the Central Membrane towards the end caps. There the electrons are detected by Multi-Wire Proportional Chambers (MWPCs), which consist of three wire planes: a gating grid, a ground plane, and anode wires. When the gating grid is in a closed configuration, with alternating wires at ± 75 V, neither electrons nor ions can pass through the plane. When the gating grid has all wires at $+110$ V, it is open, and the electrons are accelerated through the high field, producing more electrons in an avalanche. The resulting ions induce a signal on the readout plane, where they trace a two-dimensional projection (in x and y) of the helical track. The z-component of the track is obtained by measuring the drift time of electrons to the endcap and multiplying by the drift velocity (known to be typically ~ 5.45 cm/μs, but calibrated every few hours to account for variations in the atmospheric pressure). Thus the TPC produces a three-dimensional picture of the tracks produced in a collision.

Charged particle trajectories bend within the magnetic field, allowing for the particle's momentum to be determined from the curvature of the track. Therefore, from the spatial information read out in the TPC, the following properties of a charged particle can be determined (assuming a charge of ± 1): momentum (p and its components p_x, p_y, p_z), azimuthal angle (ϕ), polar angle (θ), pseudorapidity (η), and the sign of the charge. Furthermore, the amount of ionization energy released along the track (dE/dx) can be measured, and this information combined with the momentum can be used for particle identification. In the momentum range where this method of particle identification is accurate ($p \lesssim 1$ GeV/c), the species, mass, and rapidity (y), of charged particles can also be determined.

3.2.2 Barrel Electromagnetic Calorimeter (BEMC)

The BEMC [43] is a lead-scintillator sampling calorimeter which has full 2π azimuthal coverage in the region $|\eta| < 1$. Located just outside the TPC, it fulfills three main purposes in STAR: to detect neutral particles (principally π^0 and γ), to discriminate between electrons and hadrons, and as a fast trigger detector to select events with high-p_{T} processes.

The BEMC is divided into 120 modules that cover 6° in ϕ and 1.0 unit in η, each consisting of 40 towers. Towers in the BEMC have an angular size of $\Delta\phi \times \Delta\eta = 0.05 \times 0.05$ and are projective back to the center of the interaction region. Each tower contains a stack of 21 scintillation layers alternating with 20 layers of lead. When electrons, photons, or hadrons pass through the stack they produce electromagnetic showers. In the dense Pb layers, high-energy electrons produce photons via bremsstrahlung and photons undergo pair production to produce electrons, thus a single high-energy electron or photon initiates a cascade of lower-energy electrons and photons that traverses the tower. In the scintillation layers the shower energy is converted to a light signal, which is transfered to photomultiplier tubes (PMTs) outside of the STAR magnet that digitize the signal. Therefore it is possible to study the longitudinal evolution of the shower.

Each BEMC tower consists of three parts: the tower structure itself (BTOW), the preshower detector (BPRS), and the shower maximum detector (BSMD). The BPRS (which is comprised of the first two scintillator layers) and BSMD (located between the fifth Pb layer and sixth scintillator layer) are used to fulfill one of the main purposes of the BEMC, which is improved electron/hadron discrimination. In order to measure the neutral energy component (γ, π^0, η, etc.) of heavy ion collision events, which is another of the main purposes of the BEMC, only the BTOW is used.

Any energy deposited in the BEMC towers that cannot be correlated with a charged track in the TPC is taken to be neutral energy. In this thesis, the neutral energy in the BEMC is not reconstructed back to the particle level; instead, neutral towers are utilized as input constituents to the jet-finding algorithms.

The BEMC is a fast detector (unlike the TPC) and can therefore be used to make trigger decisions, i.e. to decide which events should be recorded. In particular, the BEMC can trigger on events in which a large amount of energy is localized in a small region of $\eta - \phi$ space, which would indicate that the event contains a rare high-p_{T} jet. For example, the high tower (HT) trigger fires when the energy deposition in a single BEMC tower surpasses a set transverse energy threshold, while the jet patch (JP) trigger fires when the energy in a cluster of towers is above a given threshold.

3.2.3 Forward Detectors

Forward Time Projection Chamber (FTPC)

The FTPCs [44] are used to reconstruct charged tracks at forward rapidities. They operate under similar principles as the larger, mid-rapidity TPC described in Section 3.2.1, with a few key differences. Principally, the electric field in the FTPCs is radial, and therefore the electrons drift radially outwards towards curved read-out MWPCs that wrap around the cylindrical detectors. The gas used is also different from that of the TPC: a mixture of 50% Ar and 50% CO_2.

The FTPCs are 120 cm long and have a diameter of 75 cm, and fit inside the TPC; the sensitive volume is 93.7 cm long with an outer radius of 30.05 cm and an inner radius of 7.73 cm. They are located along the beam pipe at $162.75 < |z| < 256.75$, meaning that they have a maximum possible coverage of $2.5 < |\eta| < 4.0$ ($2.1^\circ < \theta < 9.4^\circ$). As will be discussed in Section 5.3.2, in the data analysis a stricter cut is

placed on η in order to ensure track quality and more uniform coverage in ϕ.

Zero-Degree Calorimeter - Shower Maximum Detector (ZDC-SMD)

The STAR ZDCs [45] are calorimeters that predominantly detect spectator neutrons and are located 18 m down the beamline on either side of the interaction point. Each ZDC consists of three modules; each module is a planar tungsten-plastic hadronic calorimeter that is pitched at a 45° angle with respect to the beam. They serve as a minimum bias trigger, and, since each interaction point at RHIC has an identical set of ZDCs, they allow for event rate normalization amongst the experiments.

The ZDCs are located beyond the bending magnets that direct charged particles into the blue and yellow beams. Neutral particles emitted with an angle less than 4 milliradians from the beamline ($|\eta| > 6.2$) continue along straight trajectories and impinge upon the ZDCs. The ZDCs can be utilized as trigger detectors because neutrons that evaporate off the nuclear remnants are expected to only diverge from the beam by less than 2 mr. Therefore the detection of at least one neutron in the ZDCs is evidence that a collision has occurred.

In 2004, shower maximum detectors were inserted between the first and second module in each ZDC (to form the full ZDC-SMD detectors) [46]. Each SMD consists of two planes of scintillator strips: one plane of 21 strips aligned vertically and the other of 32 horizontal strips. These strips have a triangular cross-section and are optically isolated from each other. Three adjacent vertical strips comprise one vertical slat, and a horizontal slat consists of four horizontal strips. The signals from the strips in a single slat are combined and read out by one channel in a 16-channel PMT. The energy deposition in each of the 7 vertical and 8 horizontal slats provides information about the spatial distribution of the spectator neutrons, not just the total energy, and can be used to reconstruct the event plane at far forward rapidities

(see Section 5.3.3).

3.3 Upgrades after 2007

The accelerator and experiments at RHIC are continually being upgraded in order to advance their physics programs.

The replacement of the sputter ion source and Tandems by the Electron Beam Ion Source (EBIS) [48] makes it possible to accelerate a wide range of ions from helium to uranium for injection into RHIC. In 2012, for the first time, U+U collisions were recorded. Uranium nuclei are significantly non-spherical (prolate), compared to gold nuclei which are only slightly oblate, meaning that more interesting collision geometries can be accessed in the U+U system. For example, "body-body" collisions are central (small impact parameter) but are highly anisotropic, providing a vital test of the possible local parity violation signatures observed in Au+Au collisions [49].

Additionally, the flexibility of RHIC has been exploited to search for the phase transition and possible critical point of the QCD phase diagram. In 2010 and 2011, a Beam Energy Scan (BES) [50] was conducted, during which Au+Au collisions were recorded at $\sqrt{s_{\mathrm{NN}}}$ = 62.4, 39, 27, 19.6, 11.5, and 7.7 GeV. Each of these energies probes a different (μ_B, T) region in the QCD phase diagram. Signatures of QGP creation, such as v_2 scaling [51, 52] and high-p_{T} suppression, have been measured at each energy to look for the phase transition, but the results remain inconclusive and further theoretical and experimental work is required in this area.

Additional detector subsystems have extended the capabilities of STAR since 2007. In 2009 and 2010, a Time-Of-Flight (TOF) detector was installed, making it possible to perform particle identification up to $p_{\mathrm{T}} \sim 3$ GeV/c (recall that PID with dE/dx in the TPC is only possible up to $p_{\mathrm{T}} \sim 1$ GeV/c). Other detector

upgrades are underway for increasing STAR's ability to do heavy flavor physics. The Muon Telescope Detector (MTD) will be used to measure J/ψ and Υ decays in the muon channel. The Heavy Flavor Tracker (HFT) will extend tracking to small radii, making it possible to do direct topological reconstruction of open charm decays as well as reduce backgrounds in order to identify short-lived vector mesons (ω and ϕ).

The longer-term future plan for RHIC may involve installing an electron ring, converting RHIC into an electron-ion collider (EIC). To take advantage of electron-ion collisions and perform EIC physics, STAR is also planning for significant detector upgrades in the forward direction.

Chapter 4

Jet-hadron Correlations

Jet quenching has been observed and investigated in dihadron correlation analyses [30, 31], which typically use a high-p_{T} hadron as a proxy for the axis of a jet. Due to recent advances in jet-finding algorithms and techniques, it is now possible to utilize reconstructed jets as triggers in correlation analyses. Compared to high-p_{T} hadrons, using reconstructed jets allows for a more precise determination of the original parton four-momentum, and also extends the kinematic reach of correlation studies. In jet-hadron correlations, the trigger population is dominated by jets that originate from higher-p_{T} partons than those accessible in dihadron correlations.

In the jet-hadron analysis, correlations of charged hadrons with respect to the axis of a reconstructed jet are investigated. The correlations are compared in Au+Au and p+p collisions to look for evidence of medium-induced jet quenching. The observed differences between Au+Au and p+p are quantified via the Gaussian yields and widths of the jet peaks, I_{AA}, D_{AA}, and ΣD_{AA}, which are defined in Section 4.1. The two main sources of systematic uncertainties are the shape of the combinatoric background (discussed in Section 4.6) and the trigger jet energy scale (Section 4.4). The results of the jet-hadron correlation analyses are shown in Section 4.8 and

compared to theoretical calculations in Section 4.9.

4.1 Observables

The comparison between jets in Au+Au and p+p is quantified with five measures: the Gaussian yields (Y) and widths (σ) of the associated hadron peaks about the jet axis, $I_{AA}(p_{\mathrm{T}}^{\mathrm{assoc}})$, $D_{AA}(p_{\mathrm{T}}^{\mathrm{assoc}})$, and ΣD_{AA}, defined in Eqs. (4.1)–(4.3),

$$I_{AA}(p_{\mathrm{T}}^{\mathrm{assoc}}) \equiv \frac{Y_{Au+Au}(p_{\mathrm{T}}^{\mathrm{assoc}})}{Y_{p+p}(p_{\mathrm{T}}^{\mathrm{assoc}})} \tag{4.1}$$

$$D_{AA}(p_{\mathrm{T}}^{\mathrm{assoc}}) \equiv Y_{Au+Au}(p_{\mathrm{T}}^{\mathrm{assoc}}) \cdot \langle p_{\mathrm{T}}^{\mathrm{assoc}} \rangle_{Au+Au} - Y_{p+p}(p_{\mathrm{T}}^{\mathrm{assoc}}) \cdot \langle p_{\mathrm{T}}^{\mathrm{assoc}} \rangle_{p+p} \tag{4.2}$$

$$\Sigma D_{AA} \equiv \sum_{p_{\mathrm{T}}^{\mathrm{assoc}}\ \mathrm{bins}} D_{AA}(p_{\mathrm{T}}^{\mathrm{assoc}}) \tag{4.3}$$

where $\langle p_{\mathrm{T}}^{\mathrm{assoc}} \rangle$ is the mean $p_{\mathrm{T}}^{\mathrm{assoc}}$ in a given $p_{\mathrm{T}}^{\mathrm{assoc}}$ bin. I_{AA}, the ratio of the associated yields, folds in the shapes of the associated particle spectra in Au+Au and p+p, while D_{AA} measures the energy difference between Au+Au and p+p. If jets in Au+Au fragment like in p+p, then $I_{AA} = 1$ and $D_{AA} = 0$ for all $p_{\mathrm{T}}^{\mathrm{assoc}}$. Deviations from these values are indicative of jet modification. Even if $D_{AA}(p_{\mathrm{T}}^{\mathrm{assoc}}) \neq 0$, it is possible for $\Sigma D_{AA} = 0$, indicating that the overall energy is balanced between high-$p_{\mathrm{T}}^{\mathrm{assoc}}$ and low-$p_{\mathrm{T}}^{\mathrm{assoc}}$ fragments.

Each quantity can be evaluated on the nearside (NS, around the trigger jet axis) and awayside (AS, 180° away from the trigger jet). The Gaussian yields of the jet peaks, Y, are integrated over a given bin in the transverse momentum of the associated hadrons ($p_{\mathrm{T}}^{\mathrm{assoc}}$), and the reconstructed jet p_{T} ($p_{\mathrm{T}}^{\mathrm{jet,rec}}$), as well as over the $\Delta\eta$ acceptance.

4.2 Data Sets, Event Selection, & Track Selection

The data analyzed here were collected in Au+Au and p+p collisions at $\sqrt{s_{NN}}$ = 200 GeV in 2007 and 2006, respectively. This analysis utilizes charged tracks that are reconstructed in the TPC and the transverse energy (E_{T}) of neutral hadrons, which is measured in the BEMC. Energy deposited by charged hadrons in the BEMC is accounted for by a 100% hadronic correction, in which the transverse momentum of any charged track pointing towards a tower is subtracted from the transverse energy of that tower (if this subtraction would cause the tower energy to be negative, the tower energy is set to zero).

The events analyzed in both Au+Au and p+p were selected by an online high tower (HT) trigger, which requires that a certain amount of transverse energy be deposited in at least one tower in the BEMC. This trigger makes it possible to collect a large sample of the rare events that contain a high-p_{T} particle, and are therefore more likely to contain jets. For example, in the 2007 Au+Au run, the integrated sampled luminosity for the HT trigger was 600 μb^{-1}, which corresponds to 3.4 million events. The integrated sampled luminosity for the minimum bias trigger (mb-zdc, described below) was only 0.11 μb^{-1}, meaning that without the HT trigger it would have been necessary to run for 5,500 times as long to collect a comparable jet sample [53]. In p+p the HT threshold was $E_{\mathrm{T}}^{\mathrm{HT}} > 5.4$ GeV [54] while in Au+Au the threshold was $E_{\mathrm{T}}^{\mathrm{HT}} > 5.5$ GeV [53]. Since the HT thresholds were slightly different in Au+Au and p+p, and to avoid the non-linear trigger turn-on behavior, the threshold was increased to $E_{\mathrm{T}}^{\mathrm{HT}} > 6$ GeV and reapplied offline, after the hadronic correction.

Events selected by a minimum bias (MB) trigger are also utilized in parts of this analysis. The MB trigger only requires coincident energy deposition in the ZDCs,

and therefore selects a population of events that is a representative sample of all heavy ion collisions.

In Au+Au only the 20% most central events are analyzed, where event centrality is determined by the uncorrected charged particle multiplicity in the TPC within pseudorapidity $|\eta| < 0.5$. Events are required to have a primary vertex position along the beam axis (v_z) within 25 cm of the center of the TPC. Tracks are required to have $p_{\mathrm{T}} > 0.2$ GeV/c, at least 20 points measured in the TPC (out of a maximum of 45), a 3D distance of closest approach to the collision vertex of less than 1 cm, and $|\eta| < 1$. Events containing tracks with $p_{\mathrm{T}} > 30$ GeV/c are not considered because of poor momentum resolution.

4.3 The Trigger Jet

Jets are reconstructed with the anti-k_{T} algorithm in FastJet with a resolution parameter $R = 0.4$ (see Section 2.3.2). Only charged tracks in the TPC with $p_{\mathrm{T}}^{\mathrm{track}} > 2$ GeV/c and neutral towers in the BEMC with $E_{\mathrm{T}}^{\mathrm{tower}} > 2$ GeV are used in the jet reconstruction procedure. The axes of the reconstructed trigger jets are required to fall within $|\eta_{\mathrm{jet}}| < 1 - R$ so that the (nominal) jet cone is contained fully within the TPC. The trigger jet is the highest-p_{T} jet that contains (i.e. has as one of its constituents) a BEMC tower that fired the HT trigger (with $E_{\mathrm{T}}^{\mathrm{HT}} > 6$ GeV).

The combination of the $p_{\mathrm{T}}^{\mathrm{track,tower}}$ cut and the HT trigger requirement biases the jet sample towards unmodified jets in Au+Au [55], which makes comparisons to p+p jets more straightforward. This similarity between Au+Au and p+p HT jets is evidenced by the shapes of the jet spectra (see Fig. 4.4) and by the shapes and magnitudes of the nearside associated hadron correlations (see Fig. 4.10). The bias towards unmodified jets means that the trigger jets are more likely to be emitted

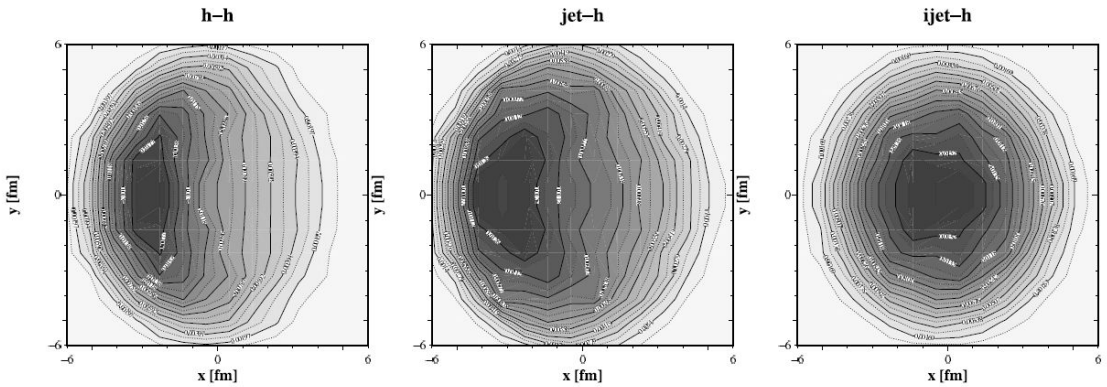

Figure 4.1: The distribution of hard-scattering vertices is shown for three types of trigger objects: (left) a single hadron, (center) a jet reconstructed with the jet definition used in the jet-hadron analysis, and (right) an "ideal" jet. All the trigger objects are traveling in the $-x$ direction and have $12 < p_{\mathrm{T}} < 15$ GeV/c. The distribution is modeled within the YaJEM-DE MC model of medium-induced parton energy loss, for 10% central Au+Au collisions at $\sqrt{s_{NN}} = 200$ GeV [60].

near the surface of the medium [56, 57, 58], increasing the probability that the recoil parton will travel a significant distance through the QGP [59], and therefore enhancing awayside partonic energy loss effects. Figure 4.1 shows the spatial distributions of production vertices for jets reconstructed under different definitions, as calculated within a specific Monte Carlo implementation of medium-induced shower modification [60]. The results of the model indicate that the vertices of jets reconstructed with the definition here ($p_{\mathrm{T}}^{\mathrm{track,tower}} > 2$ GeV/c, $E_{\mathrm{T}}^{\mathrm{HT}} > 6$ GeV) are more concentrated towards the surface of the medium, compared to "ideal" jets (no $p_{\mathrm{T}}^{\mathrm{track,tower}}$ or $E_{\mathrm{T}}^{\mathrm{HT}}$ requirements), which have a distribution of production vertices corresponding to the matter distribution in heavy ion collisions. Of course, it is not possible to claim that Au+Au HT trigger jets are entirely unmodified (or entirely surface-biased), and therefore conservative uncertainties are assigned to cover any medium-induced modification of the trigger jet.

The $p_{\mathrm{T}}^{\mathrm{track,tower}} > 2$ GeV/c cut also greatly reduces the background energy that is clustered into the jet cone and therefore eliminates the need for an average back-

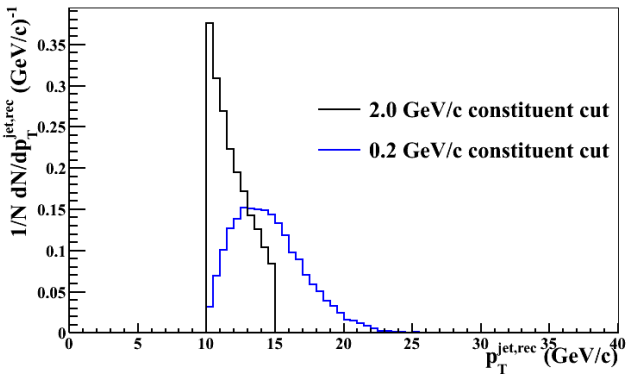

Figure 4.2: The effect of the 2 GeV/c constituent cut on the jet energy scale can be illustrated by reconstructing p+p HT jets with both a high (2 GeV/c) and a low (0.2 GeV/c) constituent p_{T} cut. For jets reconstructed with $10 < p_{\mathrm{T}}^{\mathrm{jet,2\ GeV/}c} < 15$ GeV/c (black), the corresponding distribution of $p_{\mathrm{T}}^{\mathrm{jet,0.2\ GeV/}c}$ is shown (blue).

ground energy (ρA) subtraction [61], which is typically necessary in full-jet reconstruction analyses. Fluctuations in the background energy are also suppressed, and can be accounted for by a bin-by-bin unfolding procedure described below. However, it is important to note that since the reconstructed jet p_{T} (denoted by $p_{\mathrm{T}}^{\mathrm{jet,rec}}$) is calculated only from constituents with $p_{\mathrm{T}}^{\mathrm{track,tower}} > 2$ GeV/c, and therefore it does not directly correspond to the parton energy. Figure 4.2 shows the effect of the $p_{\mathrm{T}}^{\mathrm{track,tower}} > 2$ GeV/c cut on the reconstructed jet energies for p+p HT jets.

4.3.1 Matching Jet Energies in Au+Au and *p*+*p*

In order to make quantitative comparisons between jets in Au+Au and p+p it is necessary to match jets with the same parent parton energy in the two systems. Instead of correcting the reconstructed jet energy back to the energy of the parent parton, in this analysis the distributions of p+p and Au+Au detector-level jet energies are selected such that the corresponding parton energy distributions match, i.e. the Au+Au jet population is matched to equivalent p+p jets. This is accomplished through a bin-by-bin unfolding procedure, where the correspondence between Au+Au and p+p jet energies is determined by embedding.

Since Au+Au HT trigger jets seem to be mostly unmodified by the medium, a Au+Au HT event can be described well by a p+p HT jet event on top of a Au+Au

MB background. The effects of the heavy ion combinatoric background on the trigger jet energy scale can be assessed by comparing the reconstructed jet energies before and after embedding a p+p jet in a Au+Au background. Figure 4.3a shows the correspondence between the reconstructed jet energy of a p+p HT jet before (p_{T}^{p+p}) and after ($p_{\mathrm{T}}^{p+p,\mathrm{emb}}$) the p+p HT event is embedded in a Au+Au MB background. The shift in the jet energy due to background fluctuations, $\delta p_{\mathrm{T}} = p_{\mathrm{T}}^{p+p,\mathrm{emb}} - p_{\mathrm{T}}^{p+p}$, is shown in Fig. 4.3b: most jets have $\delta p_{\mathrm{T}} = 0$; a significant fraction of jets have one background particle clustered into the jet cone so $\delta p_{\mathrm{T}} \simeq 2$ GeV/c; a small fraction have two background particles in the jet cone so $\delta p_{\mathrm{T}} \simeq 4$ GeV/c; smaller fractions have $\delta p_{\mathrm{T}} \simeq 6$ GeV/c and 8 GeV/c; a few jets have $\delta p_{\mathrm{T}} < 0$, since a lower tracking efficiency in Au+Au than in p+p leads to some tracks being lost. The embedding procedure is performed as a function of multiplicity, and then weighted to match the multiplicity distribution in 0-20% central Au+Au HT events. The results are also calculated as a function of the relative angle to the event plane of the underlying Au+Au MB event, and then weighted to simulate a non-zero jet v_2.

If HT trigger jets in Au+Au are unmodified, and therefore perfectly p+p-like, then this procedure produces the correspondence between the reconstructed energy of a Au+Au HT trigger jet and the reconstructed energy of the equivalent p+p jet. From the correspondence between p_{T}^{p+p} and $p_{\mathrm{T}}^{p+p,\mathrm{emb}}$, for a given range in p_{T}^{p+p} the distribution of $p_{\mathrm{T}}^{p+p,\mathrm{emb}} \simeq p_{\mathrm{T}}^{Au+Au}$ distribution can be obtained. As an example, Fig. 4.3c shows the distribution of embedded p+p jet energies corresponding to p+p jets with $10 < p_{\mathrm{T}}^{p+p} < 15$ GeV/c. In order to compare Au+Au jets to equivalent p+p jets in this analysis, the Au+Au signal is weighted to match this distribution of $p_{\mathrm{T}}^{p+p,\mathrm{emb}}$.

The shapes of the jet p_{T} spectra for p+p HT jets, embedded p+p HT jets, and Au+Au HT jets are compared in Fig. 4.4(a). Since the $(1/N)dN/dp_{\mathrm{T}}^{p+p,\mathrm{emb}}$ distribu-

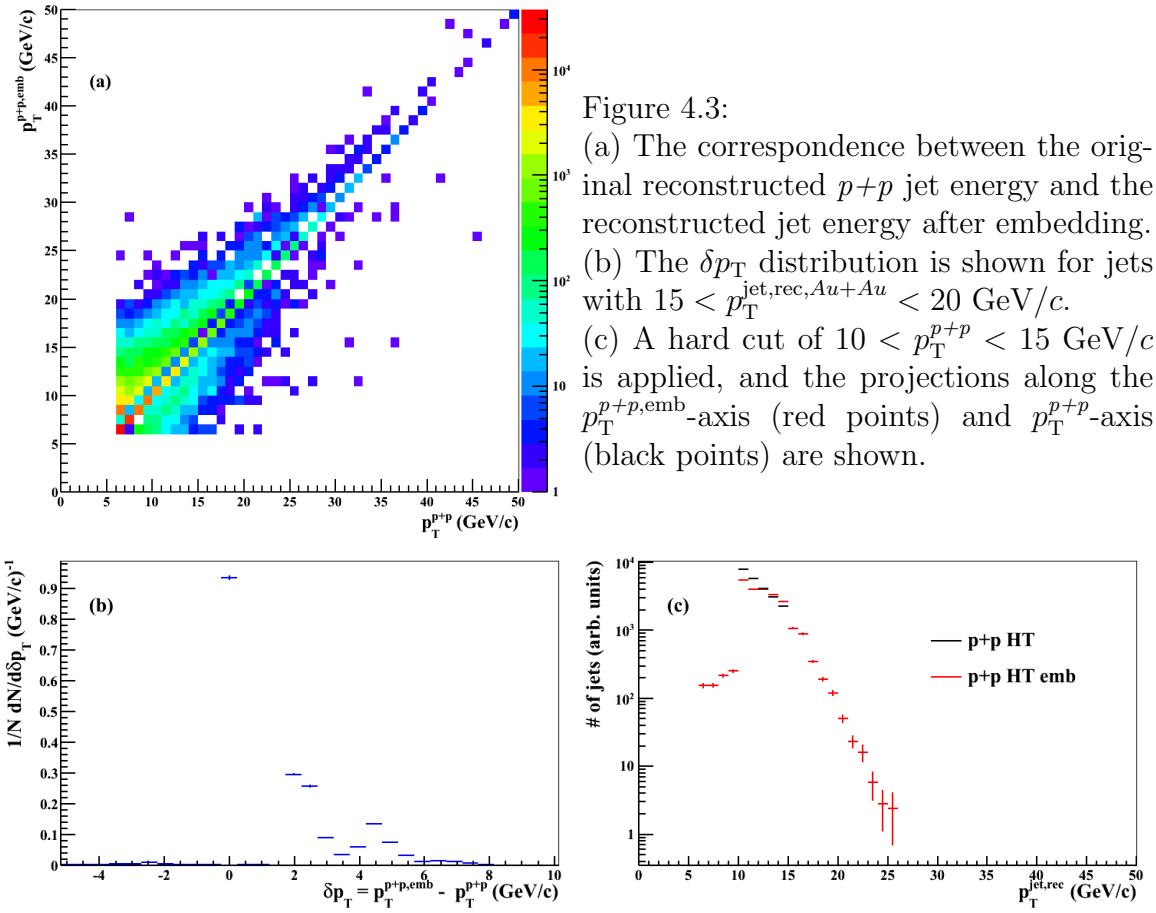

Figure 4.3:
(a) The correspondence between the original reconstructed p+p jet energy and the reconstructed jet energy after embedding. (b) The δp_{T} distribution is shown for jets with $15 < p_{\mathrm{T}}^{\mathrm{jet,rec},Au+Au} < 20$ GeV/c. (c) A hard cut of $10 < p_{\mathrm{T}}^{p+p} < 15$ GeV/c is applied, and the projections along the $p_{\mathrm{T}}^{p+p,\mathrm{emb}}$-axis (red points) and p_{T}^{p+p}-axis (black points) are shown.

tion is much closer to the $(1/N)dN/dp_{\mathrm{T}}^{Au+Au}$ distribution than the $(1/N)dN/dp_{\mathrm{T}}^{p+p}$ distribution, it can be concluded that the embedding procedure largely accounts for the difference between the shapes of the $(1/N)dN/dp_{\mathrm{T}}^{p+p}$ and $(1/N)dN/dp_{\mathrm{T}}^{Au+Au}$ spectra, and that the assumption of Au+Au HT jets being similar to p+p HT jets embedded in a Au+Au background is valid. The ratios of the spectra are shown in Fig. 4.4(b), where it can be seen that particularly at low p_{T}, the ratio of the p_{T}^{Au+Au} spectrum to the $p_{\mathrm{T}}^{p+p,\mathrm{emb}}$ spectrum is restored to unity after embedding.

While the shapes of the spectra shown in Fig. 4.4 are similar, they are not equivalent. This could be indicative of medium-induced trigger jet modification, but much more work on understanding the trigger jet energy scale is necessary before such a statement could be made (or refuted) conclusively. In this analysis the near-

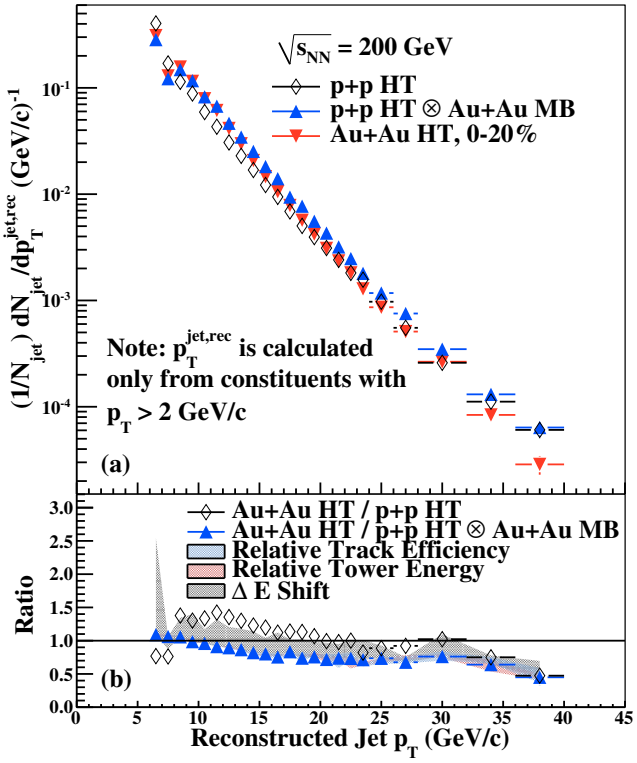

Figure 4.4:
(a) Detector-level $p_{\mathrm{T}}^{\mathrm{jet,rec}}$ spectra of HT trigger jets in p+p and Au+Au, and of p+p HT trigger jets embedded in Au+Au MB events.
(b) Ratio of $(1/N)dN/dp_{\mathrm{T}}^{Au+Au}$ to $(1/N)dN/dp_{\mathrm{T}}^{p+p,\mathrm{emb}}$ with uncertainties due to the relative tracking efficiency, relative tower energy, and ΔE shift. The ratio of $(1/N)dN/dp_{\mathrm{T}}^{Au+Au}$ to $(1/N)dN/dp_{\mathrm{T}}^{p+p}$ is also shown.

side/trigger jet is only used to define systematic uncertainties, while the effects of jet-medium interactions are investigated on the awayside. The possibility of additional discrepancies between the reconstructed jet energies in Au+Au and p+p, due to physics or other measurement effects, is included within systematic uncertainties.

4.4 Jet Energy Scale Uncertainties

The uncertainties on the trigger jet energy scale are assessed under two extreme and opposite assumptions.

1. *HT trigger jets in Au+Au are unmodified compared to HT trigger jets in* p+p. In this scenario, the shape of the jet spectrum in Au+Au should match the shape of the jet spectrum of p+p jets embedded in a heavy ion background. As shown in Fig. 4.4, the shapes of the spectra do not match even after detector effects are accounted for. A shift of $\Delta E = +1$ GeV/c in the p+p trigger jet

energy encompasses the difference in the shapes, as demonstrated by the ΔE systematic uncertainty band in Fig. 4.4(b) which encompasses unity for most values of $p_{\mathrm{T}}^{\mathrm{jet,rec}}$.

As an explicit example, the ΔE shift is applied in the $10 < p_{\mathrm{T}}^{\mathrm{jet,rec}} < 15$ GeV/c bin by determining the Au+Au jet energy distribution (the $p_{\mathrm{T}}^{p+p,\mathrm{emb}}$ points in Fig. 4.3) for the range $11 < p_{\mathrm{T}}^{\mathrm{jet,rec},p+p} < 16$ GeV/c, and recalculating the correlation functions for that distribution of $p_{\mathrm{T}}^{\mathrm{jet},Au+Au}$.

2. *HT trigger jets in Au+Au are maximally modified compared to HT trigger jets in* p+p. In this case, jets originating with similar parton energies would not have equivalent reconstructed jet energies, because $p_{\mathrm{T}}^{\mathrm{jet}}$ is calculated only from fragments with $p_{\mathrm{T}} > 2$ GeV/c. However, if all the missing fragments at high-p_{T} reappear as low-p_{T} particles, then the energy of the jets in Au+Au and p+p should balance exactly (in other words, $\Sigma D_{AA} = 0$ on the nearside) when the parton energies are matched correctly. Therefore another systematic uncertainty is defined by the shift in the p+p trigger jet energy necessary to force NS ΣD_{AA} to zero, under the assumption that the background is flat (as explained in Section 4.6).

   The $p_{\mathrm{T}}^{\mathrm{jet},p+p}$ range is shifted downwards in steps of 1 GeV/c until the NS ΣD_{AA} (when calculated under the assumption that $v_2^{\mathrm{assoc}} v_2^{\mathrm{jet}} = v_3^{\mathrm{assoc}} v_3^{\mathrm{jet}} = 0$) falls below zero. Table 4.1 shows the magnitudes of NS ΣD_{AA} before and after the shifts, as well as the necessary shift to the jet energy.

   Two observations should be noted from Table 4.1. First, in the lowest jet p_{T} range, shifts of -3 GeV/c or more start interfering with the HT threshold of 6 GeV and producing strange behaviors in the jet energy distributions. This is why the ΣD_{AA} does not quite get below zero. Second, in the middle jet p_{T}

$p_{\mathrm{T}}^{\mathrm{jet,rec}}$ (GeV/c)	NS ΣD_{AA} (GeV/c) before shift	Shift (GeV/c)	NS ΣD_{AA} (GeV/c) after shift
$10-15$	2.8	-2	0.5
$15-20$	4.0	-5	-0.7
$20-40$	2.8	-4	-0.1

Table 4.1: The jet energy shifts required to force ΣD_{AA} below zero are shown for three ranges in jet p_{T}. The values of the NS ΣD_{AA} (under the assumption that $v_2^{\mathrm{assoc}} v_2^{\mathrm{jet}} = v_3^{\mathrm{assoc}} v_3^{\mathrm{jet}} = 0$) are shown before and after the shifts.

bin, fitting issues in the lowest $p_{\mathrm{T}}^{\mathrm{assoc}}$ bin cause the NS ΣD_{AA} to be abnormally large (this is also apparent in Fig. 4.10). Hence the shift to restore ΣD_{AA} to zero is also large, and is probably an overestimate.

4.5 Correlation Functions

Once a HT trigger jet has been found in an event, the associated hadron correlation functions are constructed with respect to the angle of the jet axis. The jet-hadron correlation functions are distributions of $\Delta\phi = \phi_{\mathrm{assoc}} - \phi_{\mathrm{jet}}$, where ϕ_{jet} denotes the azimuthal angle of the axis of the reconstructed trigger jet and the associated particles are all charged hadrons in the event. The $\Delta\phi$ correlations are analyzed in bins in the reconstructed transverse momentum of the trigger jet ($p_{\mathrm{T}}^{\mathrm{jet,rec}}$) and in the transverse momentum of the associated hadrons ($p_{\mathrm{T}}^{\mathrm{assoc}}$).

4.5.1 Acceptance & Efficiency Corrections

It is necessary to correct the $\Delta\phi$ distributions for the TPC acceptance and efficiency. The probability of accurately reconstructing a charged track in the TPC depends on ϕ, η, and p_{T}, and is accounted for by single- and two-particle efficiency corrections. The single particle tracking efficiency is an absolute correction, which adjusts the particle yields as a function of η and p_{T}, while the pair efficiency is a relative

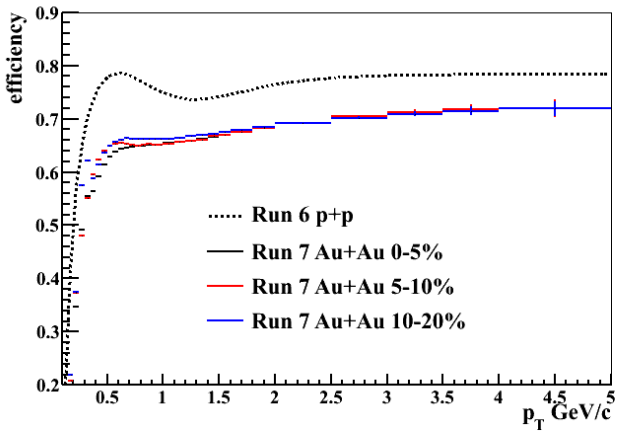

Figure 4.5: The single particle tracking efficiencies in p+p (black dotted line) and Au+Au (black, red, and blue points for the 0-5%, 5-10%, and 10-20% centrality bins, respectively) are shown as a function of p_{T}. Details of the efficiency determination can be found in Appendix A.

correction, adjusting the shapes of the $\Delta\phi$ distributions.

The methods for determining the single particle tracking efficiency in both p+p and Au+Au environments are discussed in Appendix A, and the efficiencies in p+p and Au+Au are shown as a function of p_{T} in Fig. 4.5. When the $\Delta\phi$ histograms are created, each track is weighted by the inverse of the single particle tracking efficiency.

The pair efficiency correction accounts for the ϕ-dependence of the detector inefficiencies, and also depends on the track p_{T}. This correction is done by "event mixing:" a $\Delta\phi|_{\mathrm{mix}} = \phi_{\mathrm{assoc}}^{\mathrm{event2}} - \phi_{\mathrm{jet}}^{\mathrm{event1}}$ histogram is created in which the trigger jet is from one event and the associated particles are from another event. Since the trigger and associates are from different events and therefore uncorrelated, any structure to the $\Delta\phi|_{\mathrm{mix}}$ correlations is due to detector effects instead of physics. In this analysis, each trigger jet in Au+Au is mixed with the charged tracks from 50 other 0-20% central Au+Au HT events, and each trigger jet in p+p is mixed with 50 other p+p HT events. The mixing is not done in v_z bins or fine centrality bins because of limited statistics. The mixed event distributions are normalized so that the highest bin is at unity. In each $p_{\mathrm{T}}^{\mathrm{assoc}}$ and $p_{\mathrm{T}}^{\mathrm{jet}}$ bin, the $\Delta\phi$ distributions are divided by the $\Delta\phi|_{\mathrm{mix}}$ distributions to correct the shapes for detector acceptance. Because the triggers in this analysis are multi-particle objects instead of single charged hadrons, the mixed

event correction to the $\Delta\phi$ shapes is not as large as in dihadron correlations analyses (where TPC sector boundaries cause deep dips in the pair acceptance). Some other two-particle correlation analyses also use mixed events to correct for the $\Delta\eta$ shape of the correlation functions, shown in Fig. 4.6, but that is not done here. The correlation functions prior to background subtraction are shown in Appendix B, along with the magnitude of the mixed events correction.

4.5.2 The Associated Yields, Widths, and Mean p_{T}

Once the efficiency-corrected $\Delta\phi$ distributions have been calculated in each $p_{\mathrm{T}}^{\mathrm{jet,rec}}$ and $p_{\mathrm{T}}^{\mathrm{assoc}}$ bin, they are fit with a functional form in order to (statistically) separate the jet peaks from the heavy ion combinatoric background. The shapes of the $\Delta\phi$ distributions are assumed to have the following functional form:

$$\begin{aligned} &\frac{Y_{\mathrm{NS}}}{\sqrt{2\pi\sigma_{\mathrm{NS}}^2}} e^{-(\Delta\phi)^2/2\sigma_{\mathrm{NS}}^2} + \frac{Y_{\mathrm{AS}}}{\sqrt{2\pi\sigma_{\mathrm{AS}}^2}} e^{-(\Delta\phi-\pi)^2/2\sigma_{\mathrm{AS}}^2} \\ &+ B\left(1 + 2v_2^{\mathrm{assoc}}v_2^{\mathrm{jet}}\cos(2\Delta\phi) + 2v_3^{\mathrm{assoc}}v_3^{\mathrm{jet}}\cos(3\Delta\phi)\right) \end{aligned} \tag{4.4}$$

which consists of a Gaussian peak at $\Delta\phi = 0$ representing the nearside jet peak, a Gaussian centered at $\Delta\phi = \pi$ which represents the awayside jet peak, and a background term. In the fit function (although not shown in Eq. 4.4), the nearside peak is also present at $\Delta\phi = \pm 2\pi, \pm 4\pi, \pm 6\pi$ and the awayside at $\Delta\phi = -\pi, \pm 3\pi, \pm 5\pi, 7\pi$, so that the tails of the Gaussians wrap around properly. In p+p the background is a flat pedestal (no v_2 or v_3 terms), while in Au+Au it is assumed that the heavy-ion background is modulated by elliptic and "triangular" flow. If the associated hadrons and the trigger jets are each correlated with a common plane (the reaction plane or the participant planes), then the $\Delta\phi$ distributions will have a background shape modulated by the cross-terms $v_n^{\mathrm{assoc}}v_n^{\mathrm{jet}}$, which are shown in Eq. 4.4. The values of

$v_2^{\rm assoc}v_2^{\rm jet}$ and $v_3^{\rm assoc}v_3^{\rm jet}$ are discussed in detail in Section 4.6.

The raw $\Delta\phi$ distributions are fit by the function shown in Equation 4.4 to obtain the nearside yield ($Y_{\rm NS}$), nearside width ($\sigma_{\rm NS}$), awayside yield ($Y_{\rm AS}$), and awayside width ($\sigma_{\rm AS}$). The mean transverse momentum of the charged hadrons ($\langle p_{\rm T}^{\rm assoc}\rangle$) is also calculated in three regions in $\Delta\phi$-space: on the nearside ($-1 < \Delta\phi < 1$), on the awayside ($\pi - 1.3 < \Delta\phi < \pi + 1.3$), and in the background ($\frac{\pi}{3} < \Delta\phi < \frac{2\pi}{3}$). In some high-$p_{\rm T}^{\rm assoc}$ bins, $\langle p_{\rm T}^{\rm bkg}\rangle = 0$ because there are no tracks in the region $\frac{\pi}{3} < \Delta\phi < \frac{2\pi}{3}$; in these few cases $\langle p_{\rm T}^{\rm bkg}\rangle$ is set equal to $\langle p_{\rm T}^{\rm AS}\rangle$.

4.5.3 Nearside Yield and $\langle p_{\rm T}\rangle$ Correction in Au+Au

In Au+Au the nearside associated yield for $p_{\rm T}^{\rm assoc} > 2$ GeV/c is enhanced by background particles that are clustered into the jets. The mean $p_{\rm T}^{\rm assoc}$ on the nearside ($\langle p_{\rm T}^{\rm NS}\rangle$) is also affected by the inclusion of these particles. The values of $Y_{\rm NS}(p_{\rm T}^{\rm assoc})$ and $\langle p_{\rm T}^{\rm NS}\rangle$ are corrected using the background level, B, to estimate the number of background particles that fall within the jet cone. The estimated contribution from background fluctuations to the NS yield is given by:

$$\frac{1}{2}AB\left(1 + 2v_2^{\rm assoc}v_2^{\rm jet} + 2v_3^{\rm assoc}v_3^{\rm jet}\right) \tag{4.5}$$

where $A = \pi R^2 = \pi \times 0.4^2$ is the nominal size of the jet cone. The factor of $\frac{1}{2}$ accounts for the $\Delta\eta$ acceptance. Since the trigger jet axis falls in the range $|\eta| < 0.6$ and the associated particles are restricted to $|\eta| < 1.0$, the $\Delta\eta = \eta_{\rm assoc} - \eta_{\rm jet}$ acceptance has the shape shown in Figure 4.6. The integral of this curve is 2.0. Since B is a measure of $dN/d\Delta\phi$ (integrated over $\Delta\eta$), it is necessary to divide by 2 to obtain a measure of $d^2N/d\Delta\phi d\Delta\eta$. Then by multiplying by A (an area in $\Delta\phi$–$\Delta\eta$ space), an estimate of the number of background particles within the jet cone can be obtained.

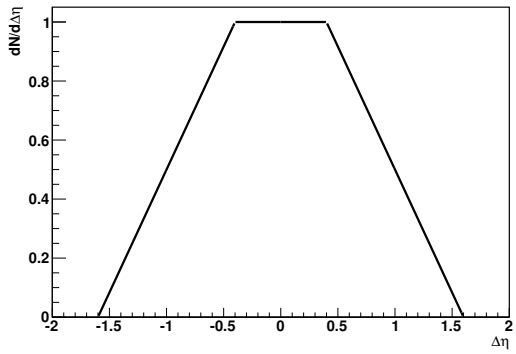

Figure 4.6: A cartoon showing the ideal $\Delta\eta = \eta_{\rm assoc} - \eta_{\rm jet}$ acceptance given $|\eta_{\rm jet}| < 0.6$ and $|\eta_{\rm assoc}| < 1.0$.

Therefore, in $p_{\rm T}^{\rm assoc}$ bins above 2 GeV/c, the fit function (Equation 4.4) is replaced by:

$$\left(Y_{\rm NS} + \frac{1}{2}AB\left(1 + 2v_2^{\rm assoc}v_2^{\rm jet} + 2v_3^{\rm assoc}v_3^{\rm jet}\right)\right)\frac{1}{\sqrt{2\pi\sigma_{\rm NS}^2}}e^{-(\Delta\phi)^2/2\sigma_{\rm NS}^2} \tag{4.6}$$
$$+ \frac{Y_{\rm AS}}{\sqrt{2\pi\sigma_{\rm AS}^2}}e^{-(\Delta\phi-\pi)^2/2\sigma_{\rm AS}^2} + B\left(1 + 2v_2^{\rm assoc}v_2^{\rm jet}\cos(2\Delta\phi) + 2v_3^{\rm assoc}v_3^{\rm jet}\cos(3\Delta\phi)\right)$$

The nearside mean $p_{\rm T}$ is adjusted by the following formula:

$$\langle p_{\rm T}^{\rm NS,new}\rangle Y_{\rm NS} = \langle p_{\rm T}^{\rm NS,old}\rangle\left(Y_{\rm NS} + \frac{1}{2}AB\left(1 + 2v_2^{\rm assoc}v_2^{\rm jet} + 2v_3^{\rm assoc}v_3^{\rm jet}\right)\right) \tag{4.7}$$
$$- \frac{1}{2}AB\left(1 + 2v_2^{\rm assoc}v_2^{\rm jet} + 2v_3^{\rm assoc}v_3^{\rm jet}\right)\langle p_{\rm T}^{\rm bkg}\rangle$$

The nearside yield and $\langle p_{\rm T}\rangle$ correction only has a large effect in the first $p_{\rm T}^{\rm assoc}$ bin above $p_{\rm T}^{\rm assoc} = 2$ GeV/c. In the higher $p_{\rm T}^{\rm assoc}$ bins the background level is small and therefore so is the correction.

4.6 Background Subtraction

Jet v_2 and v_3 are *a priori* unknown, so the approach in this analysis is to display the results under two extreme and opposite assumptions, while placing conservative uncertainties on the values of $v_2^{\rm assoc}v_2^{\rm jet}$ and $v_3^{\rm assoc}v_3^{\rm jet}$. The two assumptions are the same as those used to place uncertainties on the jet energy scale (Section 4.4):

1. *HT trigger jets in Au+Au are unmodified compared to HT trigger jets in* p+p. When fitting the $\Delta\phi$ distributions with the functional form in (4.4) the nearside yields and widths in Au+Au are fixed to the values measured in *p+p*, $v_2^{\rm assoc}v_2^{\rm jet}$ is fixed to a mean value and $v_3^{\rm assoc}v_3^{\rm jet}$ is left as a free parameter. The mean $v_2^{\rm assoc}$ is estimated to be the average of $v_2\{\text{FTPC}\}(p_{\rm T}^{\rm assoc})$ and $v_2\{4\}(p_{\rm T}^{\rm assoc})$, while $v_2^{\rm jet}$ is estimated to be $v_2\{\text{FTPC}\}(6\ \text{GeV}/c)$, where $v_2\{\text{FTPC}\}(p_{\rm T})$ and $v_2\{4\}(p_{\rm T})$ are obtained using a parameterization [62] from MB data [63]. Here, $v_2\{\text{FTPC}\}$ is estimated with respect to the event plane determined in the FTPCs and $v_2\{4\}$ is determined using the 4-particle cumulant method [64]. The systematic uncertainties are determined by fixing $v_2^{\rm assoc}v_2^{\rm jet}$ to maximum and minimum values while letting $v_3^{\rm assoc}v_3^{\rm jet}$ float to force the Au+Au nearside yields to match *p+p*. The lower and upper limits on $v_2^{\rm assoc}$ are estimated to be $v_2\{4\}(p_{\rm T}^{\rm assoc})$ and $v_2\{\text{FTPC}\}(p_{\rm T}^{\rm assoc})$, respectively. The bounds on $v_2^{\rm jet}$ are conservatively estimated to be 70% and 130% of $v_2\{\text{FTPC}\}(6\ \text{GeV}/c)$.

2. *HT trigger jets in Au+Au are maximally modified compared to HT trigger jets in* p+p. The background assumption that produces the largest nearside yields and widths is $v_2^{\rm assoc}v_2^{\rm jet} = 0$ and $v_3^{\rm assoc}v_3^{\rm jet} = 0$. (The possibility that $v_2^{\rm jet} < 0$ or $v_3^{\rm jet} < 0$ is not considered.)

The $v_2^{\rm assoc}v_2^{\rm jet}$ and $v_3^{\rm assoc}v_3^{\rm jet}$ values that arise from each of these possibilities are shown in Figs. 4.7 and 4.8, respectively. As a cross-check, the $v_2^{\rm assoc}v_2^{\rm jet}$ and $v_3^{\rm assoc}v_3^{\rm jet}$

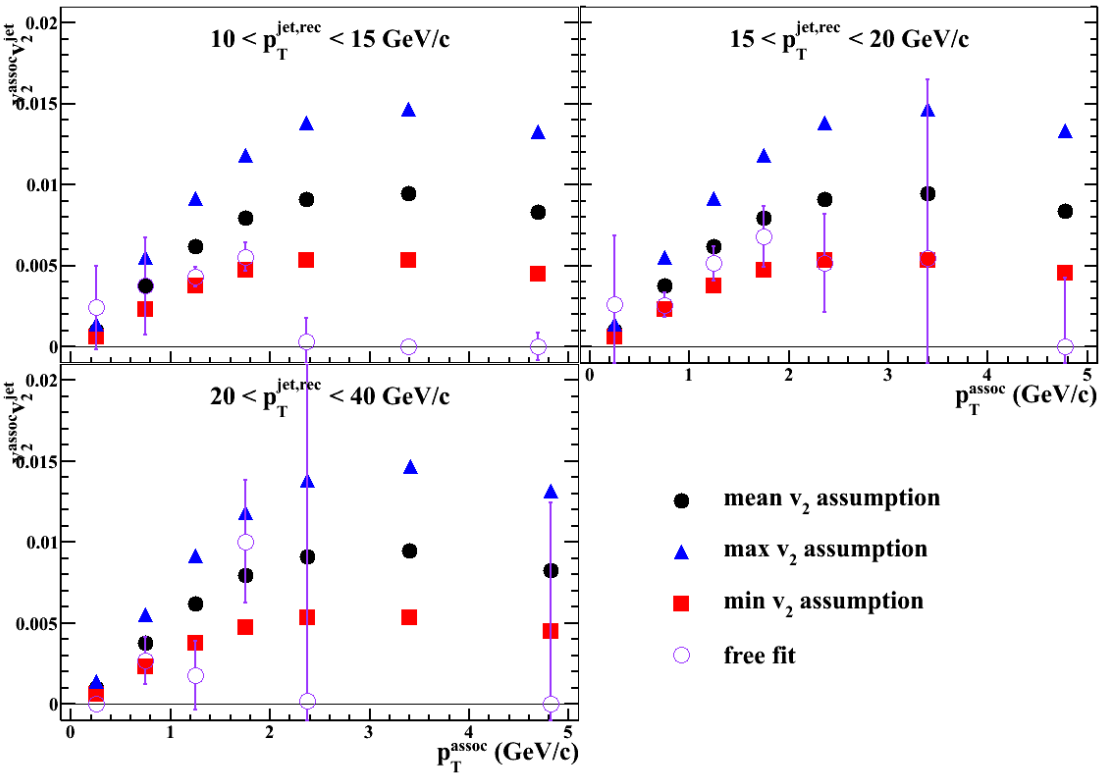

Figure 4.7: The $v_2^{\rm assoc}v_2^{\rm jet}$ values used in the fit function (Eq. 4.4) are shown under the assumptions described in Section 4.6. Also shown are the $v_2^{\rm assoc}v_2^{\rm jet}$ values extracted from a free fit to the correlation functions (when the NS yields and widths are matched between Au+Au and p+p, but both $v_2^{\rm assoc}v_2^{\rm jet}$ and $v_3^{\rm assoc}v_3^{\rm jet}$ are free parameters).

values from a free fit are also shown, and it is good to see that they fall between the imposed minimum and maximum values. The $v_3^{\rm assoc}v_3^{\rm jet}$ values that result from the fits are reasonable compared to the data in [23, 65]. Note that as $p_{\rm T}^{\rm assoc}$ increases, the background level B drops dramatically and therefore large uncertainties in the fitted values of $v_2^{\rm assoc}v_2^{\rm jet}$ and $v_3^{\rm assoc}v_3^{\rm jet}$ are possible without having a significant impact on the final result. Examples of the background-subtracted $\Delta\phi$ correlation function are shown in Fig. 4.9.

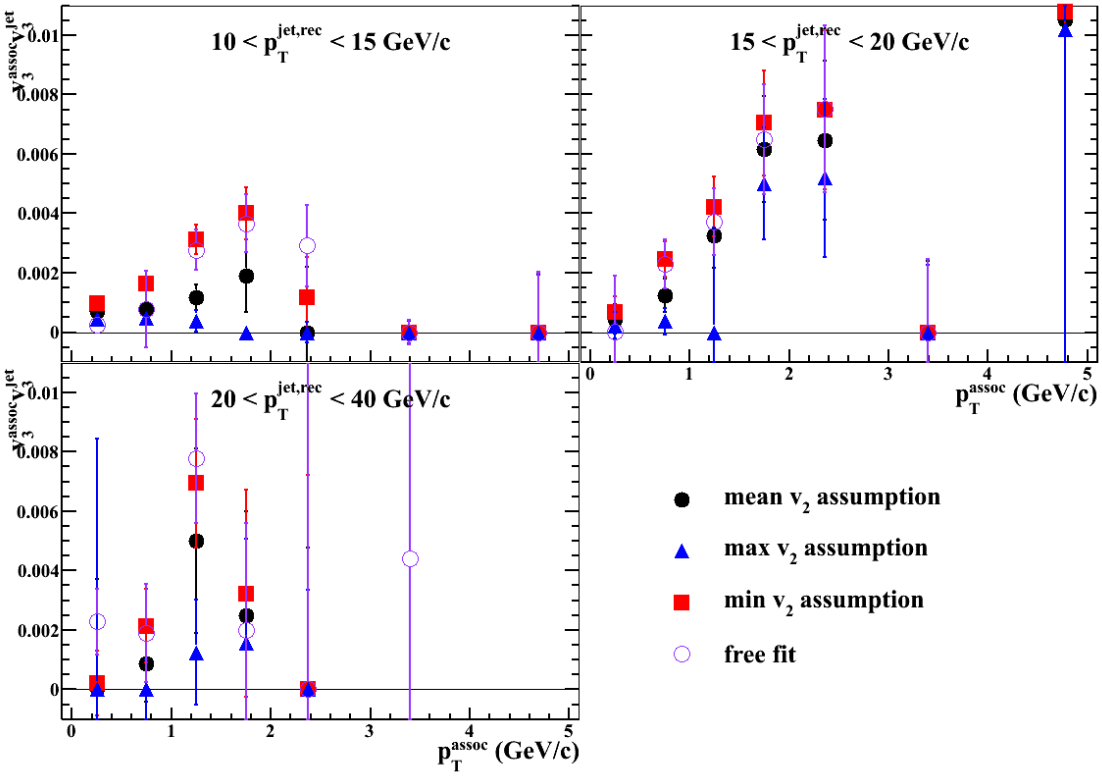

Figure 4.8: The $v_3^{\text{assoc}} v_3^{\text{jet}}$ values used in the fit function (Eq. 4.4) are shown under the assumptions described in Section 4.6. Also shown are the $v_3^{\text{assoc}} v_3^{\text{jet}}$ values extracted from a free fit to the correlation functions (when the NS yields and widths are matched between Au+Au and p+p, but both $v_2^{\text{assoc}} v_2^{\text{jet}}$ and $v_3^{\text{assoc}} v_3^{\text{jet}}$ are free parameters).

4.7 Detector Effects and Their Uncertainties

Since this analysis only concerns the comparison of equivalent Au+Au and p+p jets, and not absolute physical quantities (such as the parent parton energy), the relevant detector efficiencies are only those that are different between the two collision systems or between 2006 and 2007. The effects of the various detector efficiencies on the jet energy scale are taken into account in the p+p HT $\otimes$ Au+Au MB embedding. By changing the parameters used in the embedding study, it is possible to investigate the effects of several detector-related systematic uncertainties on the correspondence

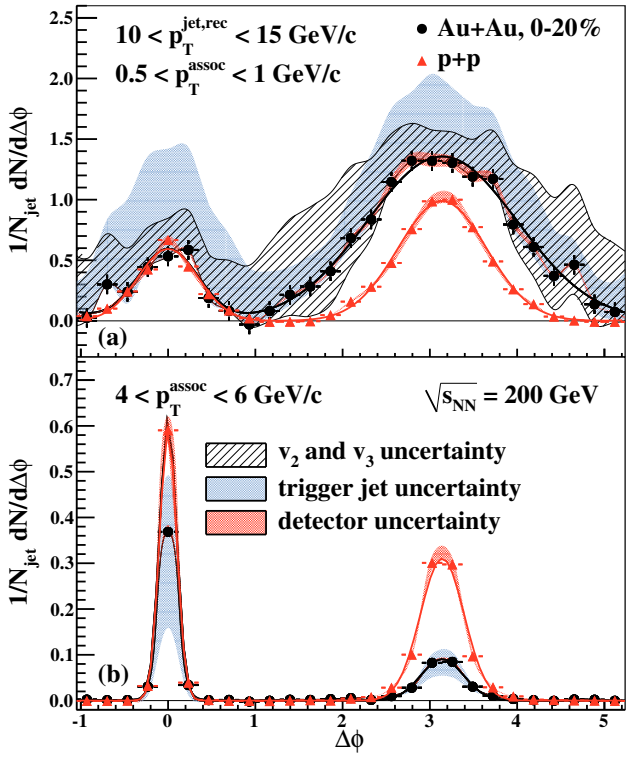

Figure 4.9: Jet-hadron correlations after background subtraction for $10 < p_{\mathrm{T}}^{\mathrm{jet,rec}} < 15$ GeV/c and for two ranges in $p_{\mathrm{T}}^{\mathrm{assoc}}$: (a) $0.5 < p_{\mathrm{T}}^{\mathrm{assoc}} < 1$ GeV/c and (b) $4 < p_{\mathrm{T}}^{\mathrm{assoc}} < 6$ GeV/c. The data points from Au+Au and p+p collisions are shown with Gaussian fits to the jet peaks and systematic uncertainty bands due to: tracking efficiency, the shape of the combinatoric background, and the trigger jet energy scale.

between p+p and Au+Au jet energies, and consequently on the jet-hadron correlations themselves. The effects that were studied and the subsequent results are listed here:

1. The tracking efficiency in Au+Au is 90%$\pm$7% of that in p+p for $p_{\mathrm{T}} > 2$ GeV/c (see Appendix A). In order to reflect this in the p+p HT $\otimes$ Au+Au MB embedding, 10% of the tracks in the p+p event are randomly rejected before calculating $p_{\mathrm{T}}^{p+p,\mathrm{emb}}$.

   In order to calculate the systematic uncertainty bands corresponding to the uncertainty on the tracking efficiency, the p+p HT $\otimes$ Au+Au MB embedding is redone with 17% and 3% of the tracks being rejected, and the extracted Gaussian yields (Y_{NS} and Y_{AS}) are also adjusted to account for the possible variation in tracking efficiency.

2. The tower efficiency in Au+Au is 98% $\pm$ 2% that in p+p. In order to reflect

this in the p+p HT $\otimes$ Au+Au MB embedding, 2% of towers in the p+p event are randomly rejected.

To calculate the systematic uncertainty bands corresponding to the uncertainty on the tower efficiency, the p+p HT $\otimes$ Au+Au MB embedding is redone with 4% and 0% of the towers being rejected. The tower efficiency and its uncertainty are negligible effects.

3. The tower energy scale uncertainty between 2006 and 2007 is $\pm 2\%$ [66]. To obtain an uncertainty band for the tower energy scale, the energy of every tower is adjusted up and down by 2% when calculating the reconstructed jet energy in the p+p HT $\otimes$ Au+Au MB embedding.

4. The "cross" hadronic correction, in which charged hadron tracks from the Au+Au MB event point towards neutral towers from the p+p event, should in principal be taken into account. However, matching tracks to towers between different events is difficult in the current analysis framework. A simple mock-up of the cross hadronic correction was attempted, in which an average momentum (~ 0.5 GeV/$c - 1$ GeV/c) was subtracted from a fraction ($25\% - 100\%$) of the towers. Varying the average momentum and tower fraction did not change the shape of the jet spectrum significantly. In the final embedding the cross hadronic correction was not included.

5. The analysis was redone using a MIP correction instead of the 100% hadronic correction. Instead of subtracting the track momentum from the tower energy whenever a track is matched to a tower, the amount of energy deposited by a minimum ionizing particle is subtracted, which is parameterized by Eq. 4.8 [67].

(In both cases, towers associated with electrons are rejected.)

$$\text{MIP} = 0.261 \text{ GeV} \times \frac{1 + 0.056\eta^2}{\sin\theta} \tag{4.8}$$

Although the MIP correction changes the shape of the jet p_{T} spectrum, it does not have a major effect on the final correlation functions. Since the 100% hadronic correction and MIP correction are essentially two extreme and opposite ways of correcting for charged hadron double-counting in the BEMC, it is believed that the hadronic correction scheme does not introduce a large uncertainty in the final results.

4.8 Results

The nearside associated yields and Gaussian widths are shown for three ranges in the reconstructed jet p_{T} in Fig. 4.10. Systematic uncertainties are shown only on the Au+Au points, since all systematics are defined relative to p+p. The only uncertainty on the nearside is the ΣD_{AA} shift uncertainty on the jet energy scale, since the uncertainties related to detector performance and on the background shape (v_2 and v_3) are defined under the assumption that the nearside yields and widths are equivalent in p+p and Au+Au.

The awayside yields, widths, I_{AA}, and D_{AA} are shown in Figs. 4.11 and 4.12. Uncertainties due to detector performance (relative tracking efficiency, tower efficiency, and tower energy scale), the shape of the background (v_2 and v_3), and the jet energy scale (ΔE and ΣD_{AA} shifts), are also shown. The awayside ΣD_{AA} is shown in Table 4.2, with its associated uncertainties. Also shown for reference in Table 4.2 is the quantity $\Sigma D_{AA}^{>}$, which is $D_{AA}(p_{\text{T}}^{\text{assoc}})$ summed over only $p_{\text{T}}^{\text{assoc}} > 2$ GeV/c.

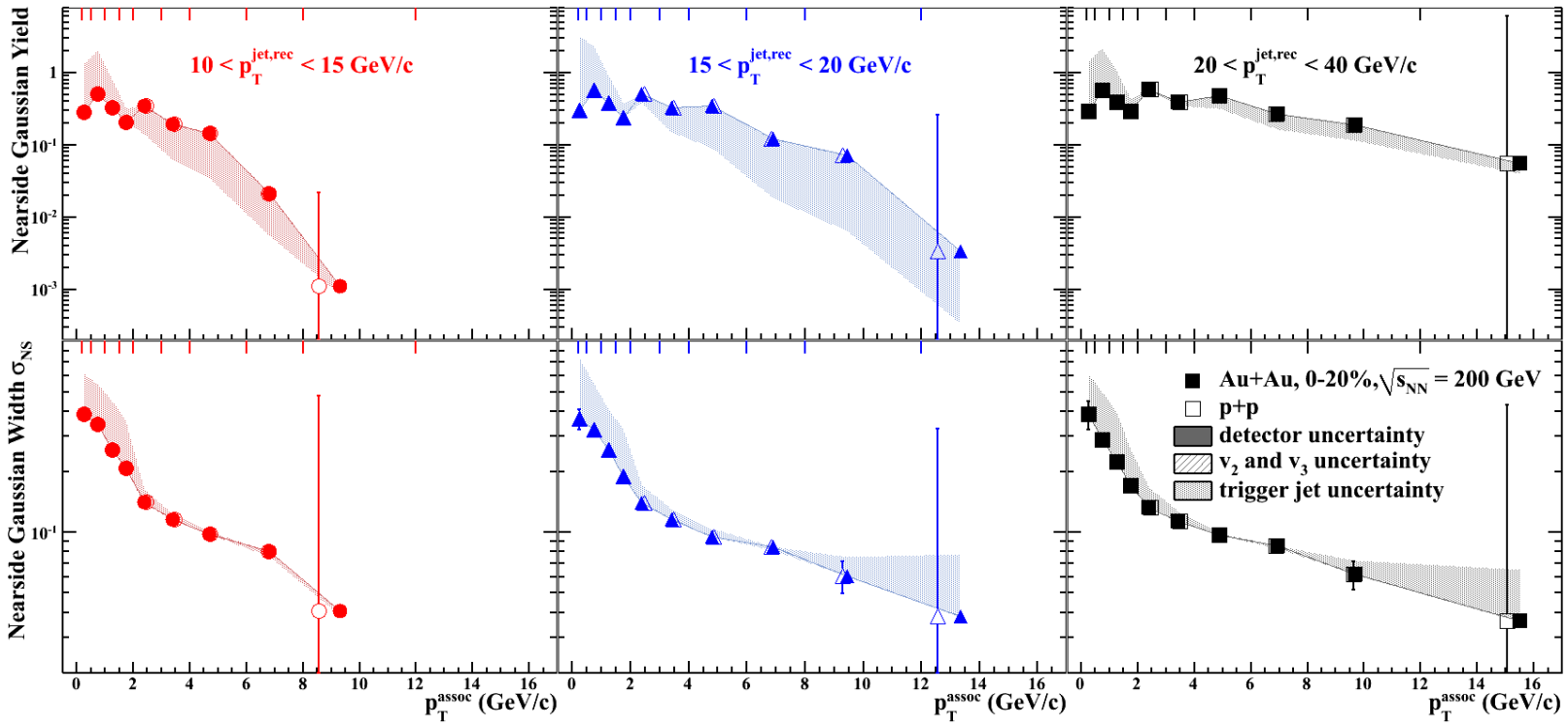

Figure 4.10: The nearside associated hadron yields (Y_{NS}, top row) and widths (σ_{NS}, bottom row) in Au+Au (solid symbols) and p+p (open symbols) are shown as a function of $p_{\mathrm{T}}^{\mathrm{assoc}}$ for three ranges in the reconstructed jet p_{T}. The boundaries of the $p_{\mathrm{T}}^{\mathrm{assoc}}$ bins are shown along the upper axes, and the points are plotted at the value of $\langle p_{\mathrm{T}}^{\mathrm{assoc,NS}} \rangle$ in each bin.

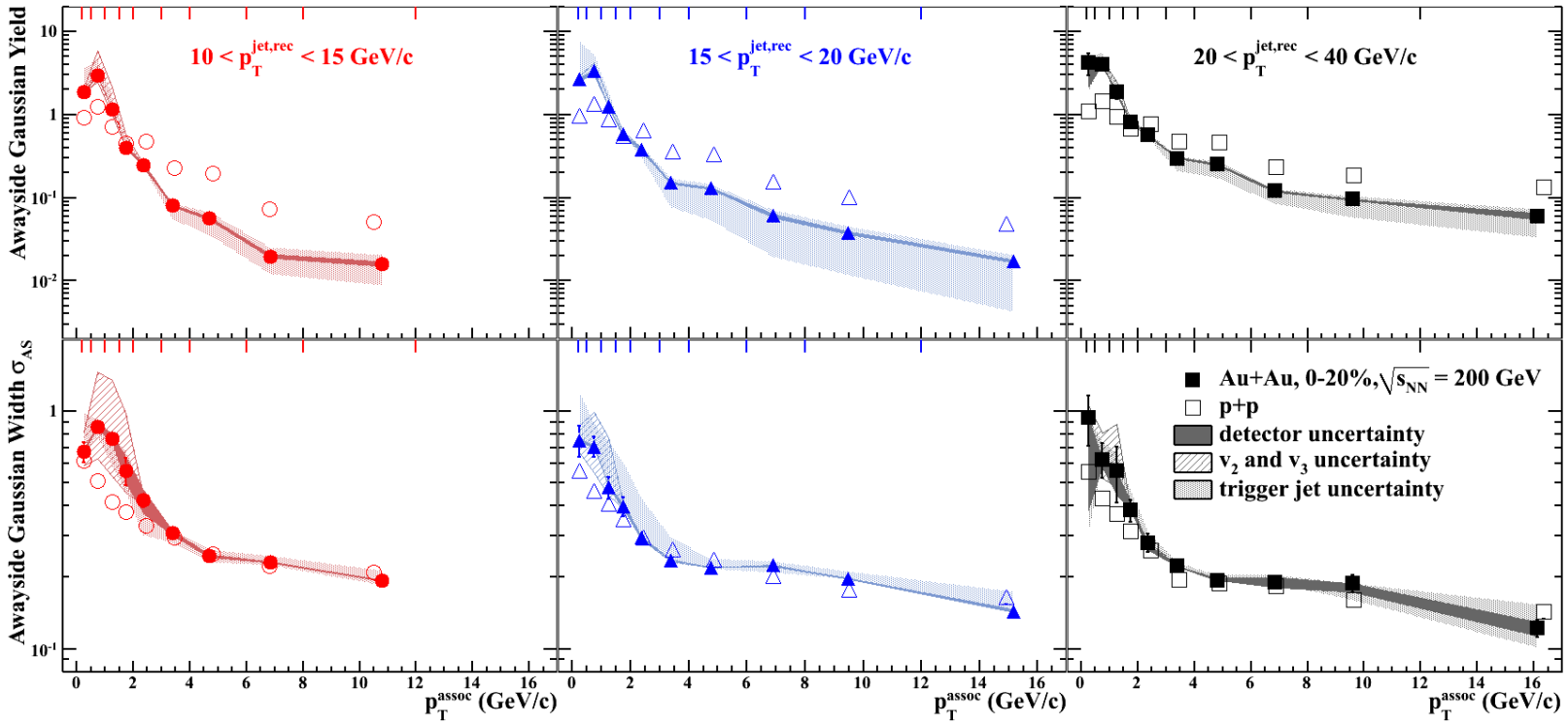

Figure 4.11: The awayside associated hadron yields (Y_{AS}, top row) and widths (σ_{AS}, bottom row) in Au+Au (solid symbols) and p+p (open symbols) are shown as a function of $p_{\mathrm{T}}^{\mathrm{assoc}}$ for three ranges in the reconstructed jet p_{T}. The boundaries of the $p_{\mathrm{T}}^{\mathrm{assoc}}$ bins are shown along the upper axes, and the points are plotted at the value of $\langle p_{\mathrm{T}}^{\mathrm{assoc,AS}} \rangle$ in each bin.

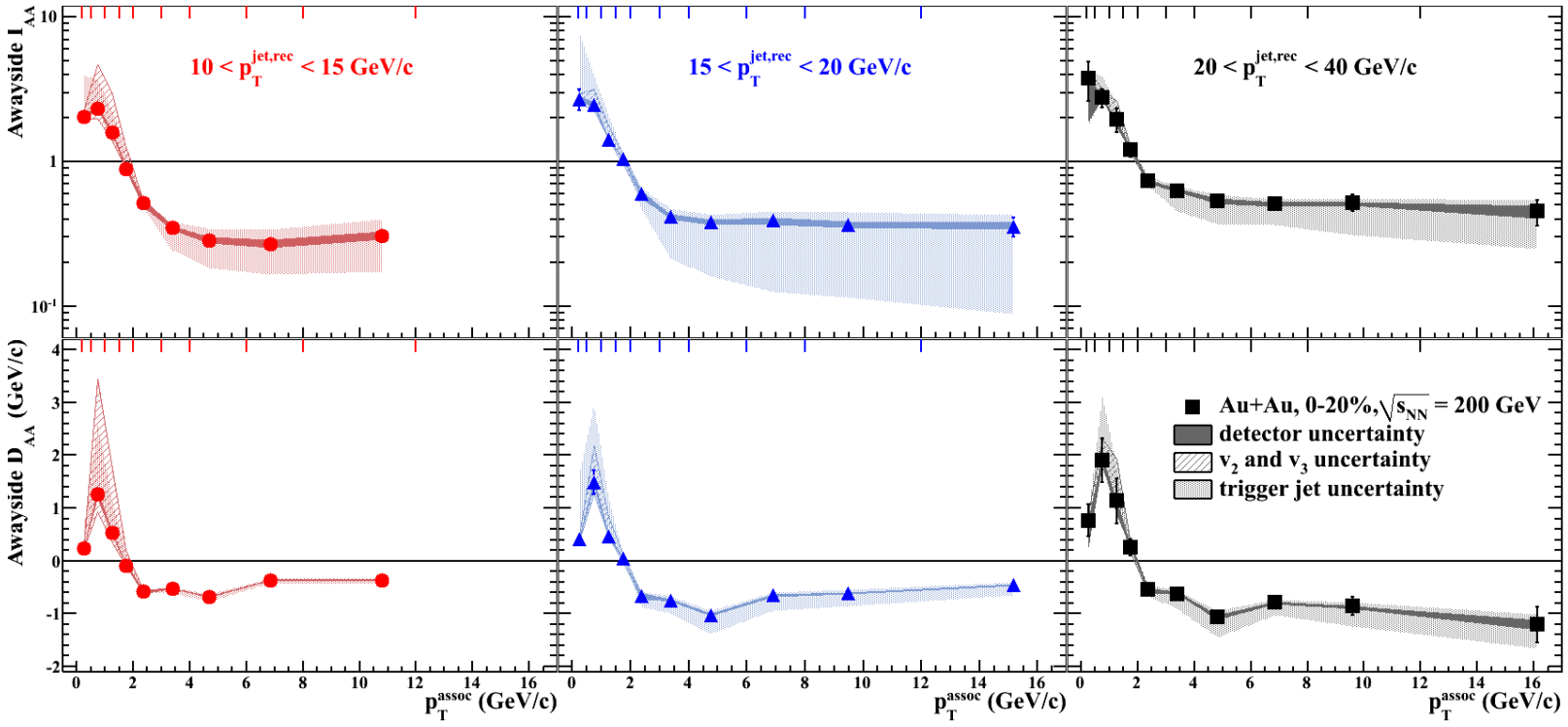

Figure 4.12: The ratio of hadron yields in Au+Au compared to p+p (I_{AA}, top row) and the energy difference between Au+Au and p+p (D_{AA}, bottom row) on the awayside is shown as a function of $p_{\mathrm{T}}^{\mathrm{assoc}}$ for three ranges in the reconstructed jet p_{T}. The boundaries of the $p_{\mathrm{T}}^{\mathrm{assoc}}$ bins are shown along the upper axes, and the points are plotted at the value of $\langle p_{\mathrm{T}}^{\mathrm{assoc,AS}} \rangle$ in each bin.

$p_{\mathrm{T}}^{\mathrm{jet,rec}}$ (GeV/c)	ΣD_{AA} (GeV/c)	Detector Uncert.	v_2 and v_3 Uncert.	Jet Energy Scale Uncert.	$\Sigma D_{AA}^{>}$ (GeV/c)
$10-15$	-0.6 ± 0.2	$^{+0.2}_{-0.2}$	$^{+3.7}_{-0.5}$	$^{+2.3}_{-0.0}$	-2.5
$15-20$	-1.8 ± 0.3	$^{+0.3}_{-0.3}$	$^{+1.0}_{-0.0}$	$^{+1.9}_{-0.0}$	-4.2
$20-40$	-1.0 ± 0.8	$^{+0.1}_{-0.8}$	$^{+1.2}_{-0.1}$	$^{+0.3}_{-0.0}$	-5.1

Table 4.2: Awayside ΣD_{AA} values with statistical and systematic uncertainties due to detector effects, the shape of the combinatoric background, and the trigger jet energy scale. $\Sigma D_{AA}^{>}$, which is only calculated for $p_{\mathrm{T}}^{\mathrm{assoc}} > 2$ GeV/c, measures the high-p_{T} suppression.

Low-p_{T} enhancement and high-p_{T} suppression of the awayside associated hadron yields in Au+Au compared to p+p are clearly visible in Figs. 4.11 and 4.12. The awayside widths suggest low-p_{T} broadening, particularly in the $10 < p_{\mathrm{T}}^{\mathrm{jet,rec}} < 15$ GeV/c range (the uncertainty bands in the other $p_{\mathrm{T}}^{\mathrm{jet,rec}}$ bins are too large to be conclusive). Furthermore, at high-p_{T}, the awayside Gaussian widths are equivalent in p+p and Au+Au, indicating that jets containing high-p_{T} hadrons do not undergo much deflection as they traverse the QGP. As seen in Table 4.2, in each jet p_{T} range the ΣD_{AA} values are small compared to the reconstructed jet energies and compared to $\Sigma D_{AA}^{>}$, indicating that the high-p_{T} suppression is in large part balanced by the low-p_{T} enhancement.

4.9 Comparison to Theory

In Fig. 4.13, theoretical calculations for σ_{AS} and D_{AA} within the YaJEM-DE model are compared to data in two jet p_{T} ranges: $10 < p_{\mathrm{T}}^{\mathrm{jet,rec}} < 15$ GeV/c and $20 < p_{\mathrm{T}}^{\mathrm{jet,rec}} < 40$ GeV/c. YaJEM-DE [68, 69, 70, 71] is a Monte Carlo model of in-medium shower evolution that incorporates radiative and elastic energy loss, and describes many high-p_{T} observables from RHIC. After the intrinsic transverse momentum imbalance, k_{T}, of the initial hard scattering was tuned to provide the best fit to the p+p yields

($Y_{\mathrm{AS},p+p}$), this model largely reproduces several of the quantitative and qualitative features observed in data. At high $p_{\mathrm{T}}^{\mathrm{assoc}}$ the Au+Au and p+p widths match and the jet yields are suppressed, while the missing energy appears as an enhancement and broadening of the soft jet fragments.

In [72], the fragmentation and propagation of a high-energy jet through a medium is modeled in a (1+1) quasi-Abelian Schwinger theory, which incorporates medium-induced perturbative gluon radiation. In particular, this model was utilized to investigate the screening effects of a comoving gluon on the energy loss of a parton traversing the medium. It was demonstrated that this model can describe the fragmentation functions measured by CMS in Pb+Pb collisions at $\sqrt{s_{NN}} = 2.76$ TeV, which initially seemed to contradict radiative energy loss expectations because suppression was observed at intermediate $\zeta = ln(1/z) = ln(p_{\mathrm{T}}^{\mathrm{jet}}/p_{\mathrm{T}}^{\mathrm{hadron}})$. As shown in Fig. 4.14, this model can also describe the $D_{AA}(p_{\mathrm{T}}^{\mathrm{assoc}})$ measured in the jet-hadron correlations analysis.

The results of the jet-hadron correlations analysis are qualitatively consistent with a picture of medium-induced parton modification through radiative energy loss, which predicts the softening and broadening of jets that traverse the QGP. Furthermore, the data are quantitatively consistent with two models that implement radiative energy loss in dramatically different ways.

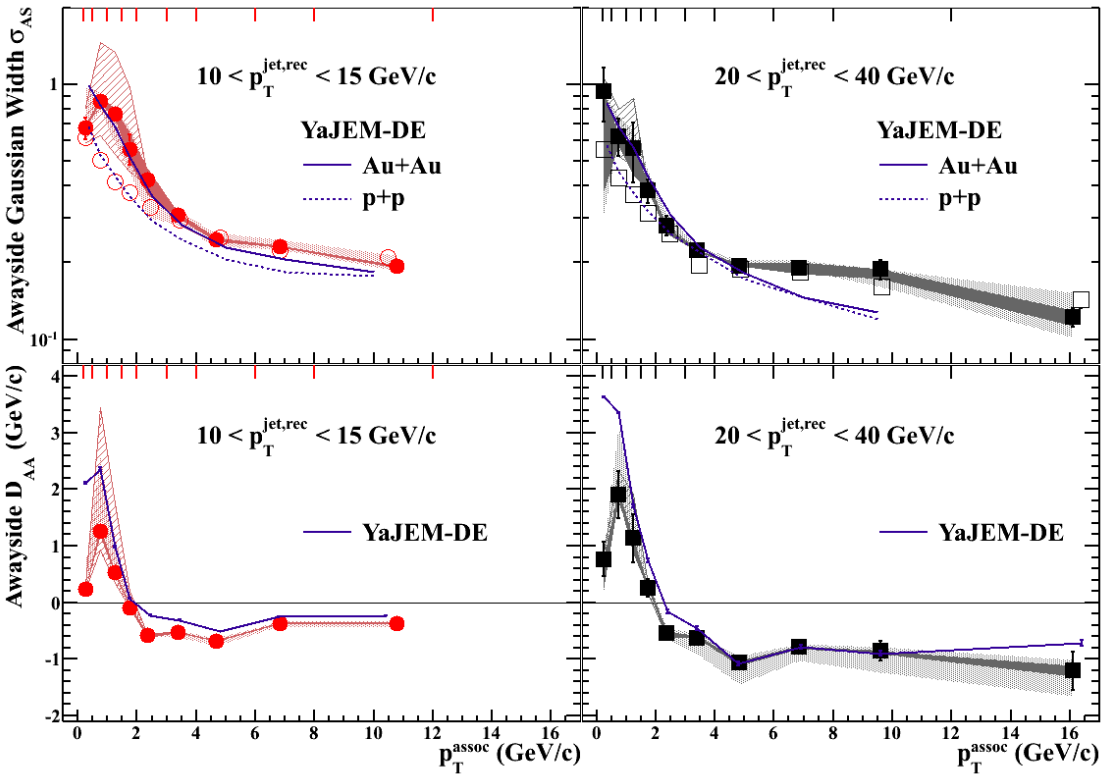

Figure 4.13: Theoretical calculations for σ_{AS} (top row) and $D_{AA}(p_{\mathrm{T}}^{\mathrm{assoc}})$ (bottom row) within the YaJEM-DE model are compared to data in two jet p_{T} ranges: $10 < p_{\mathrm{T}}^{\mathrm{jet,rec}} < 15$ GeV/c and $20 < p_{\mathrm{T}}^{\mathrm{jet,rec}} < 40$ GeV/c. [73]

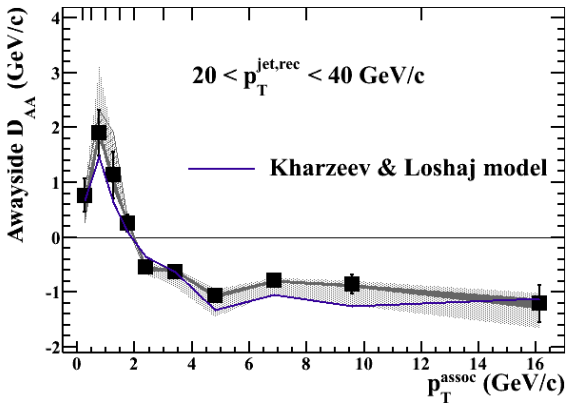

Figure 4.14: A theoretical calculation for $D_{AA}(p_{\mathrm{T}}^{\mathrm{assoc}})$ within a (1+1) quasi-Abelian Schwinger theory is compared to data for $20 < p_{\mathrm{T}}^{\mathrm{jet,rec}} < 40$ GeV/c. [74]

Chapter 5

Jet v_2

When a hard scattering occurs in the early stages of a heavy ion collision, the emission angle in the transverse plane of the back-to-back partons is expected to be independent of the QGP geometry. However, it is likely that medium-induced parton energy loss depends on the length of the parton's path through the QGP [75], and therefore should depend on the geometry of the underlying medium, which is associated with the reaction plane and participant planes. In particular, theoretical models indicate that the in-medium pathlength depends on the relative angle between the parton emission angle and the reaction plane, such that the pathlength is on-average shorter when the parton is emitted in-plane than when the parton is emitted out-of-plane [76], since the matter distribution is compressed in the direction of the participant plane and elongated in the direction perpendicular to the participant plane, as shown in Fig. 2.1. Thus, pathlength-dependent jet suppression could give rise to a difference in the number of reconstructed jets and their momenta in the direction of the event plane and out of the event plane. This effect would result in a correlation between reconstructed jets and the n^{th}-order participant planes, leading to v_n coefficients in a Fourier series representation of the azimuthal distribution of

the reconstructed jet axes (Ψ_{jet}):

$$\frac{\mathrm{d}N}{\mathrm{d}\left(\Psi_{\text{jet}} - \Psi_{\text{PP},m}\right)} \propto 1 + \sum_{n=1}^{\infty} 2v_n^{\text{jet}} \cos\left[n\left(\Psi_{\text{jet}} - \Psi_{\text{PP},m}\right)\right] \tag{5.1}$$

in analogy with Eq. 2.2. Following from Eq. 5.1, jet v_n can be defined with respect to the m^{th}-harmonic participant plane as:

$$v_n^{\text{jet}} = \left\langle \cos\left(n(\Psi_{\text{jet}} - \Psi_{\text{PP},m})\right)\right\rangle \tag{5.2}$$

Jet v_n can be defined similarly with respect to the reaction plane:

$$v_n^{\text{jet}} = \left\langle \cos\left(n(\Psi_{\text{jet}} - \Psi_{\text{RP}})\right)\right\rangle \tag{5.3}$$

Jet v_n describes the correlation between the jet axis and the reaction plane or participant planes, and should not be confused with a measure of the intrajet correlation of jet fragments. Furthermore, non-zero jet v_n does not necessarily indicate that jets experience hydrodynamic flow, since pathlength-dependent energy loss is a more likely physical explanation. "Jet v_n," which describes a correlation between the jet and the collision geometry, should be distinguished from pressure-driven "jet flow," which imposes a physical interpretation on any such correlation.

A measurement of jet v_n, and particularly jet v_2, would provide information for theories of parton-medium interactions and the pathlength-dependence of parton energy loss. Since jets experiencing varying amounts of medium-induced modification can be selected with different jet reconstruction parameters (such as constituent p_{T} cuts and the resolution parameter R) a measurement of jet v_2 can also lead to insights into the biases involved in jet finding. This chapter will describe the first attempt to measure jet v_2 in heavy-ion collisions using Au+Au collisions at $\sqrt{s_{NN}} = 200$ GeV

in STAR.

5.1 The Event Plane Method of Measuring v_2

One of the methods for measuring v_2 (or more generally, v_n) is by reconstructing the 2^{nd}-harmonic event plane, and then calculating the correlation between the object of interest (in this case, a jet) and the event plane, averaged over a large sample of events.

The standard method of calculating the event plane [77] is by defining a flow vector, $\mathbf{Q}_2$, that describes the bulk particle distribution. The components of $\mathbf{Q}_2$ are shown in (5.4),

$$Q_{2,x} = \sum_i w_i \cos(2\phi_i) = Q_2 \cos(2\Psi_{\mathrm{EP},2}) \tag{5.4}$$
$$Q_{2,y} = \sum_i w_i \sin(2\phi_i) = Q_2 \sin(2\Psi_{\mathrm{EP},2})$$

where the index i runs over all the particles used in the event plane reconstruction. The vector $\mathbf{Q}_2$ and the beam axis define the event plane, and the azimuthal angle of the event plane can therefore be calculated using Eq. 5.5:

$$\Psi_{\mathrm{EP},2} = \frac{1}{2}\tan^{-1}\left(\frac{\sum_i w_i \sin(2\phi_i)}{\sum_i w_i \cos(2\phi_i)}\right) \tag{5.5}$$

where the index i runs over all particles and the weights w_i are chosen to maximize the event plane resolution.

Once the angle of the event plane is known, jet v_2 can be calculated with the

following formula, which follows from Eq. 5.2:

$$v_2^{\text{jet}}\{\text{EP}\} \equiv \langle \cos\left(2(\Psi_{\text{jet}} - \Psi_{\text{PP,2}})\right)\rangle = \frac{\langle \cos\left(2(\Psi_{\text{jet}} - \Psi_{\text{EP,2}})\right)\rangle}{\langle \cos\left(2(\Psi_{\text{EP,2}} - \Psi_{\text{PP,2}})\right)\rangle} \tag{5.6}$$

where the denominator $\langle \cos\left(2(\Psi_{\text{EP,2}} - \Psi_{\text{PP,2}})\right)\rangle$ is the event plane resolution (the correlation between the reconstructed event plane and the underlying participant plane). Thus a measurement of jet v_2 requires three ingredients: the azimuthal angle of a reconstructed jet (discussed in Section 5.2), the angle of the event plane (Section 5.3), and the event plane resolution (Section 5.4).

5.2 The Data Set and Jet Definition

The data set analyzed in the jet v_2 study is the same as that described in Section 4.2, with two exceptions: (1) a wider centrality range (0-50%) was analyzed, and (2) the offline HT threshold was lowered from $E_{\text{T}} > 6$ GeV to $E_{\text{T}} > 5.5$ GeV in order to increase statistics (and since a comparison between Au+Au and p+p is not necessary). Jets are reconstructed as described in Section 4.3 in order to obtain the angle of the jet axis (Ψ_{jet},η_{jet}) and the reconstructed jet p_{T}.

5.3 Event Plane Reconstruction

Unfortunately, if jet fragments are included in the event plane calculation it will cause the reconstructed event plane to be biased towards the jet axis. While the bias may be small on an event-by-event basis, it can cause a significant overestimation of the jet v_2. This effect is demonstrated in a simple simulation in Fig. 5.1, in which events consist of a PYTHIA [78, 79] (p+p-like) jet event embedded into a thermal background. The background is modulated by elliptic flow with respect to

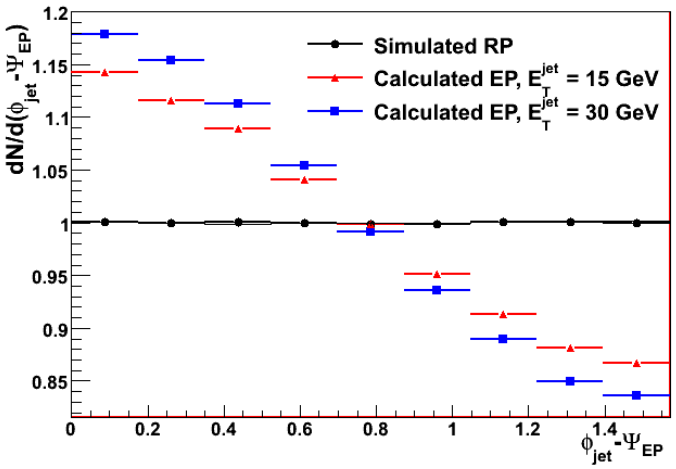

Figure 5.1: The jet – event plane bias is demonstrated in simulated events consisting of a PYTHIA jet embedded in a thermal background ($T = 0.291$ GeV). The p_{T}- and centrality-dependent v_2 values and multiplicities of the background are consistent with observations from STAR in the 10-20% centrality bin [63, 80]. The jet axes are uncorrelated with the simulated reaction planes (black circles), but when the event plane is reconstructed in the presence of a $E_{\mathrm{T}}^{\mathrm{jet}} = 15$ GeV jet (red triangles) or a $E_{\mathrm{T}}^{\mathrm{jet}} = 30$ GeV jet (blue squares), a significant correlation is observed.

a simulated reaction plane, and the axis of the embedded jet is not correlated with the reaction plane. However, when the event plane is reconstructed using Eq. 5.5, it is observed that the event plane is significantly more likely to be reconstructed in the direction of the jet axis than perpendicular to the jet axis. In this simulation, the jet – event plane bias results in an artificial jet v_2 of nearly 10%. Further studies show that even very small numbers of correlated particles (low jet multiplicities) can cause a non-negligible artificial jet v_2.

This jet – event plane bias can be reduced or avoided by introducing a pseudorapidity (η) gap between the jet (and the recoil jet) and the particles used to calculate the event plane, which is made possible by the forward detector capabilities of STAR. In this analysis, the event plane is reconstructed in three detector sub-systems covering different η ranges: the TPC covers midrapidity ($|\eta| < 1$), while the FTPCs measure charged tracks in $2.8 < |\eta| < 3.7$, and ZDC-SMDs measure the energy de-

position of spectator neutrons with $|\eta| > 6.3$. Since the axes of the reconstructed jets are restricted to within $|\eta_{\rm jet}| < 0.6$, the FTPC and ZDC-SMD allow η gaps of $|\Delta\eta| > 2.2$ and $|\Delta\eta| > 5.7$, respectively, between the jet axis and the particles used to determine the event plane. The widths of the trigger jets shown in Fig. 4.10 indicate that these η gaps are sufficient to prevent fragments of the reconstructed jet from being included in the event plane calculation. However, since the recoil jet is not reconstructed, its η range is not restricted, and the possibility that fragments of the recoil jet impinge upon the forward detectors must be considered. Evidence from a simple PYTHIA simulation indicates that the probability of the recoil jet axis falling within the FTPC η acceptance is very small (on the order of 0.0005% for $p_{\rm T}^{\rm jet} = 10$ GeV/c, and smaller for jets with higher $p_{\rm T}$), although the simulation does not indicate whether jet fragments can impinge on the FTPC, particularly if the jet is broadened by interactions with the QGP. Results from the jet v_2 analysis itself indicate that the jet – event plane bias in the FTPC is small or zero, as discussed in Section 5.6. It is kinematically impossible for the recoil jet to hit the ZDC-SMDs.

In the TPC and FTPCs, where the azimuthal angle of each track is known, Eq. 5.5 can be used as-is to reconstruct the event plane. In the ZDC-SMDs, which are hit-based detectors and do not have angular segmentation, the formula for determining the event plane is slightly different, as discussed in Section 5.3.3

5.3.1 TPC

The event plane is reconstructed at mid-rapidity in the TPC using the standard method shown in Eq. 5.5. The weights, w_i are chosen to equal the $p_{\rm T}$ of particle i since v_2 increases with $p_{\rm T}$ (in the $p_{\rm T}$ range for the tracks utilized in the event plane reconstruction). The quality cuts for the tracks used in the event plane are shown in Table 5.1. Note that only tracks with $0.2 < p_{\rm T} < 2$ GeV/c are used, as is typically

done in order to reduce the influence of jets in the event plane determination.

The angular distribution of event planes over many events should be isotropic. However, even small detector inefficiencies can cause the distribution of event planes calculated with Eq. 5.5 to be non-flat, and it is necessary to flatten the event plane distribution to avoid introducing correlations due to detector effects. In the TPC, which does not have large non-uniformities in the azimuthal angular acceptance for charged tracks, only ϕ-weighting is needed to flatten the event plane distribution. The acceptance of the TPC is determined by constructing a histogram of the $\eta - \phi$ distribution of charged tracks in a large sample of events. The contribution of each particle to the summations in Eq. 5.5 is inversely weighted by the content of the acceptance histogram at the particle's (η, ϕ) coordinate. (Clearly, this procedure must be performed separately for positively- and negatively-charged particles, and for each magnetic field configuration.) Figure 5.2 shows that ϕ-weighting is sufficient to produce a flat event plane distribution in the TPC.

5.3.2 FTPC

The event plane is reconstructed at forward rapidities in the FTPCs, using tracks in the pseudorapidity range $2.8 < |\eta| < 3.7$. As in the TPC, the FTPC event planes are also calculated with p_{T}-weighting, and the track quality cuts are shown in Table 5.1.

	TPC	FTPC
Pseudorapidity	$\|\eta\| < 1.0$	$2.8 < \|\eta\| < 3.7$
p_{T}	0.2 – 2.0 GeV/c	0.2 – 2.0 GeV/c
Distance of closest approach (DCA)	< 1.0 cm	< 2.0 cm
Number of fitted hits	≥ 20	5 – 11
Fitted/possible hits	≥ 0.55	0.52 – 1.02
Charge	± 1	± 1

Table 5.1: A comparison of the track cuts for determining the event planes in the TPC and FTPC.

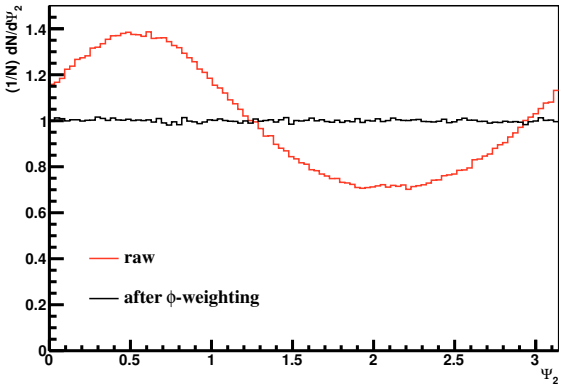

Figure 5.2: The distribution of event planes reconstructed in the TPC is shown with (black) and without (red) ϕ-weighting.

It is not possible to use ϕ-weighting to flatten the FTPC event plane distribution because the track acceptance in the FTPCs, shown in Fig. 5.3, is extremely non-uniform. Instead, recentering and shifting techniques are used to obtain a flat event plane distribution. The procedure for determining the FTPC event plane is as follows:

1. In each event, Eq. 5.5 is applied in the east and west FTPCs independently to obtain the east and west "sub-event" planes.

2. The distributions of the sub-event planes are made more uniform by recentering.

   In the recentering procedure, the average **Q**-vector is calculated over many events, and then subtracted from each individual **Q**-vector when calculating the event plane. This ensures that any **Q**-vector that is due to detector acceptance effects is removed.

3. The sub-event plane distributions are flattened by shifting.

   If the event plane distribution is still non-flat after recentering, the shifting procedure explicitly forces it to be flat. The distribution of raw event planes (Ψ_n) is decomposed into harmonics, and then an angular shift ($\Delta\Psi_n$) is calcu-

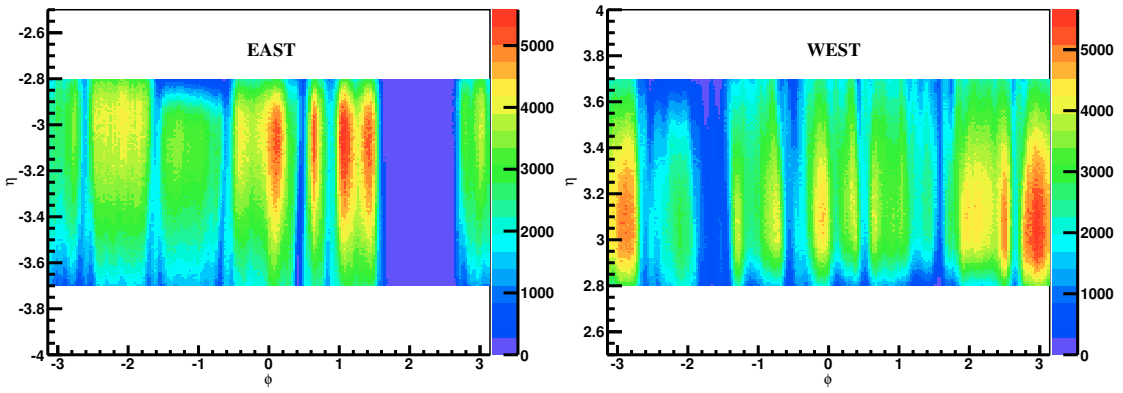

Figure 5.3: Track η–ϕ distributions in the east (left) and west (right) FTPCs.

lated for the event plane in each event such that the final distribution of shifted event planes $(\Psi_n + \Delta\Psi_n)$ is flat. The formula for calculating the shift is:

$$\Delta\Psi_n = \frac{1}{n}\sum_{i=1}^{i_{\max}} \frac{2}{i}\left[\langle\cos(in\Psi_n)\rangle \sin(in\Psi_n) - \langle\sin(in\Psi_n)\rangle \cos(in\Psi_n)\right] \tag{5.7}$$

For $n = 2$, $i_{\max} = 3$.

4. In each event, the full FTPC event plane is the weighted average of the shifted sub-event planes:

$$\Psi_{2,\text{full}} = \frac{1}{2}\tan^{-1}\left(\frac{|Q_{2,\text{west}}|\sin(2\Psi_{2,\text{west}}) + |Q_{2,\text{east}}|\sin(2\Psi_{2,\text{east}})}{|Q_{2,\text{west}}|\cos(2\Psi_{2,\text{west}}) + |Q_{2,\text{east}}|\cos(2\Psi_{2,\text{east}})}\right) \tag{5.8}$$

5. The distribution of full event planes is flattened by shifting.

Recentering and shifting are done on a run-by-run basis. Figure 5.4 shows the distribution of the event planes after each step in the procedure described above.

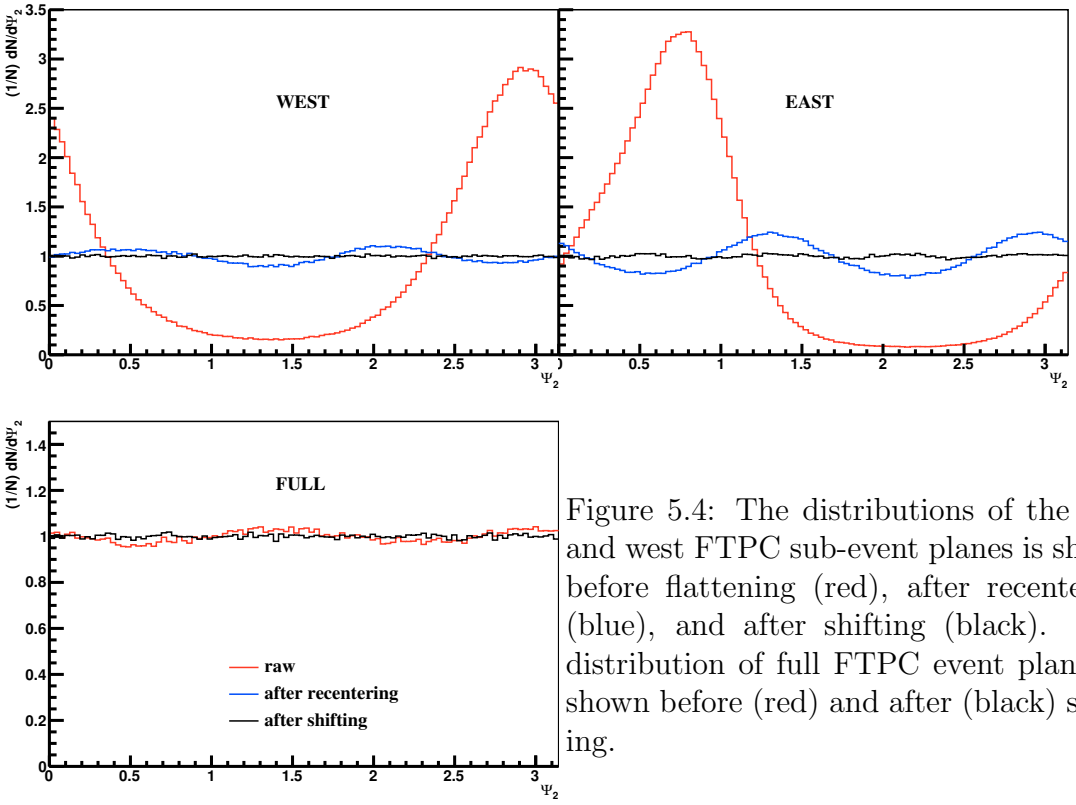

Figure 5.4: The distributions of the east and west FTPC sub-event planes is shown before flattening (red), after recentering (blue), and after shifting (black). The distribution of full FTPC event planes is shown before (red) and after (black) shifting.

5.3.3 ZDC-SMD

The event plane is reconstructed at far forward rapidities using the energy deposition of spectator neutrons in the ZDC-SMDs. Unlike the TPC and FTPCs, which are track-based detectors, the ZDC-SMDs are hit-based detectors. Since v_2 decreases with increasing pseudorapidity, the ZDC-SMDs are only sensitive to directed flow (v_1). The first-harmonic event plane is calculated using the energy deposition in each of 7 vertical slats and 8 horizontal slats, as shown in Eq. 5.9.

$$\Psi_{\mathrm{EP}}\{\text{ZDC-SMD}\} = \tan^{-1}\left(\frac{\sum_{i=1}^{8} w_i(y_i - y_0)}{\sum_{i=1}^{7} w_i(x_i - x_0)}\right) \tag{5.9}$$

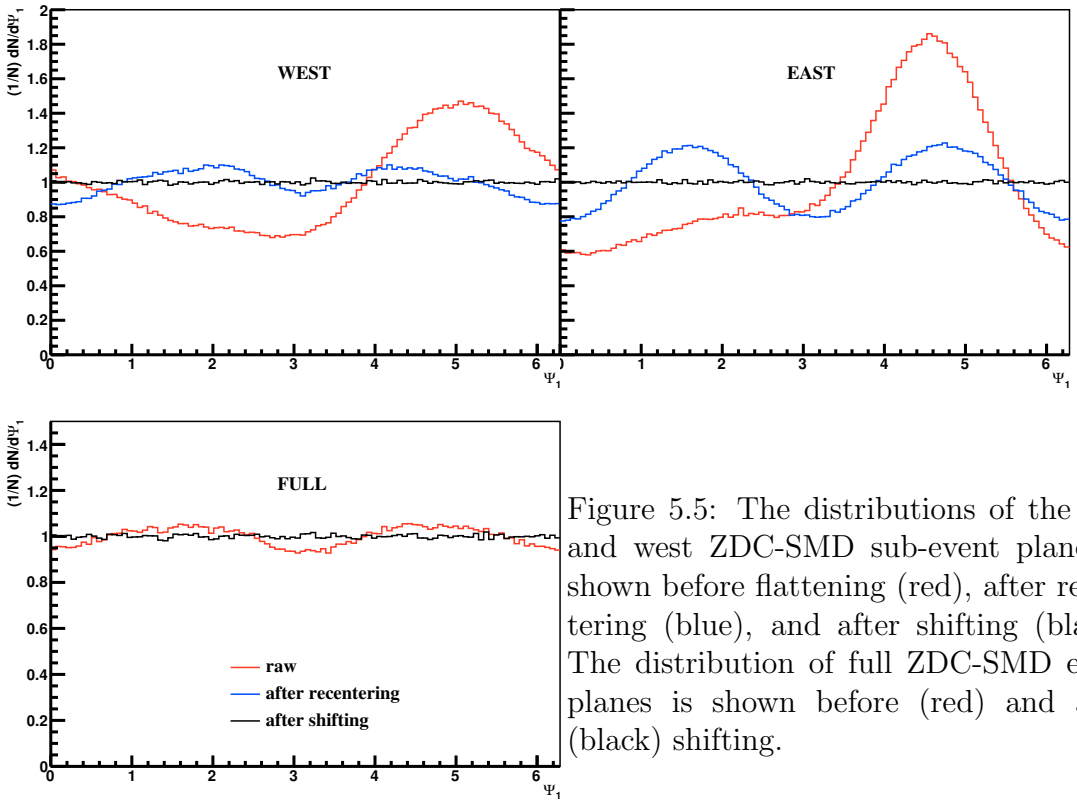

Figure 5.5: The distributions of the east and west ZDC-SMD sub-event planes is shown before flattening (red), after recentering (blue), and after shifting (black). The distribution of full ZDC-SMD event planes is shown before (red) and after (black) shifting.

The positions of the slats are denoted by x_i and y_i for the vertical and horizontal slats, respectively. They are adjusted for the $p_{\mathrm{T}} = 0$ point, denoted by (x_0, y_0), which is calculated on a day-by-day basis. The weights are given by the energy deposited in the slats. The energy is obtained from the ADC value, with the pedestal subtracted and multiplied by the slat's gain, as shown in Eq. 5.10.

$$w_i = \frac{g_i * (\mathrm{ADC}_i - \mathrm{ped}_i)}{\left(\sum_{j=1}^{7 \text{ or } 8} g_j * (\mathrm{ADC}_j - \mathrm{ped}_j) \right)} \tag{5.10}$$

The same procedure for calculating the full event plane is used for the ZDC-SMDs as for the FTPCs, above. In the shifting procedure, $i_{\max} = 4$ for $n = 1$. Recentering and shifting are done on a day-by-day basis. Figure 5.5 shows the distribution of the event planes after each step in the procedure.

5.4 Event Plane Resolution

The event plane resolution, $\mathscr{R}$, in each of the detectors is calculated with the η-subevent method [77]. The event planes in the negative and positive η regions are calculated separately, and the difference between the two planes is used to determine the accuracy with which the event plane can be calculated. First the correlation between the two planes is used to obtain the sub-event plane resolution:

$$\mathscr{R}_{n,\mathrm{sub}} = \sqrt{\langle \cos\left[n(\Psi_n^{\eta<0} - \Psi_n^{\eta>0})\right]\rangle} \tag{5.11}$$

Then the resolution parameter (χ) can be obtained by solving Eq. 5.12 numerically.

$$\mathscr{R}_k(\chi) = \frac{\sqrt{\pi}}{2}\chi e^{-\chi^2/2}\left(I_{(k-1)/2}(\chi^2/2) + I_{(k+1)/2}(\chi^2/2)\right) \tag{5.12}$$

Since the resolution parameter is proportional to the square root of the multiplicity, the full event plane resolution can be calculated by evaluating Eq. 5.13, using χ from the sub-events.

$$\mathscr{R}_{\mathrm{full}} = \mathscr{R}\left(\sqrt{2}\chi_{\mathrm{sub}}\right) \tag{5.13}$$

The event plane resolution is shown in Fig. 5.6. In the 0-50% centrality range, the resolution of the event plane in the TPC ranges from 0.55 to 0.8 and the resolution of the FTPC event plane is between 0.09 and 0.3. The resolutions of the first- and second-harmonic flow with respect to the first-harmonic event plane in the ZDC-SMD (denoted by $R_{11}\{\text{ZDC-SMD}\}$ and $R_{12}\{\text{ZDC-SMD}\}$, respectively) are also shown in Fig. 5.6. The resolution of the second-order flow with respect to the first-order event plane in the ZDC-SMD is less than 0.1. For small values of the resolution, the approximation can be made that $R_{12} \approx (2/\pi)R_{11}^2$. In Fig. 5.6 it can be seen that this approximation matches the directly-measured values of $R_{12}\{\text{ZDC-SMD}\}$

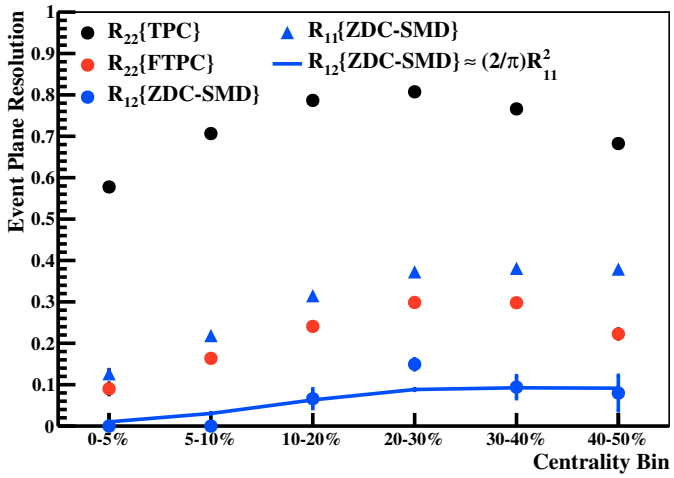

Figure 5.6: The event plane resolutions for the TPC, FTPCs, and ZDC-SMDs.

for all centralities except the 20-30% bin, where it differs significantly. Consistency checks and comparisons to other STAR analyses indicate that the value of $(2/\pi)R_{11}^2$ is more correct in that centrality bin, and the measured value of $R_{12}\{\text{ZDC-SMD}\}$ is attributed to a fluctuation. In the following analysis, the values of $(2/\pi)R_{11}^2$ will be used as the resolution $R_{12}\{\text{ZDC-SMD}\}$. Additionally, since $R_{12}\{\text{ZDC-SMD}\}$ is unsurprisingly measured to be essentially zero in the 0-5% and 5-10% centrality bins, measurements of $v_2^{\text{jet}}\{\text{ZDC-SMD}\}$ will not be reported in that centrality range.

5.5 Jet Energy Scale and Background Fluctuations

Although the constituent p_{T} cut reduces the effects of background fluctuations on the jet energy scale, it is still necessary to assess the effects of non-jet particles being clustered into the jet on the measurement of jet v_2. Background particles (with $p_{\text{T}} > 2$ GeV/c) have significant v_2 [63] and are therefore more likely to be clustered into the jet cone in-plane versus out-of-plane, since the v_2 modulation of the background is not accounted for in the jet reconstruction. Consequently, more

low-p_{T} jets get reconstructed at higher p_{T}, artificially increasing the number of in-plane jets in a fixed reconstructed jet p_{T} range. In this way, background fluctuations produce an artificial jet v_2 signal.

The magnitude of this artificial jet v_2 is determined by embedding p+p HT jets in Au+Au MB events. In this embedding, it is possible to determine three relevant quantities: the reconstructed jet p_{T} in p+p ($p_{\mathrm{T}}^{\mathrm{jet},p+p}$), the reconstructed jet p_{T} with Au+Au background fluctuations ($p_{\mathrm{T}}^{\mathrm{jet,emb}}$), and the event plane of the Au+Au event (determined before embedding the jet). The jets are embedded isotropically with respect to the event plane of the underlying event, and therefore v_2^{jet} is zero when calculated in a given range of $p_{\mathrm{T}}^{\mathrm{jet},p+p}$. However, when jet v_2 is calculated in a range of $p_{\mathrm{T}}^{\mathrm{jet,emb}}$, background fluctuations produce a measured artificial jet v_2 of approximately 4% (with little dependence on centrality and $p_{\mathrm{T}}^{\mathrm{jet}}$), as shown in Fig. 5.7. In this analysis, the effect of background fluctuations is subtracted from the measured v_2 values directly, and no attempt is made to correct the reconstructed jet energy via an average background subtraction or any other method.

5.6 Results

Jet v_2 has been investigated differentially with respect to centrality and reconstructed jet p_{T}, and compared to the v_2 of HT trigger towers (v_2^{HT}, with $E_{\mathrm{T}}^{\mathrm{HT}} > 5.5$ GeV).

5.6.1 Centrality

Figure 5.8 shows measurements of jet v_2 and HT v_2 in six centrality bins, for $10 < p_{\mathrm{T}}^{\mathrm{jet,rec}} < 40$ GeV/c. The artificial jet – event plane bias is clearly seen in the increase of $v_2^{\mathrm{jet}}\{\mathrm{TPC}\}$ over $v_2^{\mathrm{jet}}\{\mathrm{FTPC}\}$, and introduces up to a 25% v_2 signal in the most peripheral bin (40-50%). The magnitude of the difference between $v_2^{\mathrm{jet}}\{\mathrm{TPC}\}$ and

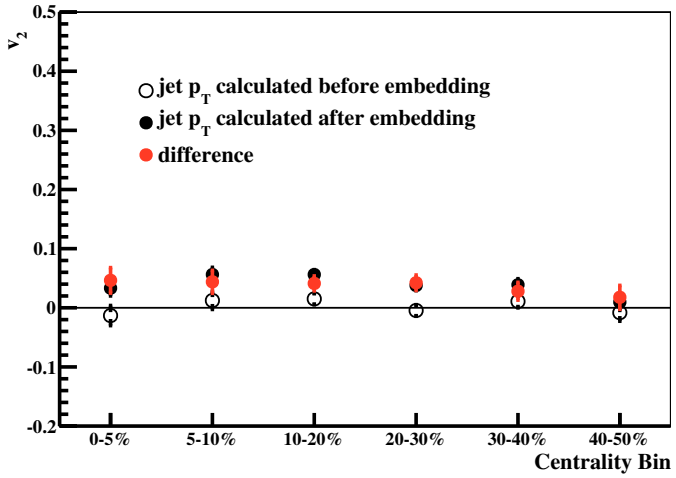

Figure 5.7: The v_2 of p+p HT jets embedded isotropically into Au+Au MB events is shown when the jet p_{T} is calculated before (open black symbols) and after (closed black symbols) embedding. The difference between the measured v_2 values (red symbols) is the artificial jet v_2 induced by background fluctuations. The results here are shown as a function of centrality for jets in the $10 < p_{\mathrm{T}}^{\mathrm{jet}} < 40$ GeV/c range.

$v_2^{\mathrm{jet}}\{\mathrm{FTPC}\}$ is due to the TPC event plane reconstruction being biased by fragments from all of the reconstructed jets and a majority of the recoil jets while the FTPC event plane reconstruction can only be biased by a small fraction of the recoil jet fragments. Thus it is expected that the jet – event plane bias in the FTPC is small and has a negligible effect on the measured $v_2^{\mathrm{jet}}\{\mathrm{FTPC}\}$. It is also observed that $v_2^{\mathrm{jet}}\{\mathrm{TPC}\}$ is significantly higher than $v_2^{\mathrm{HT}}\{\mathrm{TPC}\}$, indicating that the jet – event plane bias is stronger when jets contain additional high-p_{T} fragments (even though those fragments with $p_{\mathrm{T}} > 2$ GeV/c are not included in the event plane calculation).

A comparison of v_2^{jet} and v_2^{HT} can give insights into the biases involved in the jet definition described in Section 5.2. It is observed that $v_2^{\mathrm{jet}}\{\mathrm{FTPC}\}$ is consistent with $v_2^{\mathrm{HT}}\{\mathrm{FTPC}\}$, indicating that the surface bias or bias towards unmodified jets, which is the physical mechanism for jet v_2, is largely driven by the HT trigger requirement, and only to a lesser extent by the 2 GeV/c constituent p_{T} cut. At this stage, due to limited statistics, no conclusions can be drawn about $v_2^{\mathrm{jet}}\{\mathrm{ZDC\text{-}SMD}\}$, although

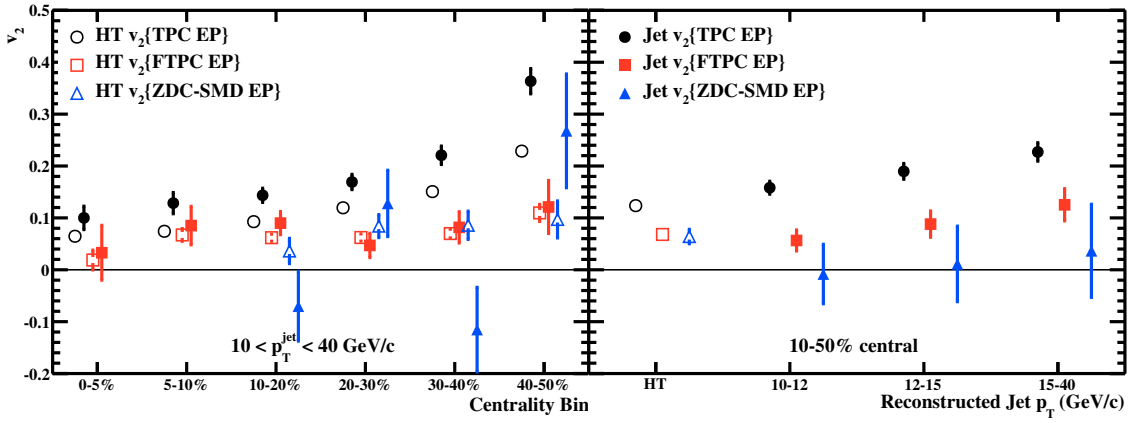

Figure 5.8: Jet v_2 (closed symbols) and HT trigger v_2 (open symbols) are shown when the event plane is determined by three sets of detectors: the TPC (black circles), the FTPC (red squares), and the ZDC-SMD (blue triangles). The results are shown as a function of centrality (left) and reconstructed jet p_{T} (right).

$v_2^{\mathrm{HT}}\{\text{ZDC-SMD}\}$ is observed to be non-zero. The finite values of $v_2^{\mathrm{jet}}\{\text{FTPC}\}$ and $v_2^{\mathrm{HT}}\{\text{ZDC-SMD}\}$ are evidence of the pathlength-dependence of parton energy loss.

At this point, no centrality dependence is observed within the statistical precision of this measurement. Interpretation of this result is further convoluted by the fact that the reconstructed jet energy is dependent on centrality, because more background particles are clustered into the jet cone in central events than in peripheral events. Future studies on the correspondence between the reconstructed jet p_{T} and the original parton energy may clarify the centrality dependence.

5.6.2 Jet p_{T}

Figure 5.8 shows a slight increase in $v_2^{\mathrm{jet}}\{\text{FTPC}\}$ with reconstructed jet p_{T}. This trend may be contrary to initial expectations, because at some high $p_{\mathrm{T}}^{\mathrm{jet}}$ value jets would escape the interaction region before the medium even has time to form, and so jet-medium interactions and jet v_2 are expected to go to zero. Apparently that kinematic regime has not been reached in the jet p_{T} range explored in this analysis

(as also demonstrated by the jet-hadron analysis). A qualitative explanation for the increasing trend with $p_{\mathrm{T}}^{\mathrm{jet,rec}}$ is that jets reconstructed with higher momenta have more high-p_{T} fragments, meaning that they undergo less interaction with the medium, which results in a higher v_2^{jet}.

Furthermore, it is observed that $v_2^{\mathrm{jet}}\{\mathrm{FTPC}\}$ is typically larger than $v_2^{\mathrm{jet}}\{\mathrm{ZDC\text{-}SMD}\}$. It is suggested [81] that asymmetries in the distribution of spectator neutrons detected at forward pseudorapidities are more sensitive to the reaction plane geometry, so the event plane reconstructed in the ZDC-SMDs is more closely related to the reaction plane. Meanwhile the asymmetries of produced particles at midrapidity are more sensitive to the participant geometry and therefore the event planes from the TPC and FTPCs are closer to the 2^{nd}-harmonic participant plane. Single-particle measurements also demonstrate $v_2\{\mathrm{FTPC}\} > v_2\{\mathrm{ZDC\text{-}SMD}\}$, which is often attributed to flow in the participant plane frame being larger than flow in the reaction plane frame [82]. This similar conclusion for v_2^{jet} could therefore indicate that jet quenching, like collective flow, is more sensitive to the participant plane geometry than the reaction plane geometry.

Chapter 6

Jet v_n method*

While measurements of jet v_2 and jet v_n can provide information about the pathlength-dependence of parton energy loss, they are challenging due to the significant jet – event plane bias. Utilizing forward detectors to reconstruct the event plane is possible, but the resulting measurements suffer large uncertainties due to low event plane resolution, as shown in Chapter 5. The ability to measure jet v_2 using only detectors at mid-rapidity would allow for stronger conclusions to be drawn. This chapter presents a method for calculating jet v_2 and the 2^{nd}-order event plane by accounting for the presence of a high-p_{T} jet, instead of attempting to remove the jet particles from the event plane reconstruction. The method is then extended to calculate v_n^{jet} and $\Psi_{\text{EP},n}$.

6.1 The Standard Event Plane Calculation

The standard method of calculating the event plane is by defining the vector $\mathbf{Q}_2$ that describes the bulk particle distribution, as discussed in Section 5.1. Events containing jets, however, can be decomposed into two vectors: one describing the

*Published in Phys. Rev. C87, 034909 (2013). Copyright 2013 by the American Physical Society.

bulk distribution ($\mathbf{Q}_2$) and one describing the jet constituents ($\mathbf{A}_2$). When a jet is present, the standard event plane method does not find the angle of $\mathbf{Q}_2$ but rather the angle of the sum of these two vectors ($\mathbf{G}_2 = \mathbf{Q}_2 + \mathbf{A}_2$), as shown in (6.1):

$$\begin{aligned} G_{2,x,\text{lab}} &= \sum_i w_i \cos(2\phi_i) \\ &= \sum_{i\in\text{bulk}} w_i \cos(2\phi_i) + \sum_{i\in\text{jet}} w_i \cos(2\phi_i) \\ &= Q_2 \cos(2\Psi_{\text{EP},2}) + A_2 \cos(2\Psi_{\text{jet}}) \\ G_{2,y,\text{lab}} &= \sum_i w_i \sin(2\phi_i) \\ &= \sum_{i\in\text{bulk}} w_i \sin(2\phi_i) + \sum_{i\in\text{jet}} w_i \sin(2\phi_i) \\ &= Q_2 \sin(2\Psi_{\text{EP},2}) + A_2 \sin(2\Psi_{\text{jet}}) \end{aligned} \tag{6.1}$$

The difficulty is to untangle $\mathbf{A}_2$ and $\mathbf{Q}_2$ in order to extract the angle of $\mathbf{Q}_2$ alone. Assuming that jets can be accurately reconstructed in heavy-ion collisions, there is another piece of information that is known: the angle of $\mathbf{A}_2$, which is the jet axis.

6.2 A New Event Plane Method

If $G_{2,x}$ and $G_{2,y}$ are calculated with respect to the jet axis (instead of in the laboratory frame, as shown in (6.1)), then A_2 only appears in one of the terms:

$$\begin{aligned} G_{2,x,\text{jet}} &= \sum_i w_i \cos(2(\phi_i - \Psi_{\text{jet}})) \\ &= Q_2 \cos(2(\Psi_{\text{EP},2} - \Psi_{\text{jet}})) + A_2 \\ G_{2,y,\text{jet}} &= \sum_i w_i \sin(2(\phi_i - \Psi_{\text{jet}})) \\ &= Q_2 \sin(2(\Psi_{\text{EP},2} - \Psi_{\text{jet}})) \end{aligned} \tag{6.2}$$

Taking the averages of $G_{2,x,\text{jet}}$ and $G_{2,y,\text{jet}}$ over many events yields:

$$\begin{aligned} \langle G_{2,x,\text{jet}} \rangle &= \langle Q_2 \cos(2(\Psi_{\text{EP},2} - \Psi_{\text{PP},2})) \rangle v_2^{\text{jet}} + \langle A_2 \rangle \\ \langle G_{2,y,\text{jet}} \rangle &= 0 \end{aligned} \tag{6.3}$$

In (6.3) v_2^{jet} has replaced the quantity $\langle \cos(2(\Psi_{\text{jet}} - \Psi_{\text{PP},2})) \rangle$. It is assumed in this decomposition that v_2^{jet} is independent of Q_2.

Solving for v_2^{jet} and $\Psi_{\text{EP},2}$ requires calculating the higher moments of $\mathbf{G}_2$ listed in (6.4). Note that terms from higher mixed harmonics (on the order of v_4^{jet} and above) are neglected in (6.4):

$$\begin{aligned} \langle G_{2,y,\text{jet}}^2 \rangle &= \tfrac{1}{2} \langle Q_2^2 \rangle \\ \langle G_{2,x,\text{jet}} G_{2,y,\text{jet}}^2 \rangle &= \tfrac{1}{4} \left(\langle Q_2^3 \cos(2(\Psi_{\text{EP},2} - \Psi_{\text{PP},2})) \rangle v_2^{\text{jet}} + 2 \langle A_2 \rangle \langle Q_2^2 \rangle \right) \\ \langle G_{2,y,\text{jet}}^4 \rangle &= \tfrac{3}{8} \langle Q_2^4 \rangle \end{aligned} \tag{6.4}$$

In (6.3) the quantity $Q_2 \cos(2(\Psi_{\text{EP},2} - \Psi_{\text{PP},2}))$ is $Q_{2,x}$ in the participant plane

frame. It is necessary to assume functional forms for the distributions of $Q_{2,x,\mathrm{PP}}$ and $Q_{2,y,\mathrm{PP}}$ in order to solve the equations in (6.3) and (6.4). The distributions of $Q_{2,x,\mathrm{PP}}$ and $Q_{2,y,\mathrm{PP}}$ are taken to be Gaussian with standard deviation σ. The distribution of $Q_{2,x,\mathrm{PP}}$ is centered at μ while the distribution of $Q_{2,y,\mathrm{PP}}$ is centered at zero. The relevant moments of $\mathbf{Q}_2$ are

$$\begin{aligned} \langle Q_{2,x,\mathrm{PP}} \rangle &= \mu \\ \langle Q_2^2 \rangle &= \langle Q_{2,x,\mathrm{PP}}^2 + Q_{2,y,\mathrm{PP}}^2 \rangle = \mu^2 + 2\sigma^2 \\ \langle Q_{2,x,\mathrm{PP}} Q_2^2 \rangle &= \langle Q_{2,x,\mathrm{PP}}^3 + Q_{2,x,\mathrm{PP}} Q_{2,y,\mathrm{PP}}^2 \rangle = \mu^3 + 4\mu\sigma^2 \\ \langle Q_2^4 \rangle &= \langle (Q_{2,x,\mathrm{PP}}^2 + Q_{2,y,\mathrm{PP}}^2)^2 \rangle = \mu^4 + 8\mu^2\sigma^2 + 8\sigma^4 \end{aligned} \tag{6.5}$$

The system of equations in (6.3)–(6.5) can be solved to yield the parameters μ and σ:

$$\begin{aligned} \mu^2 &= \sqrt{8\langle G_{2,y,\mathrm{jet}}^2 \rangle^2 - \tfrac{8}{3}\langle G_{2,y,\mathrm{jet}}^4 \rangle} \\ \sigma^2 &= \langle G_{2,y,\mathrm{jet}}^2 \rangle - \tfrac{1}{2}\mu^2 \end{aligned} \tag{6.6}$$

It is straightforward to solve for jet v_2 using Eqs. (6.3)–(6.6).

6.2.1 Jet v_2

The formula for v_2^{jet} in this new method (denoted by $v_2^{\mathrm{jet}}\{\mathrm{QA}\}$) is given in Eq. (6.7):

$$v_2^{\mathrm{jet}}\{\mathrm{QA}\} = \frac{4\langle G_{2,x,\mathrm{jet}} \rangle \langle G_{2,y,\mathrm{jet}}^2 \rangle - 4\langle G_{2,x,\mathrm{jet}} G_{2,y,\mathrm{jet}}^2 \rangle}{\mu^3} \tag{6.7}$$

Note that this method already accounts for the event plane resolution by calculating $\langle \cos(2(\Psi_{\mathrm{jet}} - \Psi_{\mathrm{PP},2})) \rangle$ instead of $\langle \cos(2(\Psi_{\mathrm{jet}} - \Psi_{\mathrm{EP},2})) \rangle$. It is not necessary to divide the resulting $v_2^{\mathrm{jet}}\{\mathrm{QA}\}$ by the event plane resolution.

6.2.2 Event Plane

Additionally, Eqs. (6.3)–(6.6) can be solved for $\langle A_2 \rangle$, the average shift in $G_{2,x,\mathrm{jet}}$ due to the jet.

$$\langle A_2 \rangle = \langle G_{2,x,\mathrm{jet}} \rangle - \mu v_2^{\mathrm{jet}} \tag{6.8}$$

Once $\langle A_2 \rangle$ is known, it can be subtracted from $G_{2,x,\mathrm{jet}}$ event by event. Then the event plane can be calculated in a way that is, on average, not biased towards the jet, using Eq. (6.9) which is based on Eq. (5.5):

$$\Psi_{\mathrm{EP},2} = \frac{1}{2} \tan^{-1} \left(\frac{\sum_i w_i \sin\left(2(\phi_i - \Psi_{\mathrm{jet}})\right)}{\sum_i w_i \cos\left(2(\phi_i - \Psi_{\mathrm{jet}})\right) - \langle A_2 \rangle} \right) + \Psi_{\mathrm{jet}} \tag{6.9}$$

6.3 Higher Harmonics v_n^{jet}

The quantities $G_{n,x,\mathrm{jet}}$ and $G_{n,y,\mathrm{jet}}$ can be evaluated at any order n:

$$\begin{aligned} G_{n,x,\mathrm{jet}} &= \sum_i w_i \cos(n(\phi_i - \Psi_{\mathrm{jet}})) \\ &= Q_n \cos(n(\Psi_{\mathrm{EP},n} - \Psi_{\mathrm{jet}})) + A_n \\ G_{n,y,\mathrm{jet}} &= \sum_i w_i \sin(n(\phi_i - \Psi_{\mathrm{jet}})) \\ &= Q_n \sin(n(\Psi_{\mathrm{EP},n} - \Psi_{\mathrm{jet}})) \end{aligned} \tag{6.10}$$

However, beyond the definitions of $G_{n,x,\mathrm{jet}}$ and $G_{n,y,\mathrm{jet}}$, the method described above does not depend on the value of n. Therefore the equations listed in (6.3)–(6.7) can be used to solve for any v_n^{jet}. Solving for the n^{th}-order event plane utilizes Eqs. (6.8) and (6.11), and is analogous to Eq. (6.9):

$$\Psi_{\mathrm{EP},n} = \frac{1}{n} \tan^{-1} \left(\frac{\sum_i w_i \sin\left(n(\phi_i - \Psi_{\mathrm{jet}})\right)}{\sum_i w_i \cos\left(n(\phi_i - \Psi_{\mathrm{jet}})\right) - \langle A_n \rangle} \right) + \Psi_{\mathrm{jet}} \tag{6.11}$$

6.4 Simulation

This method has been tested on simple simulated events, each of which consists of a PYTHIA [78, 79] (p+p-like) jet embedded in a thermal background. PYTHIA jets are simulated in an interval of ± 2 GeV around a given transverse energy $E_{\mathrm{T}}^{\mathrm{jet}}$. The charged tracks in the PYTHIA event are analyzed with the anti-k_{T} algorithm from the FastJet package [37] (with a resolution parameter $R = 0.4$) to obtain the charged jet p_{T} ($p_{\mathrm{T}}^{\mathrm{jet,ch}}$) and the angles of the jet axis (Ψ_{jet},η_{jet}). The charged jet p_{T} from FastJet is required to satisfy $\frac{2}{3c}\left(E_{\mathrm{T}}^{\mathrm{jet}} - 2\ \mathrm{GeV}\right) < p_{\mathrm{T}}^{\mathrm{jet,ch}} < \frac{2}{3c}\left(E_{\mathrm{T}}^{\mathrm{jet}} + 2\ \mathrm{GeV}\right)$; this requirement ensures that at least one of the jets from PYTHIA is inside the detector acceptance. Only tracks at midrapidity ($|\eta| < 1$) are used in the simulation to mimic the acceptance of the STAR and ALICE TPCs [42, 83], and the jet axis is restricted to lie within $|\eta_{\mathrm{jet}}| < 1 - R$. Note that the jet axis and p_{T} are reconstructed prior to embedding the jet in the thermal background, to avoid issues related to full jet reconstruction in a heavy-ion environment, although such a separation is not possible in experimental data. The thermal ($T = 0.291$ GeV, which corresponds to approximately $\sqrt{s_{\mathrm{NN}}} = 200$ GeV) background event is created such that the 2$^{\mathrm{nd}}$-order participant plane is correlated with Ψ_{jet} according to Eq. (5.1) in order to produce a jet v_2. The p_{T}- and centrality-dependent v_2 values of the background particles and the multiplicities of the background event are chosen to be consistent with observations from STAR [63, 80] at RHIC.

6.4.1 Jet v_2

Jet v_2 is calculated from all charged tracks in the combined event, without p_{T}-weighting. The results are similar when p_{T}-weighting or a track p_{T} cut is used. For each bin in N_{ch}, the number of charged particles at mid-rapidity in the event, jet v_2

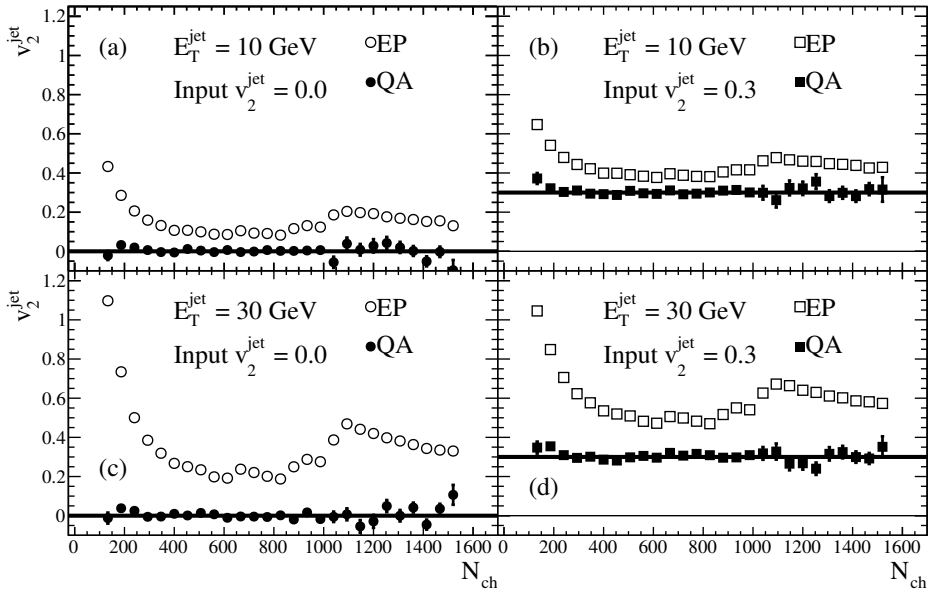

Figure 6.1: Jet v_2 is calculated using the standard (EP) method (open symbols) and the new (QA) method (closed symbols) in simulated events consisting of a PYTHIA jet embedded in a thermal background ($T = 0.291$ GeV). The simulated jet v_2 is denoted by a solid line for two cases: $v_2^{\rm jet} = 0.0$ (left column) and $v_2^{\rm jet} = 0.3$ (right column). The results are shown for two jet energies: $E_{\rm T}^{\rm jet} = 10$ GeV (top row) and $E_{\rm T}^{\rm jet} = 30$ GeV (bottom row). The $p_{\rm T}$- and centrality-dependent v_2 values and multiplicities of the background are consistent with observations from STAR [63, 80]. Statistical errors are drawn but are often smaller than the symbol size. The "jumps" in the distribution of $v_2^{\rm jet}\{{\rm EP}\}$ correspond to the edges of the centrality bins in [63] that were used to simulate the bulk v_2.

is calculated using the standard method (Eqs. (5.5)–(5.6)) and with the new method proposed here (Eq. (6.7)). The results of the simulation are shown in Fig. 6.1 for $v_2^{\rm jet} = 0.0$ and $v_2^{\rm jet} = 0.3$ in two cases: $E_{\rm T}^{\rm jet} = 10$ GeV and $E_{\rm T}^{\rm jet} = 30$ GeV.

The results of the simulation indicate that the standard method of calculating $v_2^{\rm jet}\{{\rm EP}\}$ leads to an overestimation of the true jet v_2 by 5–20% (or more, in peripheral collisions) due to the jet biasing the event plane calculation. However, the new method of calculating $v_2^{\rm jet}\{{\rm QA}\}$ obtains accurate values of jet v_2. The observed discrepancy between the simulated $v_2^{\rm jet}$ and $v_2^{\rm jet}\{{\rm EP}\}$ is largest in the most central events where the bulk v_2 is low and the event plane is not well defined, and in the

most peripheral events where the ratio of jet fragments to bulk particles is significant. The artificial jet – event plane bias increases with jet energy.

6.4.2 Event Plane

The event plane was calculated using the standard method (Eq. (5.5)) and the new method (Eq. (6.9)) and then compared with the simulated participant plane in Fig. 6.2. Both methods accurately reconstruct the participant plane, and the results are shown separately for the cases in which the jet is in-plane ($|\Psi_{\rm jet} - \Psi_{\rm PP,2}| < \pi/6$) and out-of-plane ($|\Psi_{\rm jet} - \Psi_{\rm PP,2}| > \pi/3$). It is clear from Fig. 6.2 that the standard event plane resolution depends on the orientation of the jet with respect to the participant plane. When the jet is aligned with the participant plane, the resolution of the standard event plane method is high because the jet pulls the event plane towards the participant plane. When the jet is perpendicular to the participant plane, the standard event plane is pulled away from the true participant plane, thus lowering the resolution. However, the resolution of the event plane calculated with the new (QA) method does not depend on the orientation of the jet to the participant plane, as is desirable.

Table 6.1 shows the standard deviation (σ) of the event plane from the participant plane, for both the standard method and the new (QA) method, in two centrality bins and for three orientations of the jet to the participant plane. The results show that while the standard event plane resolution depends on the orientation of the jet, the QA event plane resolution is constant. Furthermore, the resolution of the QA event plane does not differ significantly from the resolution of the standard event plane in either of the centrality classes.

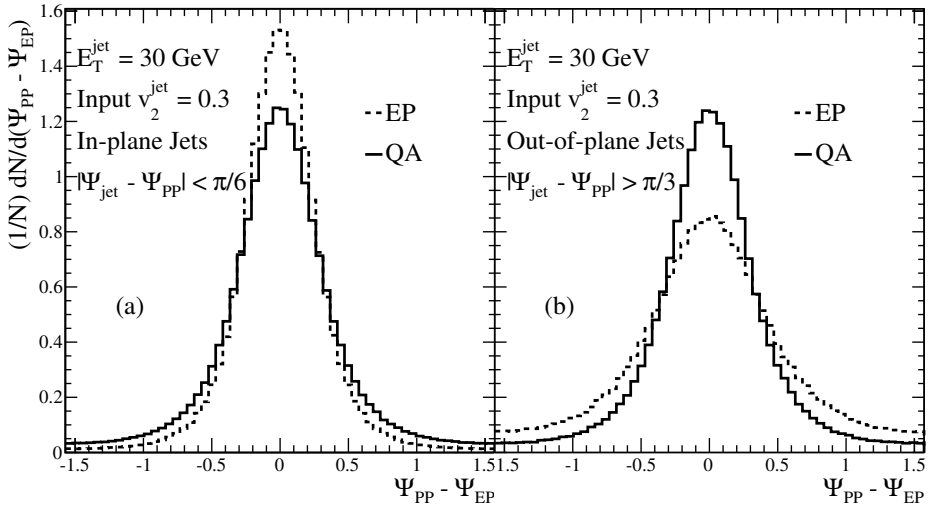

Figure 6.2: The event plane is calculated using the standard (EP) and new (QA) methods in simulated events consisting of a PYTHIA jet with $E_{\mathrm{T}}^{\mathrm{jet}} = 30$ GeV embedded in a thermal background ($T = 0.291$ GeV). The p_{T}- and centrality-dependent v_2 values and multiplicities of the background are consistent with observations from STAR [63, 80], and $v_2^{\mathrm{jet}} = 0.3$. The difference between the reconstructed event planes and the participant plane are folded into the interval $\left(-\frac{\pi}{2}, \frac{\pi}{2}\right)$ and are shown for two cases: (a) the jet is aligned with the participant plane and (b) the jet is perpendicular to the participant plane. The results are integrated over N_{ch}.

6.4.3 Jet v_3

The simulation was modified to include a background modulated by v_2 and v_3 and a jet correlated to $\Psi_{\mathrm{PP},2}$ and $\Psi_{\mathrm{PP},3}$ via v_2^{jet} and v_3^{jet}. The underlying event v_3 was chosen to equal the v_2 measured by STAR in the 5–10% centrality bin [63]. The 2^{nd}- and 3^{rd}-order participant planes are each correlated with the jet axis, but are not explicitly correlated to each other. Figure 6.3 shows the results of a simulation in which 30 GeV jets are chosen to have $v_2^{\mathrm{jet}} = 0.1$ and $v_3^{\mathrm{jet}} = 0.3$. The new jet v_n method can accurately measure the jet v_2 and v_3 harmonics independently. The standard method estimation of jet v_3 is less biased than the estimation of v_2^{jet}, because in the case of odd harmonics, the two jets in a dijet pair pull the event plane in opposite directions, and thus the bias is largely canceled.

Jet – Participant Plane Orientation	σ_{EP}	σ_{QA}
$0 < \lvert\Psi_{\mathrm{jet}} - \Psi_{\mathrm{PP},2}\rvert < \pi/6$	0.3419 ± 0.0004	0.4378 ± 0.0004
$\pi/6 < \lvert\Psi_{\mathrm{jet}} - \Psi_{\mathrm{PP},2}\rvert < \pi/3$	0.4461 ± 0.0004	0.4374 ± 0.0004
$\pi/3 < \lvert\Psi_{\mathrm{jet}} - \Psi_{\mathrm{PP},2}\rvert < \pi/2$	0.5755 ± 0.0006	0.4397 ± 0.0006
Centrality	σ_{EP}	σ_{QA}
Peripheral ($107 \leq N_{\mathrm{ch}} < 800$)	0.3426 ± 0.0004	0.3399 ± 0.0004
Central ($800 \leq N_{\mathrm{ch}} \leq 1546$)	0.4912 ± 0.0004	0.5157 ± 0.0003

Table 6.1: Standard deviation of the event plane from the participant plane, when the event plane is calculated with the standard method (σ_{EP}) and with the new method (σ_{QA}). The results are shown for two centrality bins, and three orientations of the jet to the participant plane. Errors are statistical only.

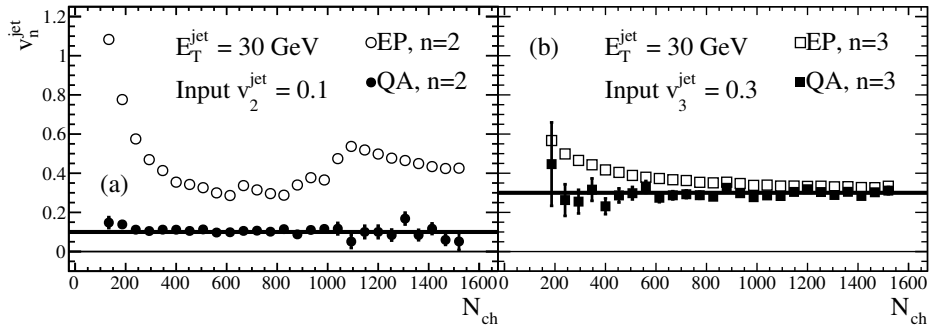

Figure 6.3: Jet v_2 and v_3 are calculated simultaneously using the standard (EP) method (open symbols) and the new (QA) method (closed symbols) in simulated events consisting of a PYTHIA jet with $E_{\mathrm{T}}^{\mathrm{jet}} = 30$ GeV embedded in a thermal background ($T = 0.291$ GeV). The p_{T}- and centrality-dependent v_2 values and multiplicities of the background are consistent with observations from STAR [63, 80]. Solid lines denote the simulated (a) jet $v_2 = 0.1$ and (b) jet $v_3 = 0.3$. Statistical errors are drawn.

6.4.4 Jets at the LHC

The simulation was also modified so that the v_2 values of the background particles and the multiplicities of the thermal ($T = 0.350$ GeV) background event are consistent with observations from ALICE [84, 85] at the LHC. The results are shown in Fig. 6.4 for $E_{\mathrm{T}}^{\mathrm{jet}} = 100$ GeV and $v_2^{\mathrm{jet}} = 0.3$. Due to the higher multiplicities at LHC energies, the standard event plane method does not overestimate jet v_2 as drastically as at RHIC energies. The new method also successfully recovers the correct jet v_2 at LHC energies.

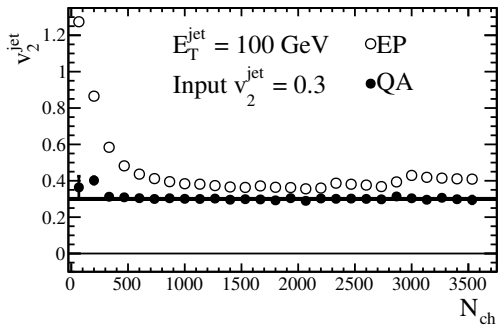

Figure 6.4: Jet v_2 is calculated using the standard (EP) method (open symbols) and the new (QA) method (closed symbols) in simulated events consisting of a PYTHIA jet with $E_{\mathrm{T}}^{\mathrm{jet}} = 100$ GeV embedded in a thermal background ($T = 0.350$ GeV). The p_{T}- and centrality-dependent v_2 values and multiplicities of the background are consistent with observations from ALICE [84, 85]. The simulated jet v_2 is 0.3 and is denoted by a solid line. Statistical errors are smaller than the symbol size.

6.5 Discussion

As shown by the above simulation study, this new method can accurately calculate jet v_2 and the 2$^{\mathrm{nd}}$-order event plane in a simple picture of a jet embedded in a heavy ion background exhibiting elliptic flow. The method also works for higher-order anisotropies.

This method is tested in a simulation that does not include medium-induced jet modification. The decomposition in Eq. (6.1) implies that the bulk particle distribution is independent of the jet. However, if the jet is modified by interactions with the medium, then the bulk must be modified to some degree as well. It is expected that jet-medium interactions would produce structures in the azimuthal distribution of particles that are correlated with (or symmetric about) the jet axis, and therefore jet quenching would be reflected in the event-by-event magnitude of $\mathbf{A}_n$, rather than in $\mathbf{Q}_n$, to first order.

This method does not assume anything about the magnitude of the jet vector (A_n) or about the v_n components of the underlying event. However, the equations

for calculating $v_n^{\rm jet}$ and $\Psi_{{\rm EP},n}$ rely on the assumption that the fluctuations of $Q_{n,x}$ and $Q_{n,y}$ in the participant plane frame can be described by Gaussian distributions. This assumption follows from Ref. [86], although it is noted that there are small deviations from the Gaussian ansatz in peripheral collisions. However, Ref. [87] disputes this assumption, stating that a Gaussian distribution is a poor description of event-by-event fluctuations in a Monte Carlo Glauber model for all but the most central collisions. This new jet v_n method may be generalized to account for different distributions of $Q_{n,x,{\rm PP}}$ and $Q_{n,y,{\rm PP}}$ by rederiving Eqs. (6.5)–(6.9) with alternative non-Gaussian functional forms.

Although the method presented here assumes perfect resolution of the jet axis, accounting for the jet axis resolution in the measurement of $v_2^{\rm jet}$ does not require significant changes to the equations. This method is improved when it is applied in fine bins in centrality (multiplicity) and jet energy, in order for the average quantities ($\langle A_n \rangle$, $\langle Q_n \rangle$, etc) to be meaningful. Unfortunately, high statistics are required in order to obtain reasonable results. For this reason the application of this method may not be feasible at RHIC, whereas statistics may be sufficient at the LHC.

While jets can influence event plane and v_2 measurements, the production of such high-$p_{\rm T}$ jets is rare and therefore only a small subset of events are affected in most event plane analyses. Furthermore, in v_2 analyses of objects that are uncorrelated to jets, the jet – event plane bias only contributes to a small decrease in the event plane resolution. It is only when calculating the v_2 of jets themselves, or particles likely to come from jet production (such as high-$p_{\rm T}$ hadrons), that the jet can cause a significant overestimation in the v_2 calculation.

A measurement of jet v_n for odd n could potentially yield more information about jet quenching than the even $v_n^{\rm jet}$ harmonics. Since parton pairs produced in hard scatterings are essentially symmetric under an azimuthal rotation by π, and

odd harmonics are antisymmetric under the same rotation, it is not possible for jet production to have any intrinsic correlation with an odd event plane. Barring detector acceptance effects, jet reconstruction algorithms will likely find (or assign a higher energy to) the jet in a dijet pair which undergoes less modification. If a nonzero odd v_n^{jet} term is measured, it could be indicative of the correlation between the n^{th}-order event plane and jets which undergo less modification than their recoiling partners, illustrating pathlength-dependent medium-induced jet modification.

Chapter 7

Summary & Conclusions

In this thesis, two analyses of jet quenching and parton energy loss in the QGP are presented. In the jet-hadron correlations analysis, the correlations of charged hadrons with respect to the axis of a reconstructed trigger jet are studied as a function of the jet p_{T} and the associated hadron p_{T}. The trigger jet population is highly-biased towards jets with unmodified fragmentation patterns, making comparisons between Au+Au and p+p jets simpler while potentially enhancing quenching effects on the recoil jet. The yields and widths of the hadron distributions associated with the unbiased recoil jet are studied. The results demonstrate that in Au+Au the associated yields are suppressed at high $p_{\mathrm{T}}^{\mathrm{assoc}}$ and enhanced at low $p_{\mathrm{T}}^{\mathrm{assoc}}$ compared to p+p, therefore interactions with the QGP cause jets to be softer than in vacuum. The suppression of the high-$p_{\mathrm{T}}^{\mathrm{assoc}}$ associated particle yield is in large part balanced by the low-$p_{\mathrm{T}}^{\mathrm{assoc}}$ enhancement. The widths of the recoil jet peak are indicative of broadening at low $p_{\mathrm{T}}^{\mathrm{assoc}}$, although they are highly dependent on the assumed shape of the combinatoric heavy-ion background (in particular, the magnitude of jet v_3). The experimentally-observed redistribution of energy from high-p_{T} fragments to low-p_{T} fragments that remain correlated with the jet axis is qualitatively consistent with

radiative/collisional energy loss models for parton interactions within the QGP. Furthermore, two theoretical models that implement medium-induced radiative energy loss show good quantitative agreement with the experimental data.

An analysis of jet v_2, which quantifies the correlation between the number of reconstructed jets and the azimuthal angle of the reaction plane or 2^{nd}-harmonic participant plane, was also performed. Jet v_2 probes the pathlength-dependence of parton energy loss, since the parton's in-medium pathlength is expected to depend on the QGP geometry. However, reconstructing the event plane in the presence of a jet is non-trivial, since the artificial jet – event plane bias that arises when jet particles are included in the event plane calculation can lead to a significant overestimation of jet v_2. Utilizing the forward detector sub-systems in STAR makes it possible to introduce a pseudorapidity gap between the jet and the particles used to reconstruct the event plane, minimizing the jet – event plane bias. While this measurement is limited by the low event plane resolution in the forward detectors, a non-zero jet $v_2\{\text{FTPC}\}$ is observed. This result demonstrates that in-plane and out-of-plane jets undergo different amounts of quenching (on average), which shows that jet quenching depends on the QGP geometry and is evidence for pathlength-dependent parton energy loss in the QGP.

7.1 Comparison to LHC Results

The first jet results from the LHC clearly demonstrated jet quenching, with back-to-back jets being reconstructed at significantly-different energies [88, 89]. Jet measurements at the LHC span a very different kinematic range from jet studies at RHIC, and they are performed with different techniques (for jet reconstruction, background subtraction, jet energy scale correction, etc), making quantitative comparisons be-

tween the RHIC and LHC results complicated. In particular, in several of the LHC jet analyses only the hard part of the jet fragmentation is studied because the soft part is inaccessible due to detector limitations, and jets that undergo significant modification are excluded from the analyses entirely because they do not satisfy the definitions imposed by jet reconstruction algorithms. Therefore, careful assessments of the biases at both RHIC and the LHC are crucial to the interpretation of the results. Two LHC jet analyses, which are closely related to the STAR results presented in this thesis, are discussed here.

7.1.1 CMS track-jet correlations

CMS has performed an analysis of "track-jet" correlations [89], which are similar to jet-hadron correlations. Dijets are reconstructed using an iterative cone algorithm with a cone radius of $R = 0.5$ (the details of the jet-finding and background subtraction procedures are found in Ref. [89] and references therein). The definition of a reconstructed dijet in this analysis requires: a leading jet with $p_{\mathrm{T}}^{\mathrm{jet},1} > 120$ GeV/c, a subleading jet with $p_{\mathrm{T}}^{\mathrm{jet},2} > 50$ GeV/c, an azimuthal angle difference between the jets of $|\phi^{\mathrm{jet},1} - \phi^{\mathrm{jet},2}| > 2\pi/3$, and both jet axes to be within $0.8 < |\eta| < 1.6$. The total p_{T} (Σp_{T}) within rings of radius $\Delta R = \sqrt{(\Delta\phi)^2 + (\Delta\eta)^2}$ and width 0.08 around the axes of the leading jet and the subleading jet are shown in Fig. 7.1 for tracks in three $p_{\mathrm{T}}^{\mathrm{assoc}}$ bins. The analysis is done in PYTHIA+HYDJET simulated events, which represent the p+p or unmodified jet case, and in Pb+Pb collisions at $\sqrt{s_{NN}} = 2.76$ TeV. The results are shown in bins of A_J, the dijet asymmetry, defined in Eq. 7.1.

$$A_J = \frac{p_{\mathrm{T}}^{\mathrm{jet},1} - p_{\mathrm{T}}^{\mathrm{jet},2}}{p_{\mathrm{T}}^{\mathrm{jet},1} + p_{\mathrm{T}}^{\mathrm{jet},2}} \tag{7.1}$$

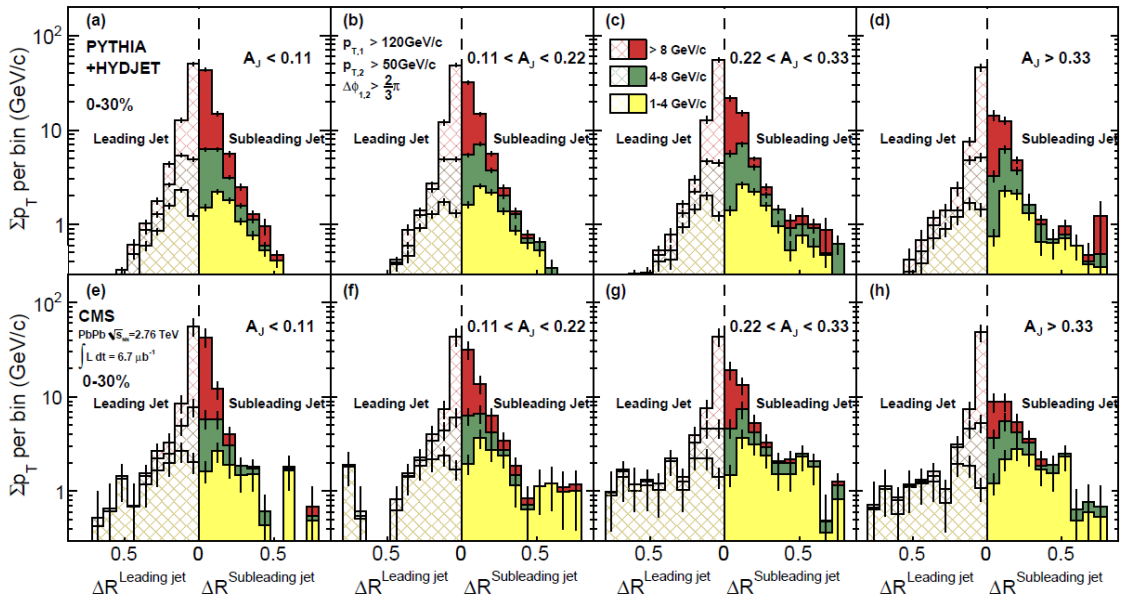

Figure 7.1: Track-jet correlations in CMS are shown in Pb+Pb collisions at $\sqrt{s_{NN}} = 2.76$ TeV (bottom row) and in PYTHIA+HYDJET simulations (top row) for different bins in the dijet asymmetry, A_J (increasing from left to right). Shown here are the $\Delta R = \sqrt{(\Delta\phi)^2 + (\Delta\eta)^2}$ distributions with respect to the leading (hatched) and subleading (solid) jet axes of the total p_{T} in a ring (Σp_{T}) carried by charged tracks in three $p_{\mathrm{T}}^{\mathrm{assoc}}$ bins: $p_{\mathrm{T}}^{\mathrm{assoc}} > 8$ GeV/c (red), $4 < p_{\mathrm{T}}^{\mathrm{assoc}} < 8$ GeV/c (green), and $1 < p_{\mathrm{T}}^{\mathrm{assoc}} < 4$ GeV/c (yellow). Note the logarithmic scale on the vertical axis. [89]

Small A_J indicates that the leading and subleading jets are reconstructed with similar energies, while A_J is large when the leading and subleading jet energies are unbalanced.

From Fig. 7.1 it can be observed that the ΔR distributions look similar in data (Pb+Pb) and simulations (p+p) for balanced dijets (small A_J). Most of the jet momentum is carried by tracks with $p_{\mathrm{T}}^{\mathrm{assoc}} > 8$ GeV/c. As A_J increases, the track distributions around the *leading* jet still show agreement between data and PYTHIA, but the structure of the *subleading* jet (in both p_{T} and ΔR) becomes modified. In particular, the relative number of tracks with $p_{\mathrm{T}}^{\mathrm{assoc}} < 4$ GeV/c increases, and they are observed at larger angles from the jet axis in Pb+Pb compared to PYTHIA. It should be noted that balanced dijet pairs are more common in p+p (represented here

by PYTHIA+HYDJET) while unbalanced dijet pairs are more common in Pb+Pb (and that large-A_J dijets in p+p mostly originate from three-jet events). If the CMS track-jet analysis was integrated over A_J, like the STAR jet-hadron correlations analysis, the ΔR correlation functions would look more like the low-A_J distributions in p+p and more like the high-A_J distributions in Pb+Pb.

The conclusions from the CMS track-jet analysis are generally consistent with the conclusions from the STAR jet-hadron analysis, in that softening and low-$p_{\mathrm{T}}^{\mathrm{assoc}}$ broadening of the recoil (subleading/awayside) jet are observed in heavy ion collisions compared to p+p. However, it is not entirely clear from the CMS measurement whether the low-p_{T} fragments are deflected to large angles in such a way that they remain correlated with the jet axis (as observed in the STAR analysis), or if jet-medium interactions cause an overall "heating" of the QGP which manifests itself as an extra constant background of soft particles at all angles. The difficulty in making such a conclusion about the precise nature of jet broadening is partially due to the jet-finding algorithm imposing a preferred shape on the distribution of particles about the reconstructed jet axis. Both the leading and subleading jet are reconstructed in the CMS measurement, unlike in the STAR jet-hadron measurement where the recoil jet is not subject to any jet definition that may bias its fragmentation pattern. In the track-jet analysis, it can be seen that the fragmentation of the subleading jet is biased by the resolution parameter used in the jet finding algorithm ($R = 0.5$), since there is a discontinuity in the track distribution around $\Delta R = 0.5 - 0.6$ in Pb+Pb. The dip at $\Delta R \sim 0$ in the low-$p_{\mathrm{T}}^{\mathrm{assoc}}$ bins may also be due to the behavior of the jet-finder. An analysis in which the recoil jet is not required to have a p+p-like hard core with $p_{\mathrm{T}} > 50$ GeV/c contained within a fixed cone radius would be more informative for theories of medium-induced jet shape modification at the LHC.

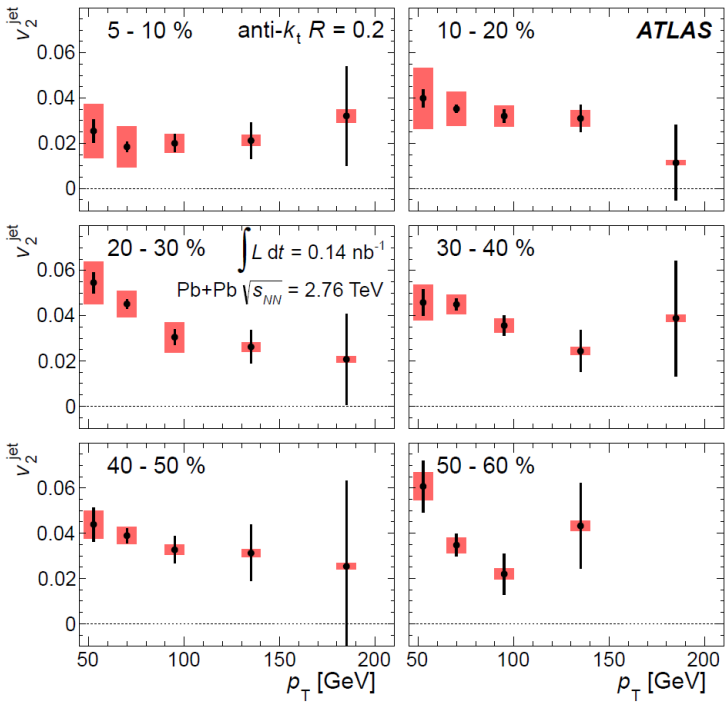

Figure 7.2: Jet v_2 is measured by ATLAS in Pb+Pb collisions at $\sqrt{s_{NN}} = 2.76$ TeV for $R = 0.2$ anti-k_T jets in the range $45 < p_T^{jet} < 210$ GeV/c. The results are shown in six centrality bins. [90]

7.1.2 ATLAS jet v_2

Jet v_2 measurements have been done at both RHIC and the LHC. ATLAS has performed an analysis of jet v_2 [90] for $R = 0.2$ anti-k_T jets with $45 < p_T^{jet} < 210$ GeV/c, shown in Fig. 7.2. (For details about jet reconstruction in ATLAS see Refs. [90] and [91].) As in the STAR jet v_2 analysis, a non-zero jet v_2 is also observed in ATLAS, so both experiments conclude that parton energy loss has a pathlength dependence. However, the cuts used in the jet finding and background subtraction procedure are quite different in the two analyses, meaning that not only are the kinematic ranges different between the experiments, but they also probe jets with different biases and so the results are also qualitatively different. For example, ATLAS sees hints of a decrease in jet v_2 with jet p_T, which is expected but not observed in the STAR measurement. As discussed in Section 5.6.2, this may be due to the very biased jet definition that is used in the STAR measurement, while the jets reconstructed in ATLAS do not have such a high constituent p_T cut relative

to the reconstructed jet energies. Some centrality dependence is also observed by ATLAS, particularly in the $60 < p_{\mathrm{T}}^{\mathrm{jet}} < 80$ GeV/c bin (see Fig. 3 in Ref. [90]). Jet v_2 decreases in the most central and most peripheral events, which is expected from geometrical considerations and consistent with single-particle v_2 measurements. CMS has also measured the v_2 of very high-p_{T} hadrons [92], and observes a non-zero v_2 up to $p_{\mathrm{T}} \approx 40$ GeV/c with a similar dependencies on centrality and p_{T}. Although the overall qualitative conclusions of these analyses are consistent, further work is needed before these measurements at RHIC and the LHC can be quantitatively or qualitatively compared in more detail.

7.2 Outlook

There are several possible ways that the analyses presented in this thesis can be improved and extended in the future.

The jet-hadron correlations analysis is systematics-limited at low-$p_{\mathrm{T}}^{\mathrm{assoc}}$ by the uncertainty in the magnitude of jet v_2 and jet v_3. Since the measurement of jet v_2 in Chapter 5 has large uncertainties and uses a slightly different jet definition than the one used in the jet-hadron correlations analysis, and jet v_3 has not been measured, it was necessary to place very conservative uncertainties on the shape of the background in the jet-hadron correlations analysis. A precise measurement of jet v_3 would make it possible to draw stronger conclusions about low-$p_{\mathrm{T}}^{\mathrm{assoc}}$ broadening. Unfortunately, the jet v_2 and jet v_3 measurements in STAR are limited by the event plane resolution in the forward detectors.

The method for measuring jet v_n presented in Chapter 6 utilizes knowledge of the jet axis from full jet reconstruction to accurately calculate jet v_2 and v_3 as well as an event plane at mid-rapidity that is, on average, unbiased by the presence of a jet.

Unfortunately, the new method requires high statistics to be accurate, and it was not possible to use this method to determine jet v_2 and v_3 in the 2007 Au+Au data set at STAR. The higher statistics available in later years at STAR (particularly 2010 and 2011) and at the LHC may make it possible to measure jet v_2 and v_3 with the new method.

In addition to jet v_2, another potential measurement that can inform theories of pathlength-dependent parton energy loss is jet-hadron correlations with respect to the event plane. It is expected, and evident from the results of the jet v_2 analysis, that in-plane jets undergo less quenching than out-of-plane jets. It would be informative to investigate both the softening (measured with the I_{AA} and D_{AA} observables) and broadening (of the Gaussian widths) of jets as a function of the relative angle between the jet and the event plane. This analysis was attempted prior to discovering the significant jet – event plane bias, and before jet v_2 had been measured. Now that tools exist for calculating the event plane in the presence of a jet (utilizing the FTPC, or the method presented in Chapter 6), and the jet v_n coefficients (which are crucial for background subtraction) are being investigated, a measurement of the event plane dependence of jet-hadron correlations should be possible in the near future.

These advancements in the jet-hadron correlations and jet v_2 analyses may be possible with the new high-statistics $\sqrt{s_{NN}} = 200$ GeV Au+Au data set recorded in 2011. For example, in the jet-hadron correlations analysis there were 2.8k jets reconstructed in the range $20 < p_{\mathrm{T}}^{\mathrm{jet,rec}} < 40$ GeV/c in the 0-20% central events in the Run 7 Au+Au HT data set. In Run 11 there are anticipated to be ~2k events reconstructed with $p_{\mathrm{T}}^{\mathrm{jet,rec}} > 50$ GeV/c (with more lenient jet reconstruction parameters, such as a low constituent p_{T} cut) in 0-10% central Au+Au collisions [93]. In addition, efforts are ongoing in STAR to obtain an improved jet spectrum measurement in the new 2011 high-statistics data set [93]. Furthermore, the STAR jet spectrum

is being measured with similar techniques as those used in the ALICE jet spectrum measurement [94]. This will make it possible to do a *direct* quantitative comparison between the jets observed in STAR at RHIC and in ALICE at the LHC.

Future LHC jet measurements (and some that are already ongoing) will provide even more detailed information about parton energy loss in the QGP. For example, it will be possible to precisely determine the energy and direction of partons that recoil from high-p_{T} electroweak probes (photons [95] and even Z^0 bosons), which do not interact with the QGP and are produced in abundance at the LHC, without resorting to jet-finding algorithms. Furthermore, the ability of the LHC experiments to directly reconstruct heavy flavor hadrons will make it possible to tag jets originating from heavy quarks [96], and thus contrast the energy loss of light partons and heavy quarks. It may also be possible to discriminate between gluon jets and quark jets in the future. At low p_{T}, the particle identification capabilities of the LHC experiments, particularly ALICE, will make it possible to study how quenching alters jet chemistry in heavy ion collisions, providing information to models of jet fragmentation and hadronization.

Complementary studies of jets at RHIC and the LHC can cover a huge kinematic range, from $5 < p_{\mathrm{T}}^{\gamma} < 10$ GeV/c in γ-hadron studies in PHENIX [97], to reconstructed jets in the ranges of $10 < p_{\mathrm{T}}^{\mathrm{jet,rec}} < 40$ GeV/c in STAR and $30 < p_{\mathrm{T}}^{\mathrm{jet}} < 100$ GeV/c in ALICE [94], to $50 < p_{\mathrm{T}}^{\mathrm{jet}} < 350$ GeV/c jets in CMS and ATLAS [98, 99]. The collection of jet measurements over such a large range of energies will provide stringent constraints on theories of parton energy loss in the QGP.

Appendix A

Charged Particle Tracking Efficiency

The TPC tracking efficiency is defined as the probability of reconstructing a track when a charged particle passes through the TPC. The tracking efficiency must be determined in both p+p and Au+Au environments, and depends on the detector performance when the data was taken, the configuration of the reconstruction software when the data was produced, and the track quality cuts that are imposed during the data analysis. The tracking efficiency is a function of the azimuthal angle (ϕ), pseudorapidity (η), and transverse momentum (p_{T}) of the particle, as well as the multiplicity and z-vertex position (v_z) of the event.

A.1 Y06 p+p

The tracking efficiency in Run 6 p+p collisions is determined by simulating p+p collisions in PYTHIA and running the simulated p+p events through the STAR reconstruction software chain. Each track that is reconstructed is then matched to

the nearest simulated Monte Carlo (MC) track. The criteria that the Monte Carlo and matched tracks must satisfy are summarized in Table A.1. Two histograms are filled with the (p_{T}, η) distributions of the simulated Monte Carlo tracks and the reconstructed tracks that satisfy the track quality cuts used in the analysis. The ratio of the latter to the former gives the (p_{T}, η)-dependent probability of reconstructing a track in the TPC (and also accounts for the track p_{T} resolution).

Monte Carlo tracks	Reconstructed matched tracks
Geant id = 8, 9, 11, 12, 14, 15	Geant id of MC track = 8, 9, 11, 12, 14, 15
refmult > 0	refmult > 0
$v_x^2 + v_y^2 < 2^2$	$v_x^2 + v_y^2 < 2^2$
$\lvert v_z \rvert < 25$ cm	$\lvert v_z \rvert < 25$ cm
$\lvert \eta \rvert < 1$	$\lvert \eta \rvert < 1$
IsPrimary = 1	MC track with matching Key has IsPrimary = 1.
	$p_{T,pr}^2 + p_{z,pr}^2 > 0.1^2$
	Number of fit points ≥ 20
	Number of fit points / Possible fit points > 0.55
	DCA < 1

Table A.1: The cuts used to select MC tracks and matched tracks in the Y06 tracking efficiency calculation. The Geant ID selects $\pi^{\pm}$, $K^{\pm}$, p, and $\bar{p}$. Refmult is the uncorrected multiplicity within $|\eta| < 0.5$.

The resulting tracking efficiency is shown as a function of p_{T} and η in Fig. A.1a. A parameterization of this two-dimensional histogram was obtained in two steps.

First, the p_{T}-dependence of the efficiency was fit with the one-dimensional functional form $a_0 - a_1 e^{a_2/p_{\mathrm{T}}} + \mathrm{gausn}(a_3) - \mathrm{gausn}(a_6)$, where gausn represents a normalized Gaussian ($\mathrm{gausn}(a_3) = a_3(2\pi a_5^2)^{-1/2} e^{-(p_{\mathrm{T}}-a_4)^2/(2a_5^2)}$). Since the PYTHIA events are simulated in different $p_{\mathrm{T}}^{\mathrm{hard}}$ bins (5-7, 7-9, 9-11, 11-15, 15-25, 25-35, 35-45, 45-55, and 55-65 GeV/c), the fits to the efficiency were at first performed separately for each $p_{\mathrm{T}}^{\mathrm{hard}}$ bin. It is observed in Fig. A.1b that the tracking efficiency curves do not depend largely on the $p_{\mathrm{T}}^{\mathrm{hard}}$ bin, and so the bins were combined (with equal weighting, not weighted by a p_{T} spectrum) to obtain better statistical precision. The tracking

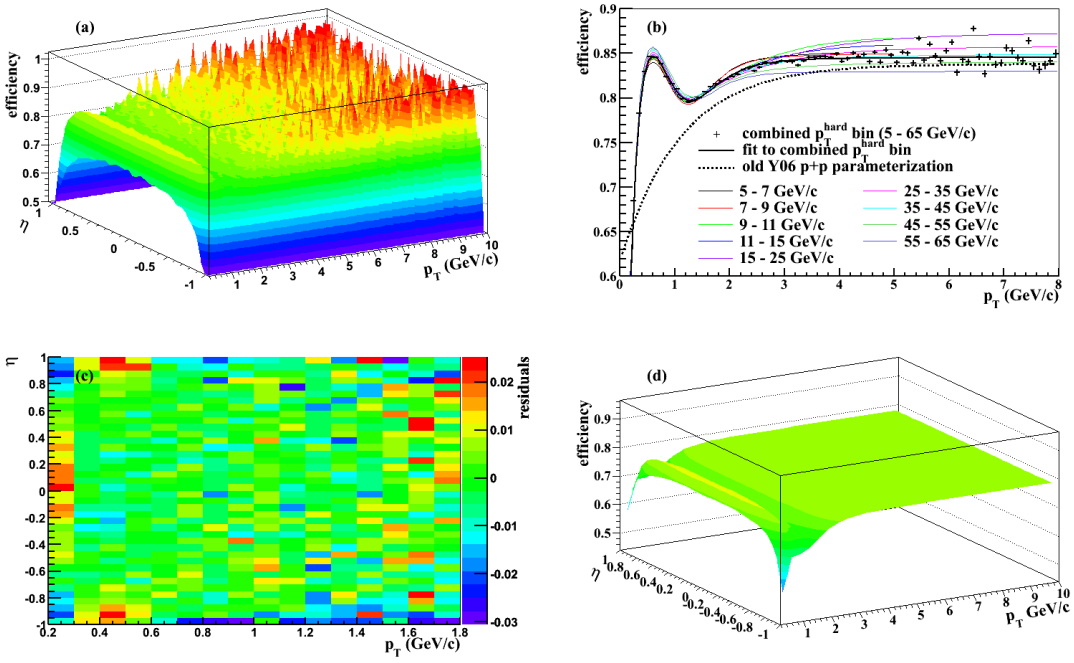

Figure A.1:
(a) The Run 6 tracking efficiency as a function of p_{T} and η.
(b) The tracking efficiency as a function of p_{T}. The fits in each $p_{\mathrm{T}}^{\mathrm{hard}}$ bin are shown in thin colored lines. The black points are from the combined 5-65 GeV/c $p_{\mathrm{T}}^{\mathrm{hard}}$ bin, and the thick black line is the fit to those points. The parameterization in [100] is shown in the dashed black line.
(c) The difference between the calculated tracking efficiency and the parameterization (without the 0.06 shift).
(d) The final parameterization of the 2006 p+p tracking efficiency.

efficiency for the combined $5 < p_{\mathrm{T}}^{\mathrm{hard}} < 65$ GeV/c bin, and its fit, are shown in Fig. A.1b. The previous parameterization of the Run 6 tracking efficiency [100] is also shown in Fig. A.1b; it does not describe the efficiency well below 2 GeV/c.

Next, the 1D p_{T}-dependent parameterization was subtracted from the 2D efficiency histogram and the remainder was fit with the functional form $(b_0 - b_1(\eta - b_2)^2 - b_3(\eta - b_2)^4 - b_4(\eta - b_2)^6 - b_5(\eta - b_2)^8)e^{-b_6 p_{\mathrm{T}}}$. The sum of the 1D p_{T}-dependent fit and the 2D (p_{T}, η)-dependent fit yields the final parameterization. The final residuals are shown in Figure A.1c. Although there is some structure in the residuals (at large η and for $0.2 < p_T < 0.3$), the errors are within the standard tracking efficiency

uncertainty of 5%.

Finally, it was shown in Ref. [101] that the PYTHIA events are too "clean", and that the tracking efficiency obtained from embedding jets in real p+p data is lower by 6% than the tracking efficiency obtained from reconstructed PYTHIA events. This factor of 6% is roughly constant in η and p_T. Therefore, 0.06 is subtracted from the efficiency.

The final parameterization of the year 6 tracking efficiency is shown in Figure A.1d. It is important to note that the parameterization is only valid for $p_T > 0.2$ GeV/c and $|\eta| < 1$. The parameterization can be obtained with the following ROOT function:

```
TF2* GetEffY06()
{
   TF2* funcpp = new TF2("ppEfficiency","[0]-0.06-[1]*exp([2]/x)
                 +[3]*exp(-0.5*((x-[4])/[5])**2)/sqrt(2*pi*[5]*[5])
                 -[6]*exp(-0.5*((x-[7])/[8])**2)/sqrt(2*pi*[8]*[8])
                 +([9]-[10]*(y-[11])^2-[12]*(y-[11])^4-[13]*(y-[11])^6
                 -[14]*(y-[11])^8)*exp(-[15]*x)",0.,10.,-1.,1.);
   Double_t parset[] = {0.869233,0.0223402,0.44061,0.558762,0.145162,
                        0.508033,110.008,-4.63659,1.73765,0.0452674,
                        -0.101279,0.0081551,0.945287,-2.00949,1.61746,
                        1.39352};
   ((TF2*)funcpp)->SetParameters(parset);
   return funcpp;
}
```

A.2 Y07 Au+Au

Typically, the tracking efficiency in heavy ion events in STAR is determined by embedding simulated tracks into real heavy ion events, reconstructing the event with the STAR reconstruction software chain, finding the reconstructed tracks which match the simulated tracks, and calculating the probability that a simulated track

Centrality	Run 4	Run 7
0-5%	519	484
5-10%	440	398
10-20%	318	268

Table A.2: The non-inclusive (g)refmult cuts for Run 4 [104] and Run 7 [105]. Note that Run 4 uses refmult while Run 7 uses grefmult.

is reconstructed. However, this type of embedding was not available for the 2007 Au+Au data, so an alternative method for obtaining the tracking efficiency was necessary. The p_{T}- and η-dependent tracking efficiency in the previous Au+Au run (2004) had been parameterized in Refs. [102] and [103], so the relative TPC acceptance between Runs 4 and 7 was used to convert the Run 4 efficiency to the Run 7 efficiency.

The (p_{T}, η) distribution of tracks was produced for the Run 4 MB, Run 7 MB, and Run 7 HT data sets. The per-event track distribution was produced separately for each of the three centrality bins 0-5%, 5-10%, and 10-20%, using the refmult cuts appropriate for the given year, which are shown in Table A.2.

Below $p_{\mathrm{T}} = 1.5$ GeV/c the Run 7 HT / Run 4 MB relative efficiency in (p_{T}, η) is used to scale the Run 4 efficiency to obtain the Run 7 efficiency (in HT events). However, the HT data set shows an excess of high-p_{T} tracks due to the trigger requirement, as seen in Fig. A.2, while the Run 7 MB / Run 4 MB ratio is roughly flat as a function of p_{T} beyond $p_{\mathrm{T}} \approx 1.2$ GeV/c. Therefore, for $p_{\mathrm{T}} > 1.5$ GeV/c, the Run 7 HT / Run 4 MB relative efficiency in η between $1.2 < p_{\mathrm{T}} < 1.8$ GeV/c is used to scale the Run 4 efficiency. For each of the centrality bins, Figs. A.4–A.6 show the Run 4 efficiency (a), the Run 7 / Run 4 scale factors (b,c) and the final Run 7 efficiency (d). Figure A.3 shows the comparison between the Run 4, Run 6, and Run 7 efficiencies as a function of p_{T}.

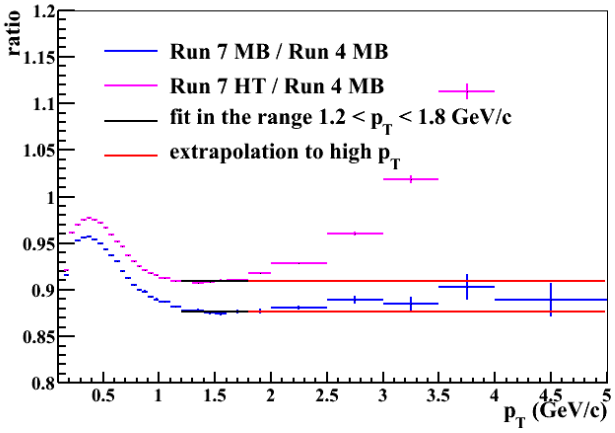

Figure A.2: The Run 7 HT / Run 4 MB (pink) and Run 7 MB / Run 4 MB (blue) ratios are shown as a function of p_{T} in the 10-20% centrality bin. For $p_{\mathrm{T}} \gtrsim 1.5$ GeV/c there is an enhancement of tracks in the HT data, while the ratio for the Run 7 MB data is roughly constant, as shown by the horizontal lines, which are a fit to the data within $1.2 < p_{\mathrm{T}} < 1.8$ GeV/c (black) and an extrapolation to higher p_{T} (red). In the two more central bins, the difference between the HT and MB points at low p_{T} is not so large.

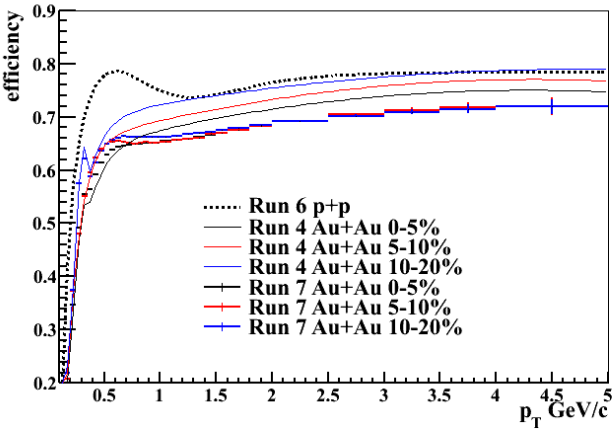

Figure A.3: The efficiencies for Run 6 p+p, Run 4 Au+Au, and Run 7 Au+Au are compared as a function of p_{T}.

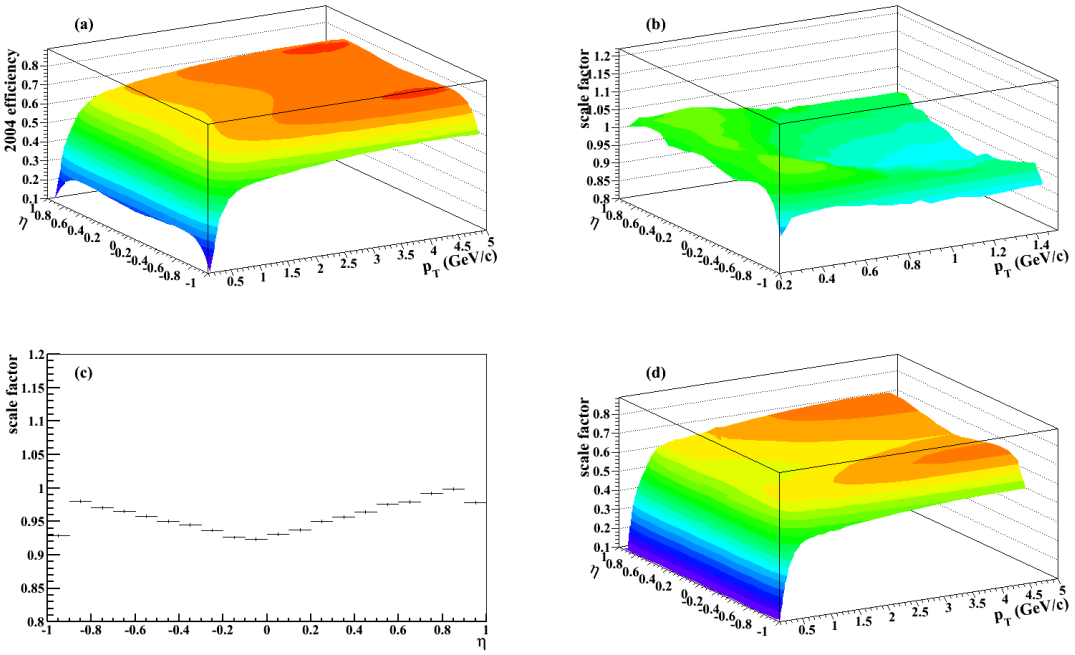

Figure A.4: Tracking efficiency for 0-5% central events.
(a) The Run 4 tracking efficiency.
(b) The Run 7 HT / Run 4 MB ratio in (p_{T}, η) which is used to scale the Run 4 efficiency for $p_{\mathrm{T}} < 1.5$ GeV/c.
(c) The Run 7 HT / Run 4 MB ratio in η which is used to scale the Run 4 efficiency for $p_{\mathrm{T}} > 1.5$ GeV/c.
(d) The Run 7 tracking efficiency.

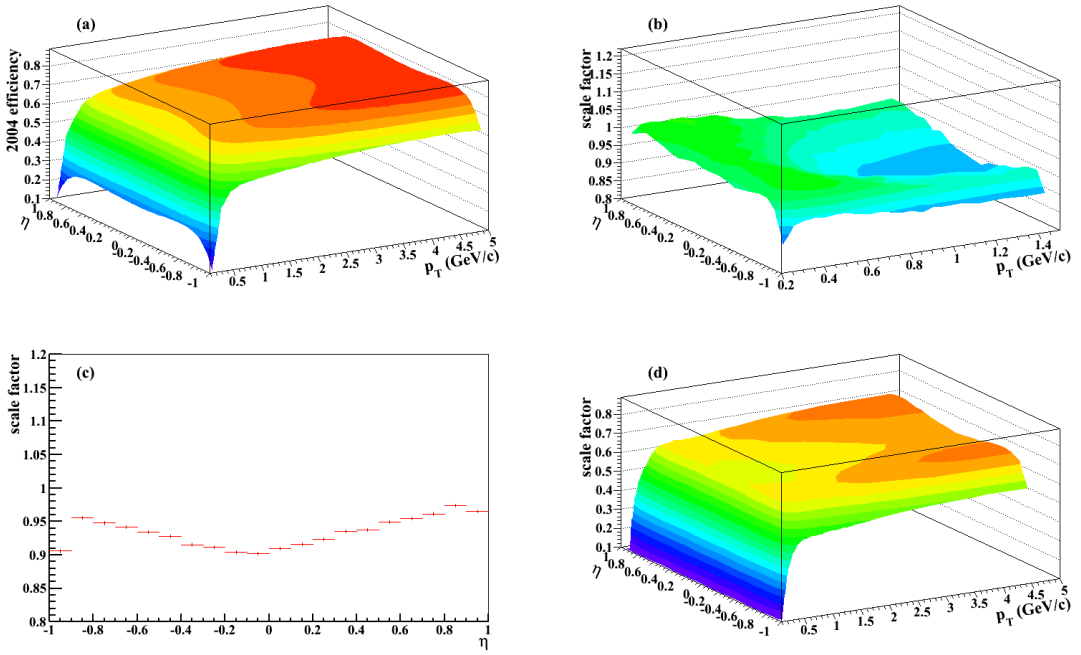

Figure A.5: Tracking efficiency for 5-10% central events.
(a) The Run 4 tracking efficiency.
(b) The Run 7 HT / Run 4 MB ratio in (p_{T}, η) which is used to scale the Run 4 efficiency for $p_{\mathrm{T}} < 1.5$ GeV/c.
(c) The Run 7 HT / Run 4 MB ratio in η which is used to scale the Run 4 efficiency for $p_{\mathrm{T}} > 1.5$ GeV/c.
(d) The Run 7 tracking efficiency.

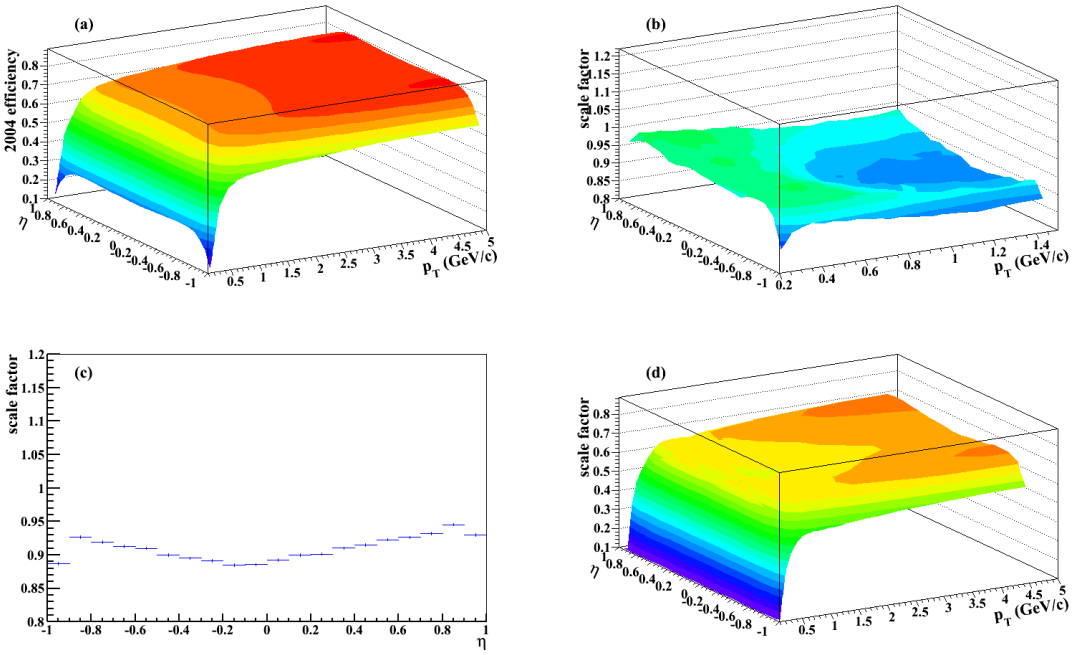

Figure A.6: Tracking efficiency for 10-20% central events.
(a) The Run 4 tracking efficiency.
(b) The Run 7 HT / Run 4 MB ratio in (p_{T}, η) which is used to scale the Run 4 efficiency for $p_{\mathrm{T}} < 1.5$ GeV/c.
(c) The Run 7 HT / Run 4 MB ratio in η which is used to scale the Run 4 efficiency for $p_{\mathrm{T}} > 1.5$ GeV/c.
(d) The Run 7 tracking efficiency.

A.3 Tracking Efficiency Uncertainty

The standard STAR value of $\pm 5\%$ is used for the absolute systematic uncertainty in p+p. Since the analyses in this thesis only concern relative quantities between Au+Au and p+p, it is only necessary to compute the systematic uncertainty on the difference of the tracking efficiency in Au+Au and p+p, and on the ratio of the tracking efficiency in Au+Au and p+p for $p_{\mathrm{T}} > 2$ GeV/c.

The difference between the tracking efficiencies in Run 4 and Run 7 is approximately 3% in the 0-5% centrality bin, so this is taken as a conservative estimate of the run-dependence of the tracking efficiency. This uncertainty applies to both Run 6 (p+p) and Run 7 (Au+Au), in other words, it should be applied twice. Furthermore, it is noted that, strangely, the efficiencies in Figure A.3 appear to be independent of centrality. A Au+Au-specific uncertainty of 4% is assigned to account for this centrality dependence. Adding these uncertainties in quadrature gives $3\% \oplus 3\% \oplus 4\% = 6\%$ as the total uncertainty on the relative tracking efficiency difference between Au+Au and p+p.

In the range $p_{\mathrm{T}} > 2$ GeV/c, the tracking efficiency is 70% in Au+Au and 78% in p+p, so the ratio is 90%. The uncertainty on the ratio is therefore calculated to be $90\% \times \sqrt{(3\%/78\%)^2 + ((3\% \oplus 4\%)/70\%)^2} = 7\%$. This ratio and its uncertainty are applied in the p+p HT + Au+Au MB embedding in Section 4.7.

Appendix B

Jet-hadron Correlation Functions

B.1 $10 < p_{\mathrm{T}}^{jet,rec} < 15$ GeV/c

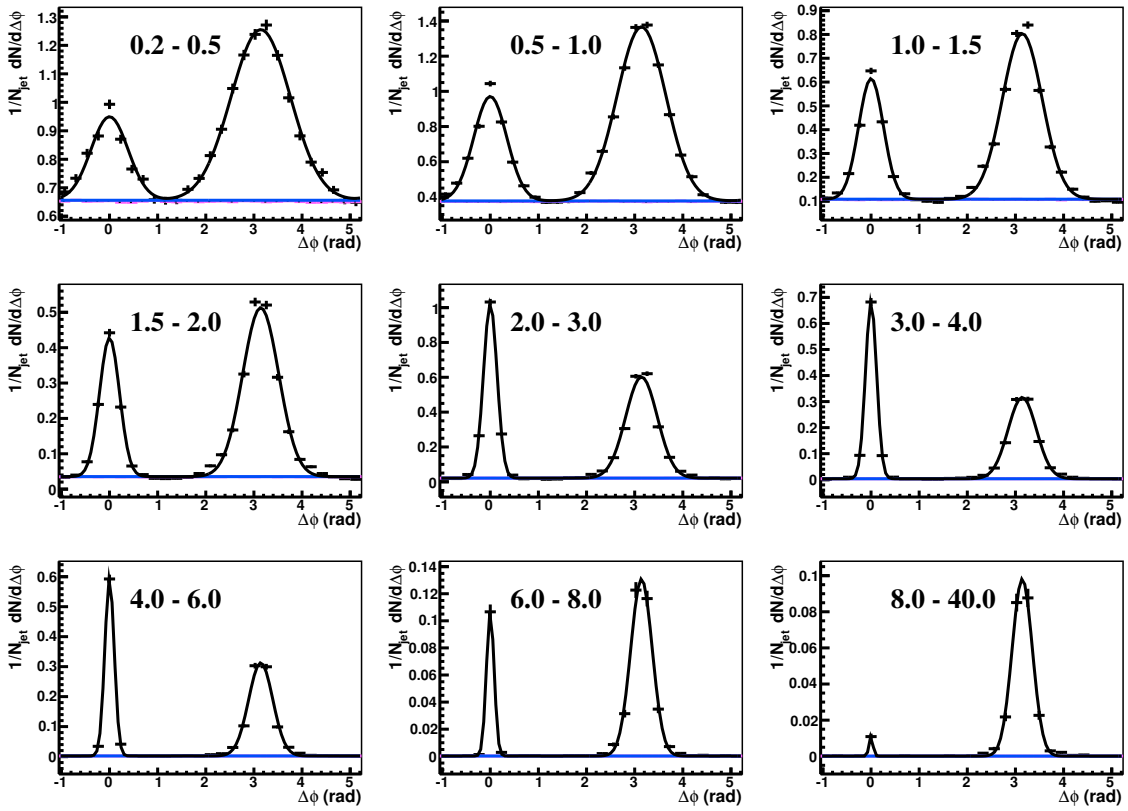

Figure B.1: $\Delta\phi$ correlations in p+p for $10 < p_{\mathrm{T}}^{jet,rec} < 15$ GeV/c. The p_{T}^{assoc} values (in GeV/c) are shown in each panel. The fit to the points (Eq. 4.4) is shown by a black line, the flat background is shown in blue. The mixed event background is shown in pink points, scaled up to the background level B (although the points are mostly obscured by the blue background line).

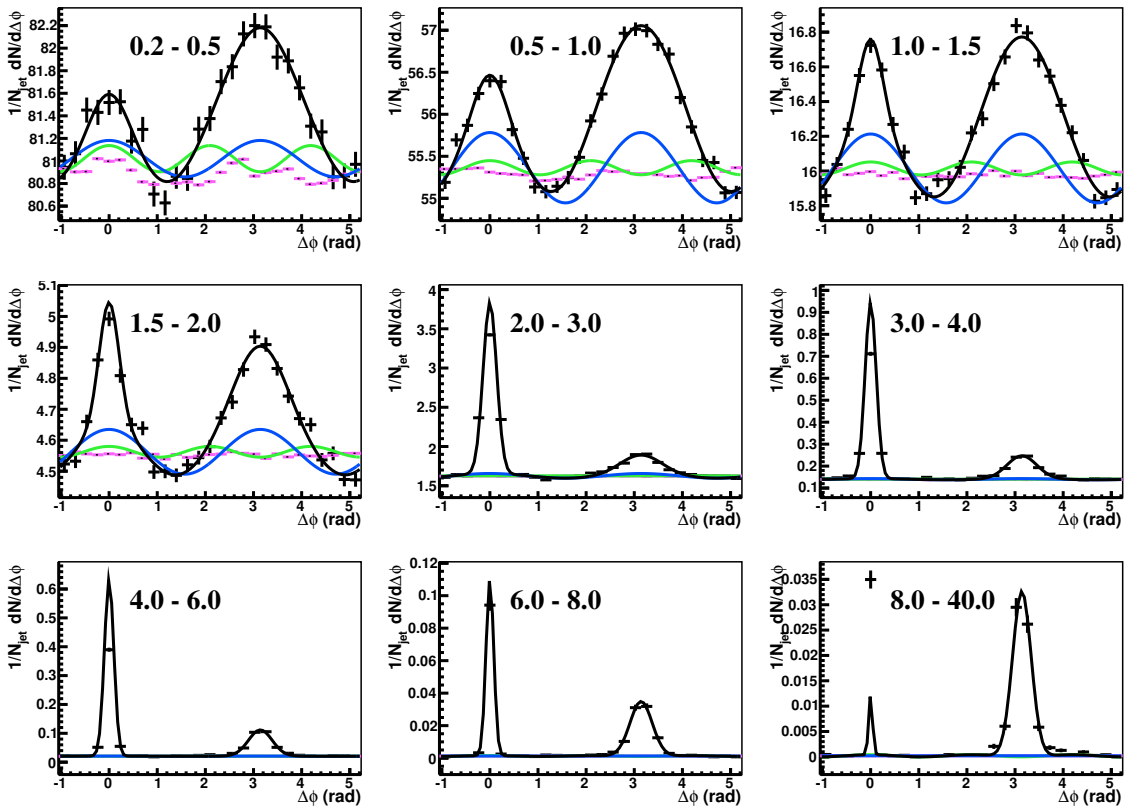

Figure B.2: $\Delta\phi$ correlations in Au+Au for $10 < p_{\mathrm{T}}^{jet,rec} < 15$ GeV/c with the *mean* v_2 background assumption and nearside yield/width matching. The p_{T}^{assoc} values (in GeV/c) are shown in each panel. The fit to the points (Eq. 4.4) is shown by a black line, the v_2 and v_3 components of the fit are shown in blue and green, respectively. The mixed event background is shown in pink points, scaled up to the background level B.

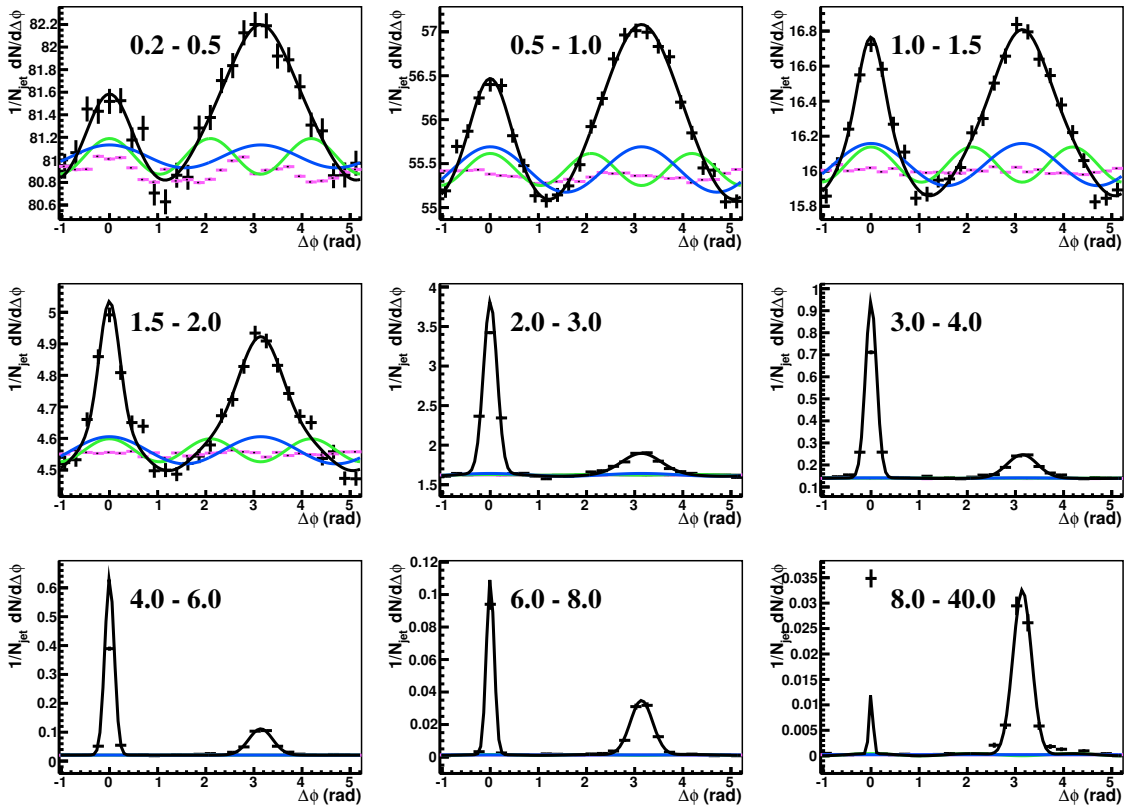

Figure B.3: $\Delta\phi$ correlations in Au+Au for $10 < p_{\mathrm{T}}^{jet,rec} < 15$ GeV/c with the *minimum* v_2 background assumption and nearside yield/width matching. The p_{T}^{assoc} values (in GeV/c) are shown in each panel. The fit to the points (Eq. 4.4) is shown by a black line, the v_2 and v_3 components of the fit are shown in blue and green, respectively. The mixed event background is shown in pink points, scaled up to the background level B.

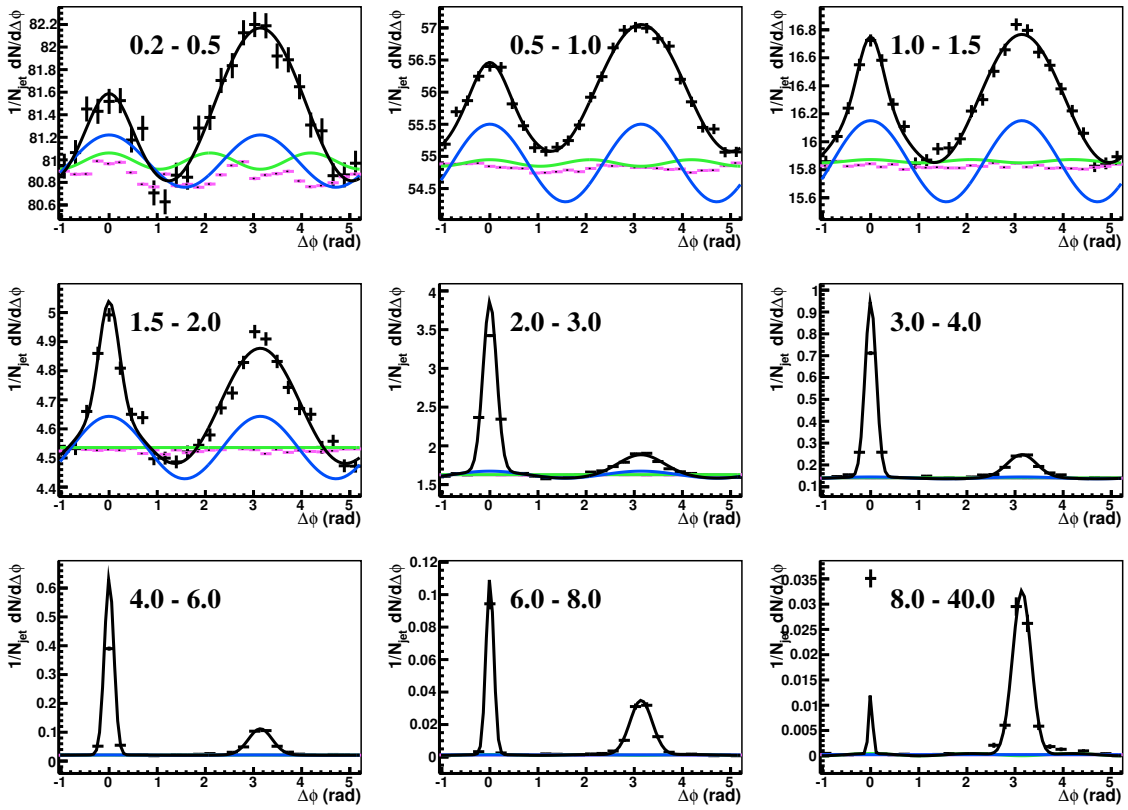

Figure B.4: $\Delta\phi$ correlations in Au+Au for $10 < p_{\mathrm{T}}^{jet,rec} < 15$ GeV/c with the *maximum* v_2 background assumption and nearside yield/width matching. The p_{T}^{assoc} values (in GeV/c) are shown in each panel. The fit to the points (Eq. 4.4) is shown by a black line, the v_2 and v_3 components of the fit are shown in blue and green, respectively. The mixed event background is shown in pink points, scaled up to the background level B.

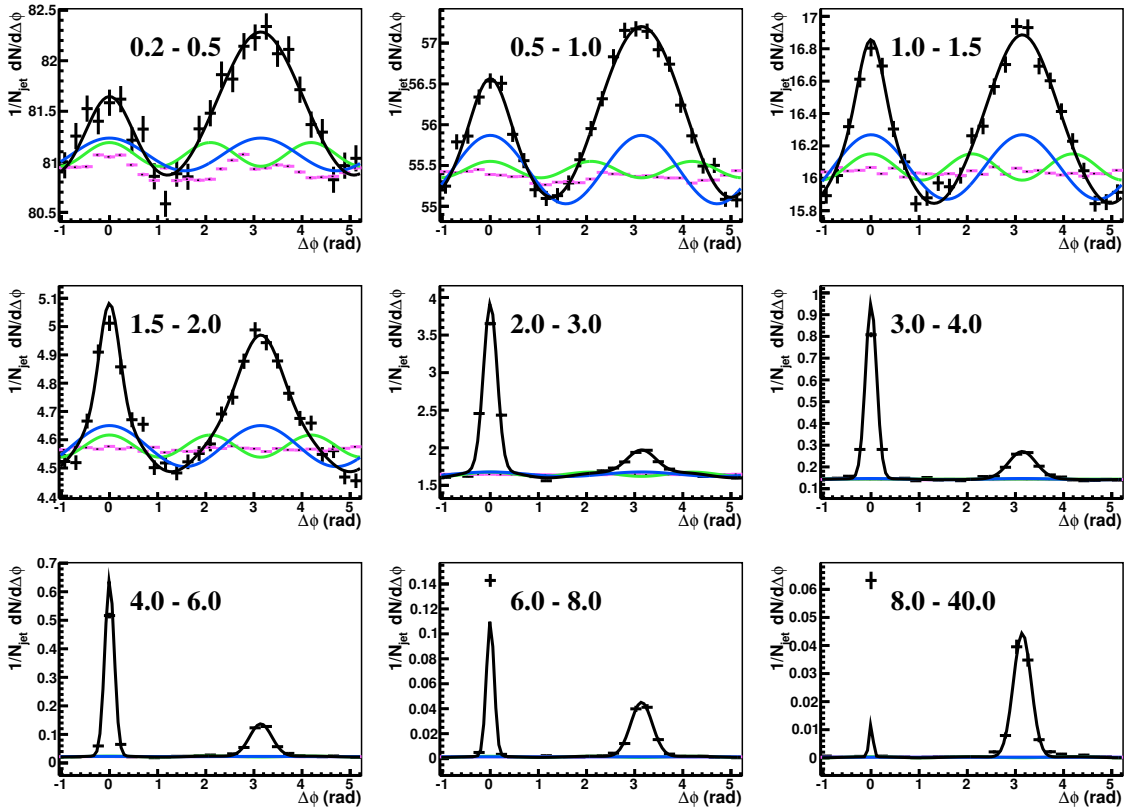

Figure B.5: $\Delta\phi$ correlations in Au+Au for $10 < p_{\mathrm{T}}^{jet,rec} < 15$ GeV/c with the mean v_2 background assumption and nearside yield/width matching *after the* ΔE *shift*. The p_{T}^{assoc} values (in GeV/c) are shown in each panel. The fit to the points (Eq. 4.4) is shown by a black line, the v_2 and v_3 components of the fit are shown in blue and green, respectively. The mixed event background is shown in pink points, scaled up to the background level B.

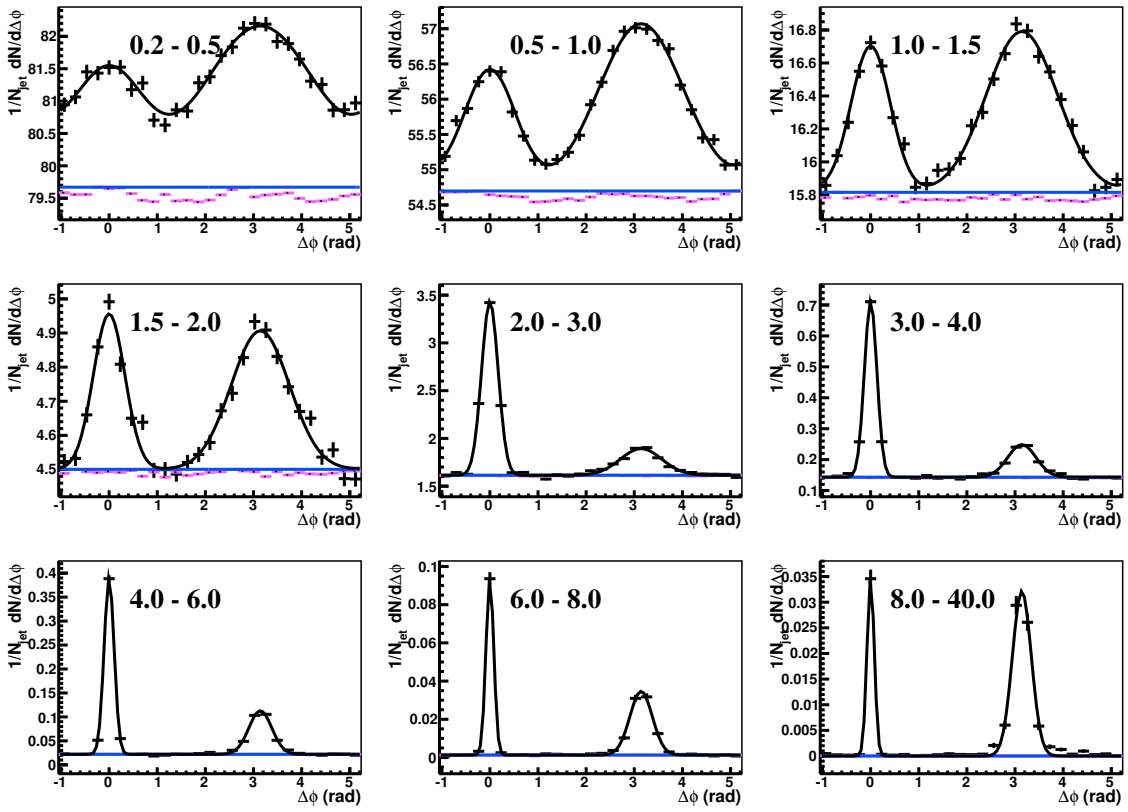

Figure B.6: $\Delta\phi$ correlations in Au+Au for $10 < p_{\mathrm{T}}^{jet,rec} < 15$ GeV/c with the *zero* v_2 background assumption. The p_{T}^{assoc} values (in GeV/c) are shown in each panel. The fit to the points (Eq. 4.4) is shown by a black line, the flat background is shown in blue. The mixed event background is shown in pink points, scaled up to the background level B.

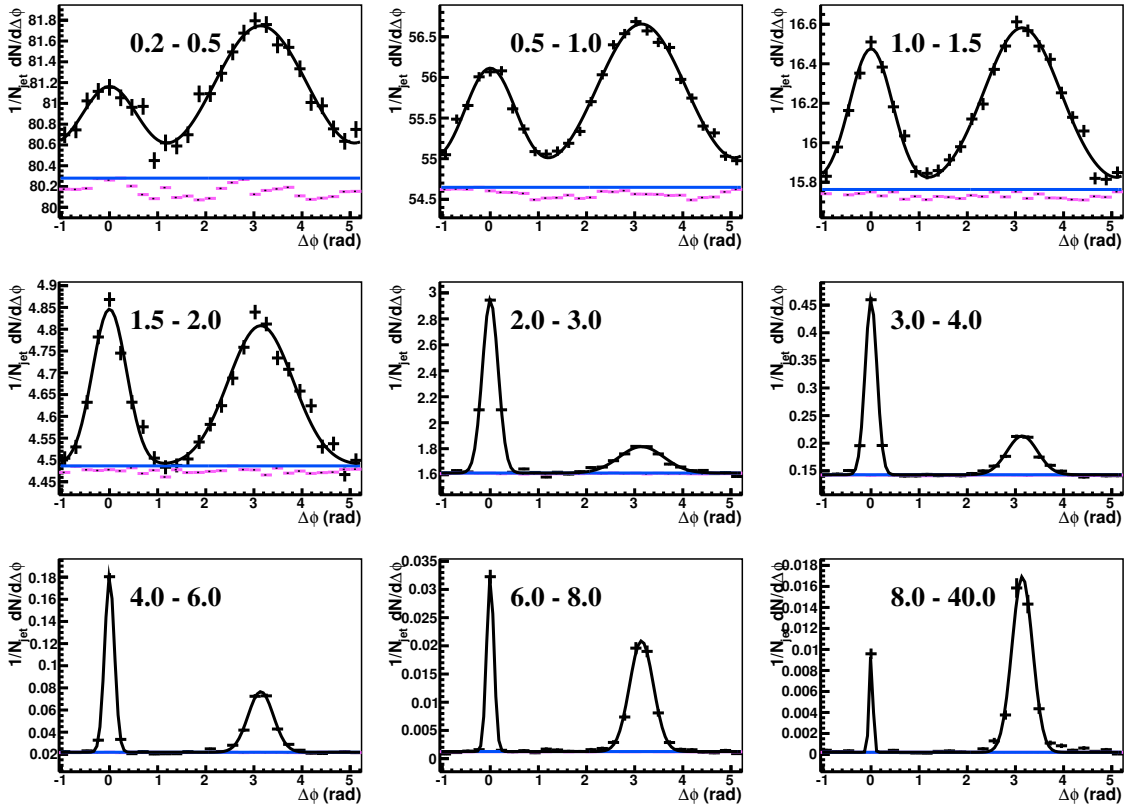

Figure B.7: $\Delta\phi$ correlations in Au+Au for $10 < p_{\mathrm{T}}^{jet,rec} < 15$ GeV/c with the zero v_2 background assumption *after the* ΣD_{AA} *shift*. The p_{T}^{assoc} values (in GeV/c) are shown in each panel. The fit to the points (Eq. 4.4) is shown by a black line, the flat background is shown in blue. The mixed event background is shown in pink points, scaled up to the background level B.

B.2 $15 < p_{\mathrm{T}}^{jet,rec} < 20$ GeV/c

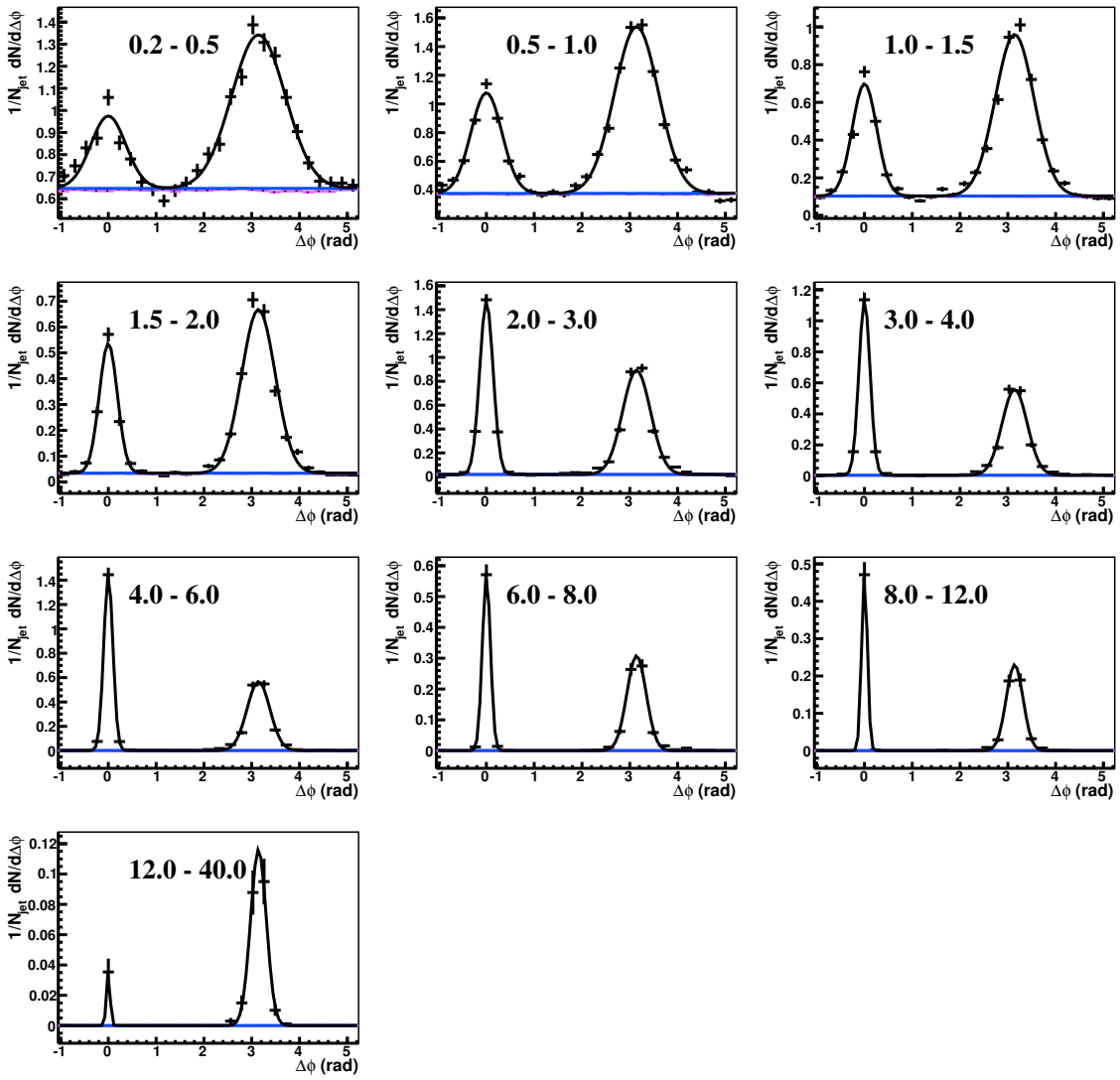

Figure B.8: $\Delta\phi$ correlations in p+p for $15 < p_{\mathrm{T}}^{jet,rec} < 20$ GeV/c. The p_{T}^{assoc} values (in GeV/c) are shown in each panel. The fit to the points (Eq. 4.4) is shown by a black line, the flat background is shown in blue. The mixed event background is shown in pink points, scaled up to the background level B (although the points are mostly obscured by the blue background line).

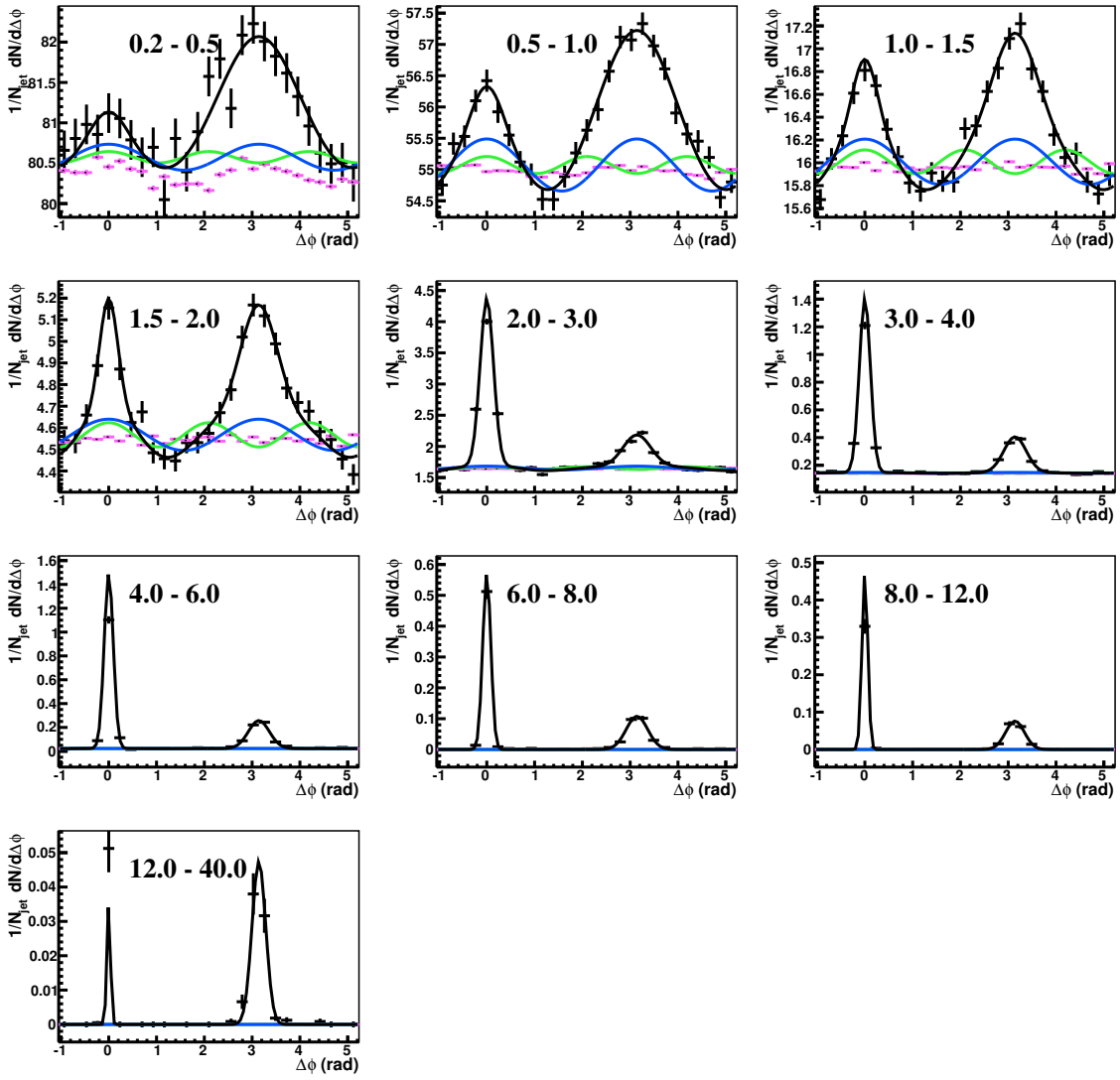

Figure B.9: $\Delta\phi$ correlations in Au+Au for $15 < p_{\mathrm{T}}^{jet,rec} < 20$ GeV/c with the *mean* v_2 background assumption and nearside yield/width matching. The p_{T}^{assoc} values (in GeV/c) are shown in each panel. The fit to the points (Eq. 4.4) is shown by a black line, the v_2 and v_3 components of the fit are shown in blue and green, respectively. The mixed event background is shown in pink points, scaled up to the background level B.

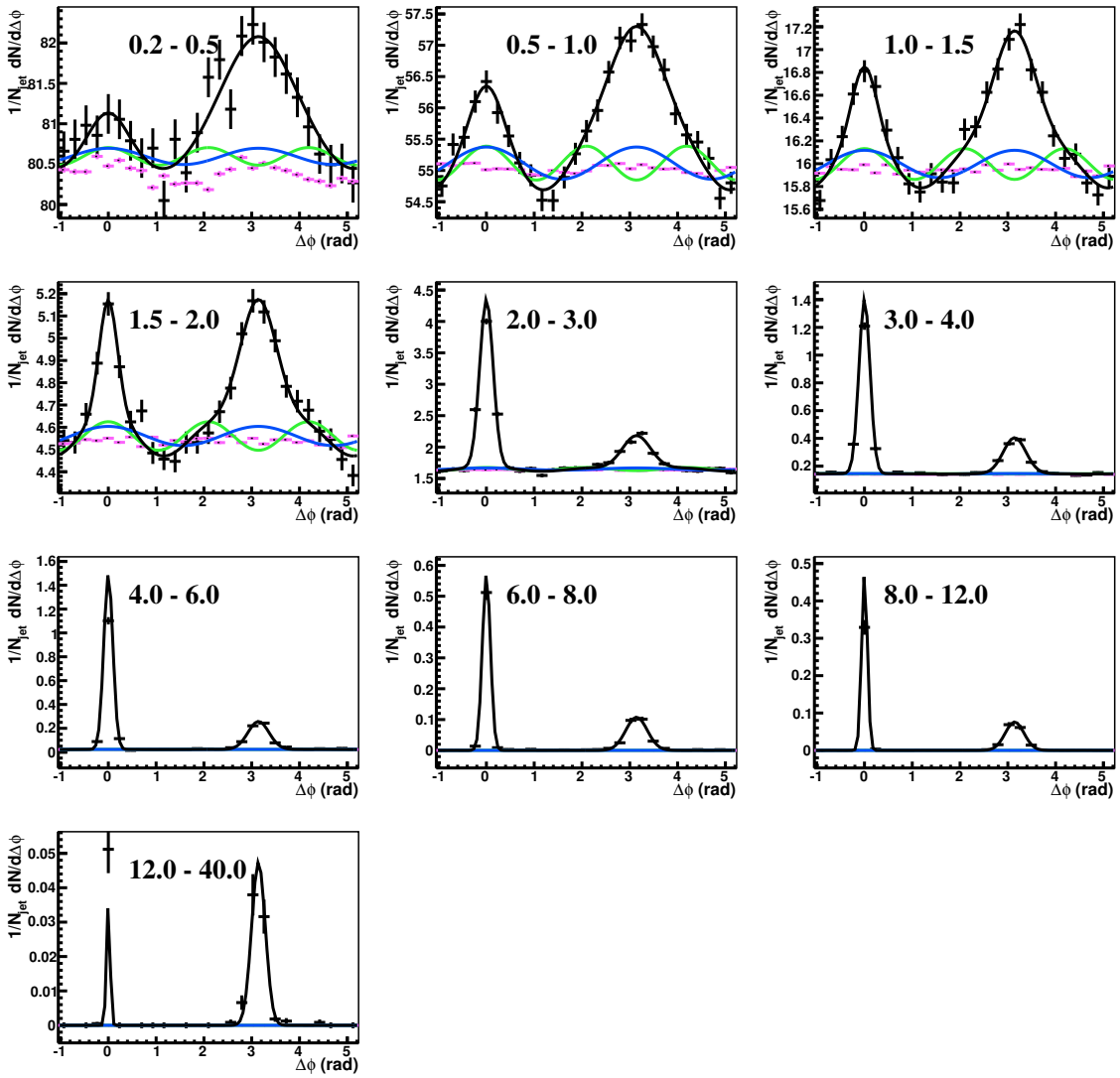

Figure B.10: $\Delta\phi$ correlations in Au+Au for $15 < p_{\mathrm{T}}^{jet,rec} < 20$ GeV/c with the *minimum* v_2 background assumption and nearside yield/width matching. The p_{T}^{assoc} values (in GeV/c) are shown in each panel. The fit to the points (Eq. 4.4) is shown by a black line, the v_2 and v_3 components of the fit are shown in blue and green, respectively. The mixed event background is shown in pink points, scaled up to the background level B.

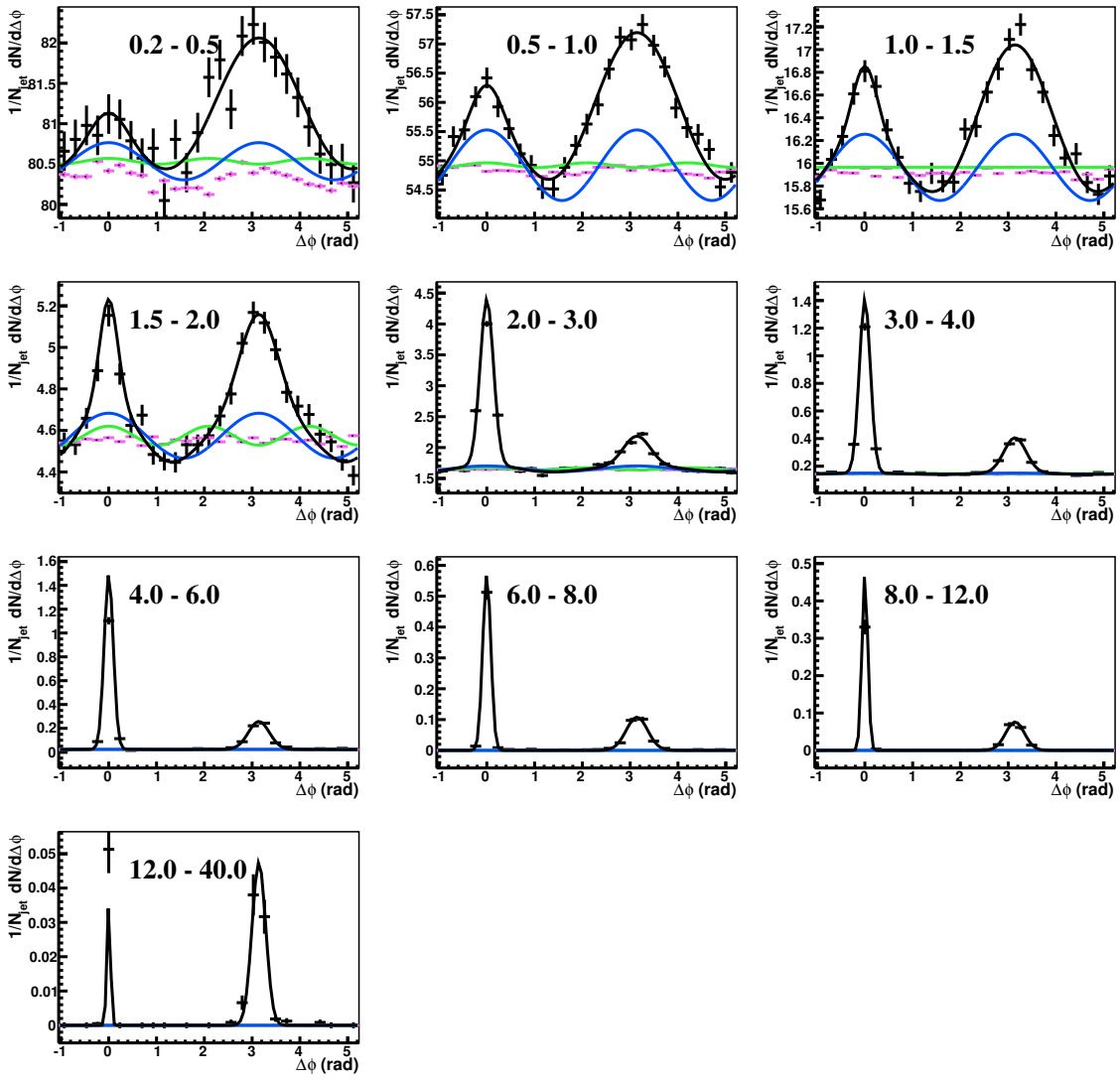

Figure B.11: $\Delta\phi$ correlations in Au+Au for $15 < p_{\mathrm{T}}^{jet,rec} < 20$ GeV/c with the *maximum* v_2 background assumption and nearside yield/width matching. The p_{T}^{assoc} values (in GeV/c) are shown in each panel. The fit to the points (Eq. 4.4) is shown by a black line, the v_2 and v_3 components of the fit are shown in blue and green, respectively. The mixed event background is shown in pink points, scaled up to the background level B.

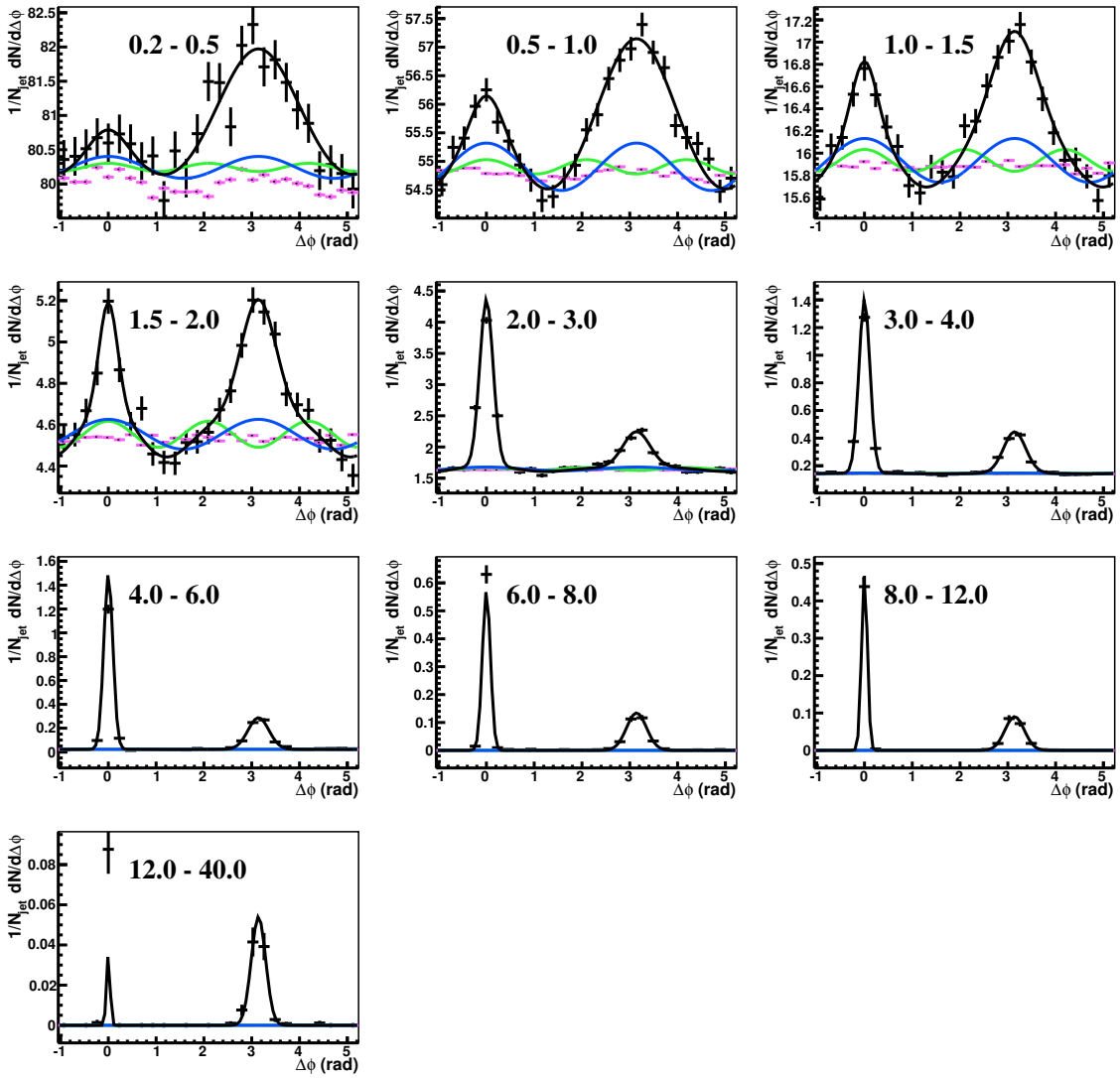

Figure B.12: $\Delta\phi$ correlations in Au+Au for $15 < p_{\mathrm{T}}^{jet,rec} < 20$ GeV/c with the mean v_2 background assumption and nearside yield/width matching *after the* ΔE *shift*. The p_{T}^{assoc} values (in GeV/c) are shown in each panel. The fit to the points (Eq. 4.4) is shown by a black line, the v_2 and v_3 components of the fit are shown in blue and green, respectively. The mixed event background is shown in pink points, scaled up to the background level B.

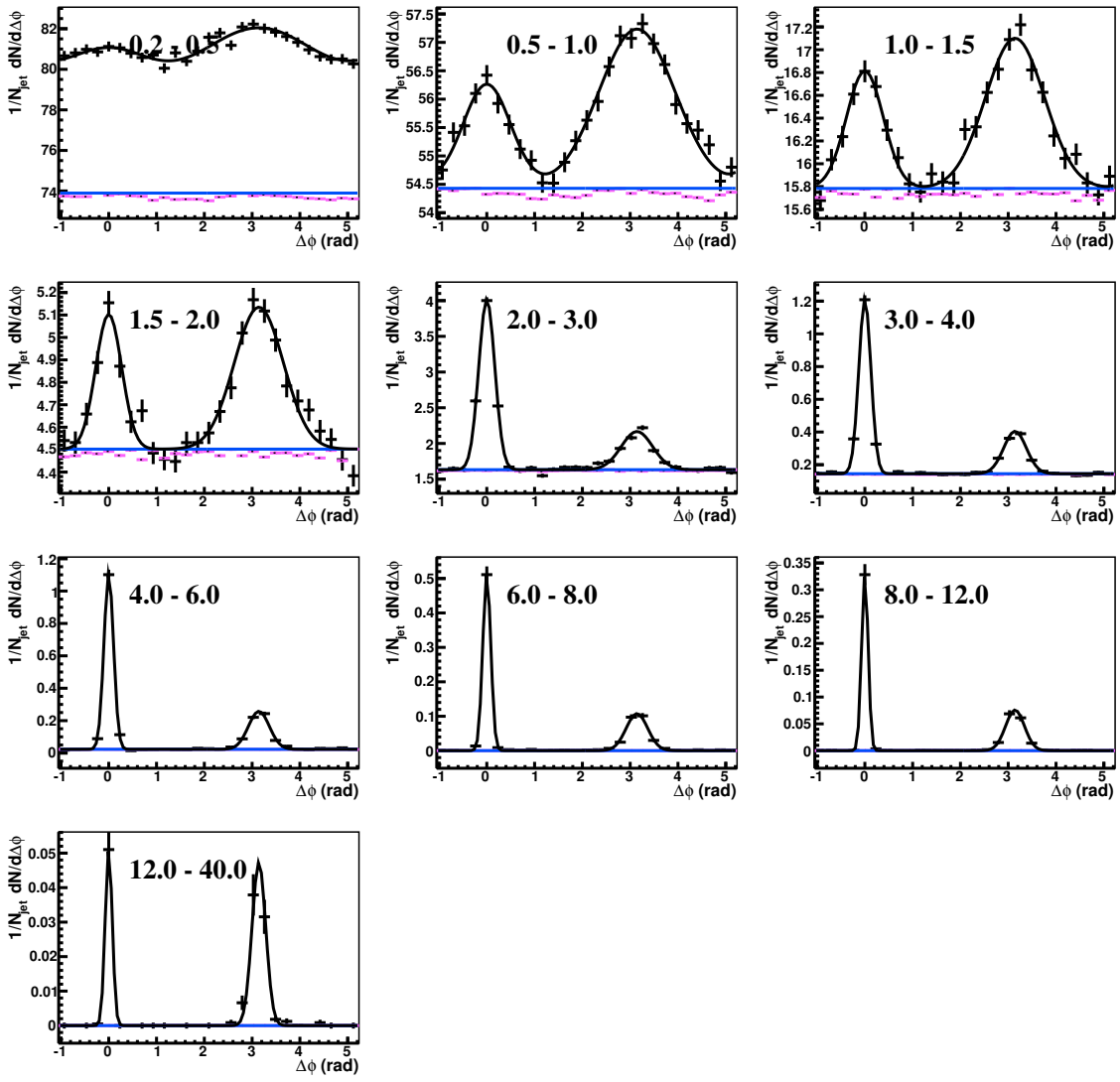

Figure B.13: $\Delta\phi$ correlations in Au+Au for $15 < p_{\mathrm{T}}^{jet,rec} < 20$ GeV/c with the *zero* v_2 background assumption. The p_{T}^{assoc} values (in GeV/c) are shown in each panel. The fit to the points (Eq. 4.4) is shown by a black line, the flat background is shown in blue. The mixed event background is shown in pink points, scaled up to the background level B.

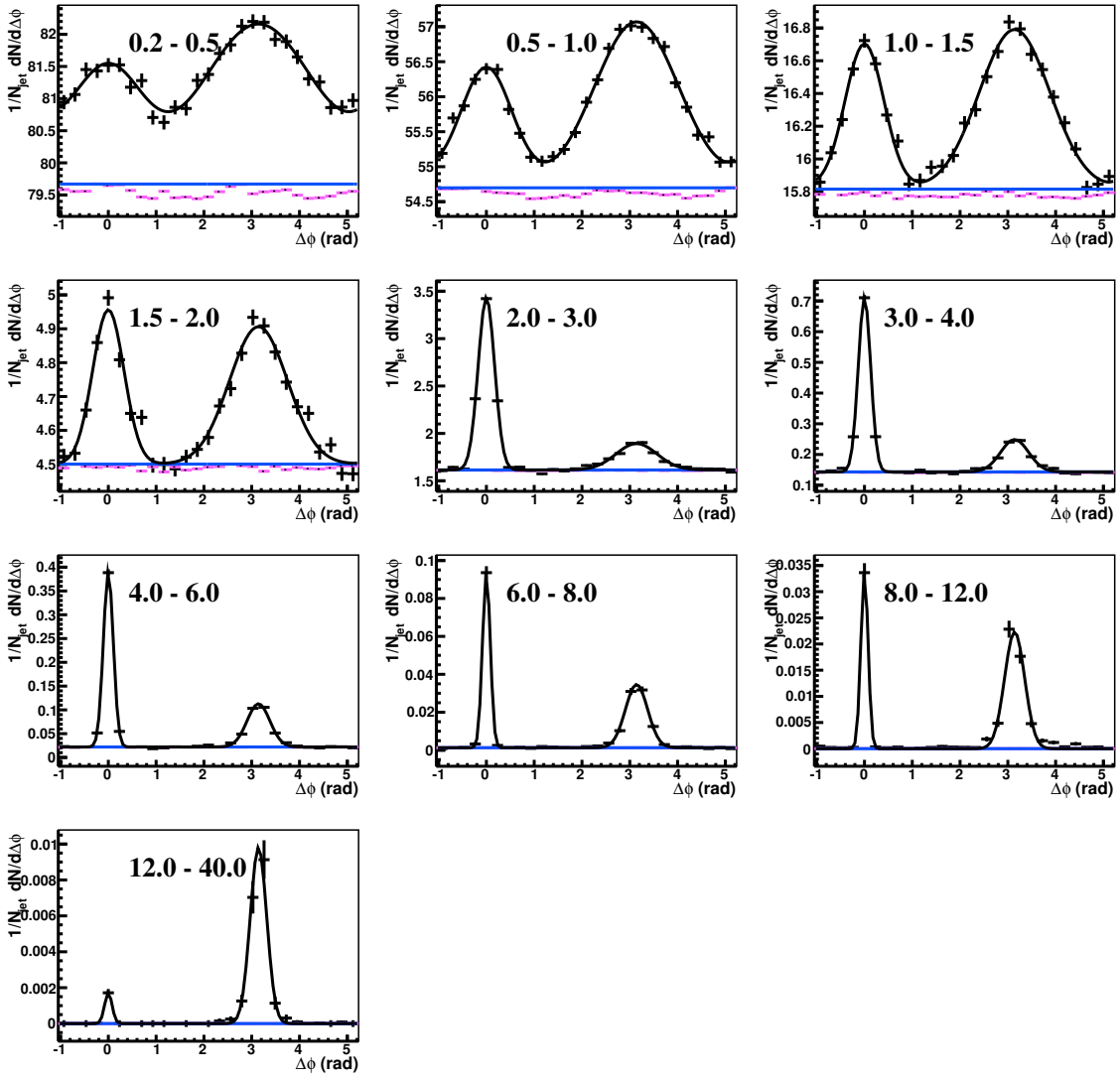

Figure B.14: $\Delta\phi$ correlations in Au+Au for $15 < p_{\mathrm{T}}^{jet,rec} < 20$ GeV/c with the zero v_2 background assumption *after the* ΣD_{AA} *shift*. The p_{T}^{assoc} values (in GeV/c) are shown in each panel. The fit to the points (Eq. 4.4) is shown by a black line, the flat background is shown in blue. The mixed event background is shown in pink points, scaled up to the background level B.

B.3 $20 < p_{\mathrm{T}}^{jet,rec} < 40$ GeV/c

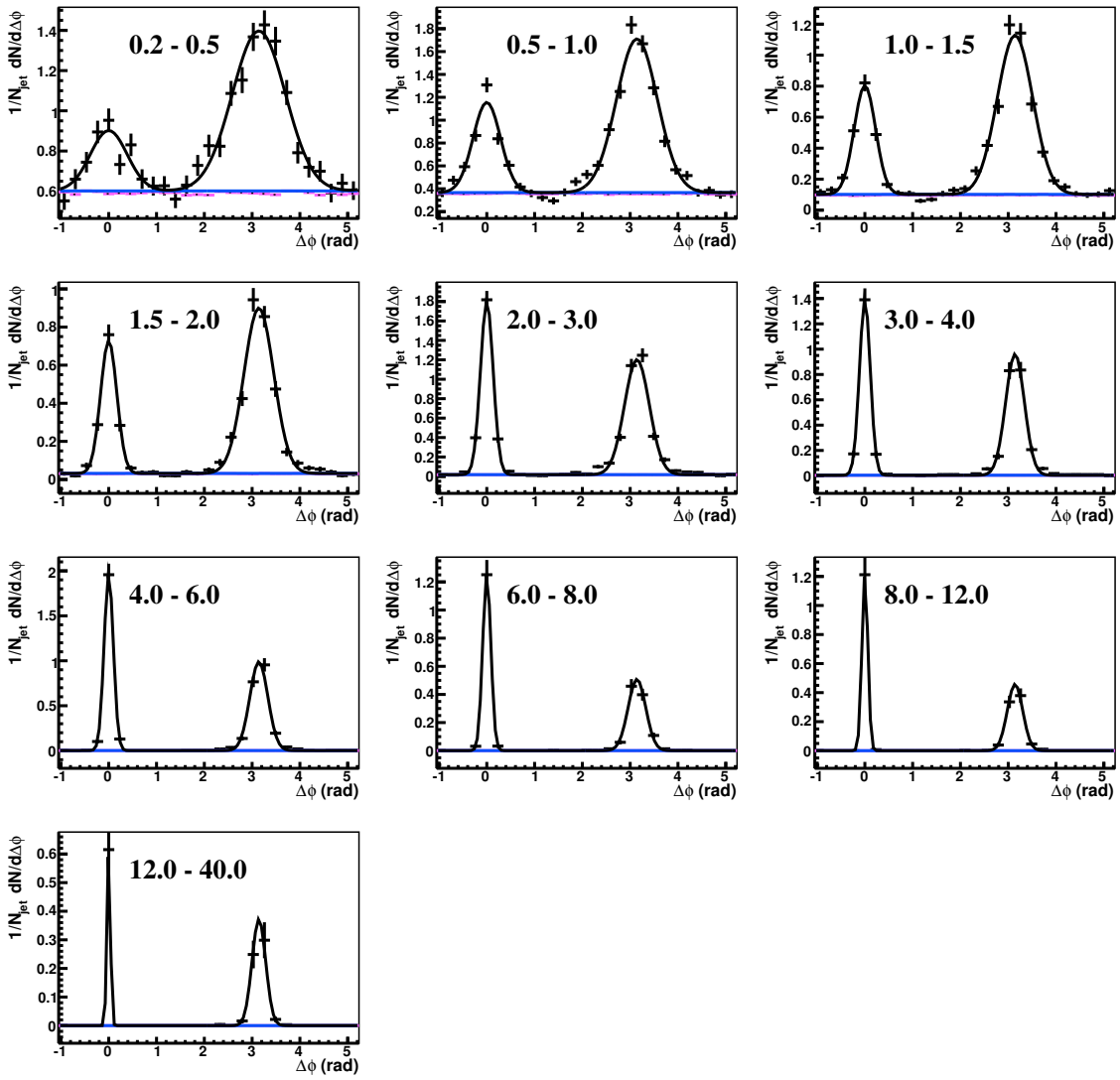

Figure B.15: $\Delta\phi$ correlations in p+p for $20 < p_{\mathrm{T}}^{jet,rec} < 40$ GeV/c. The p_{T}^{assoc} values (in GeV/c) are shown in each panel. The fit to the points (Eq. 4.4) is shown by a black line, the flat background is shown in blue. The mixed event background is shown in pink points, scaled up to the background level B (although the points are mostly obscured by the blue background line).

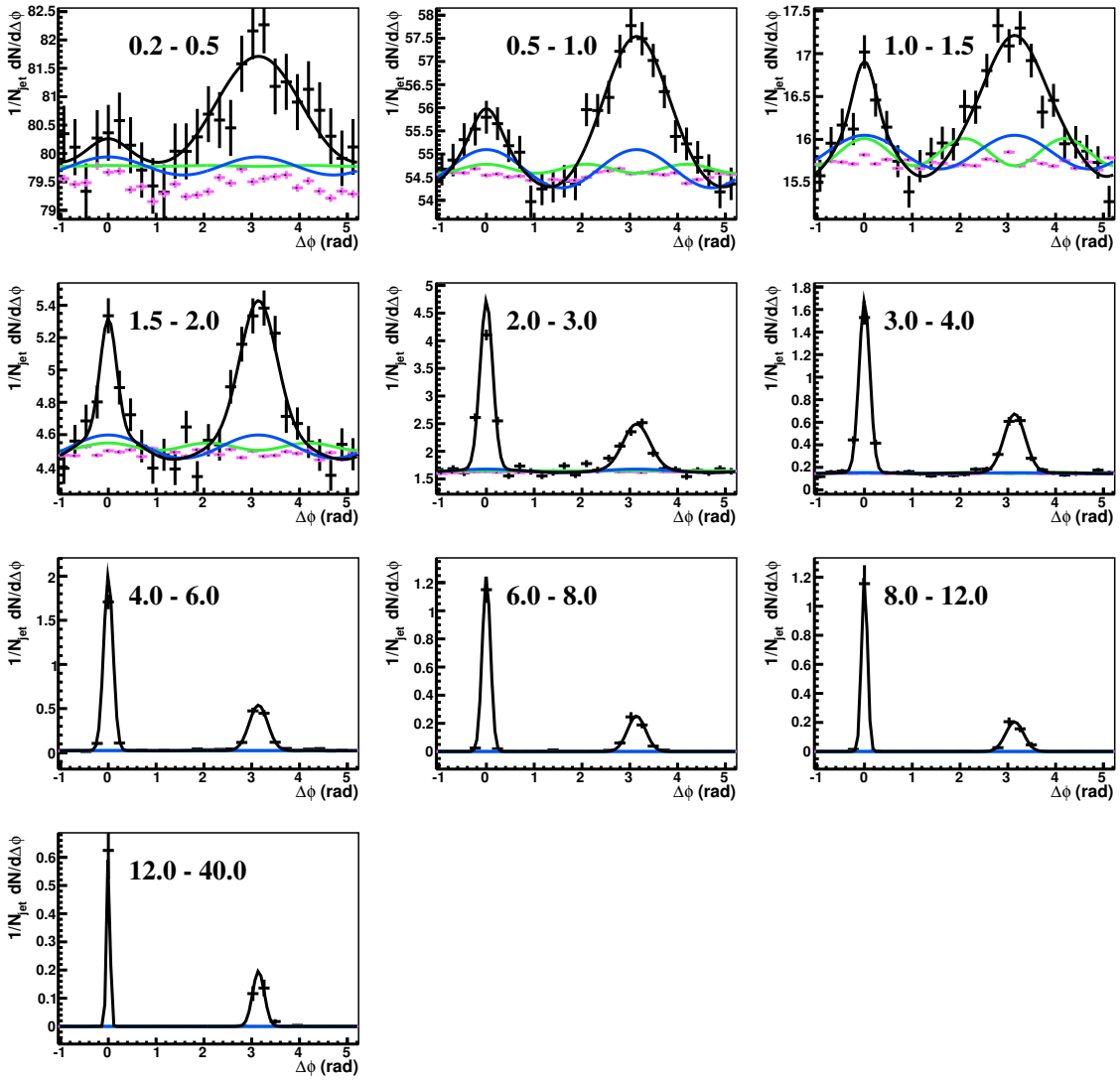

Figure B.16: $\Delta\phi$ correlations in Au+Au for $20 < p_{\mathrm{T}}^{jet,rec} < 40$ GeV/c with the *mean* v_2 background assumption and nearside yield/width matching. The p_{T}^{assoc} values (in GeV/c) are shown in each panel. The fit to the points (Eq. 4.4) is shown by a black line, the v_2 and v_3 components of the fit are shown in blue and green, respectively. The mixed event background is shown in pink points, scaled up to the background level B.

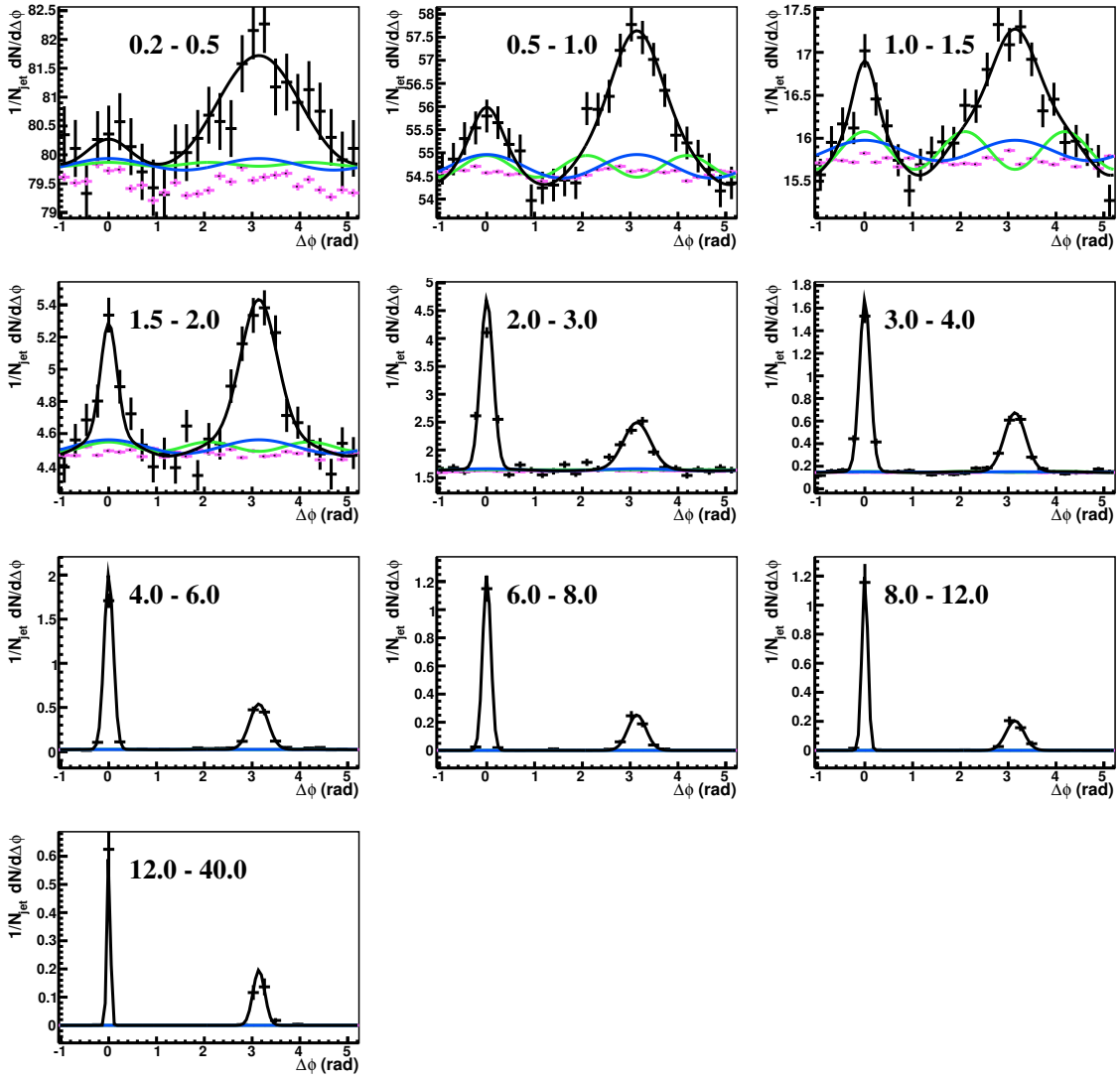

Figure B.17: $\Delta\phi$ correlations in Au+Au for $20 < p_{\mathrm{T}}^{jet,rec} < 40$ GeV/c with the *minimum* v_2 background assumption and nearside yield/width matching. The p_{T}^{assoc} values (in GeV/c) are shown in each panel. The fit to the points (Eq. 4.4) is shown by a black line, the v_2 and v_3 components of the fit are shown in blue and green, respectively. The mixed event background is shown in pink points, scaled up to the background level B.

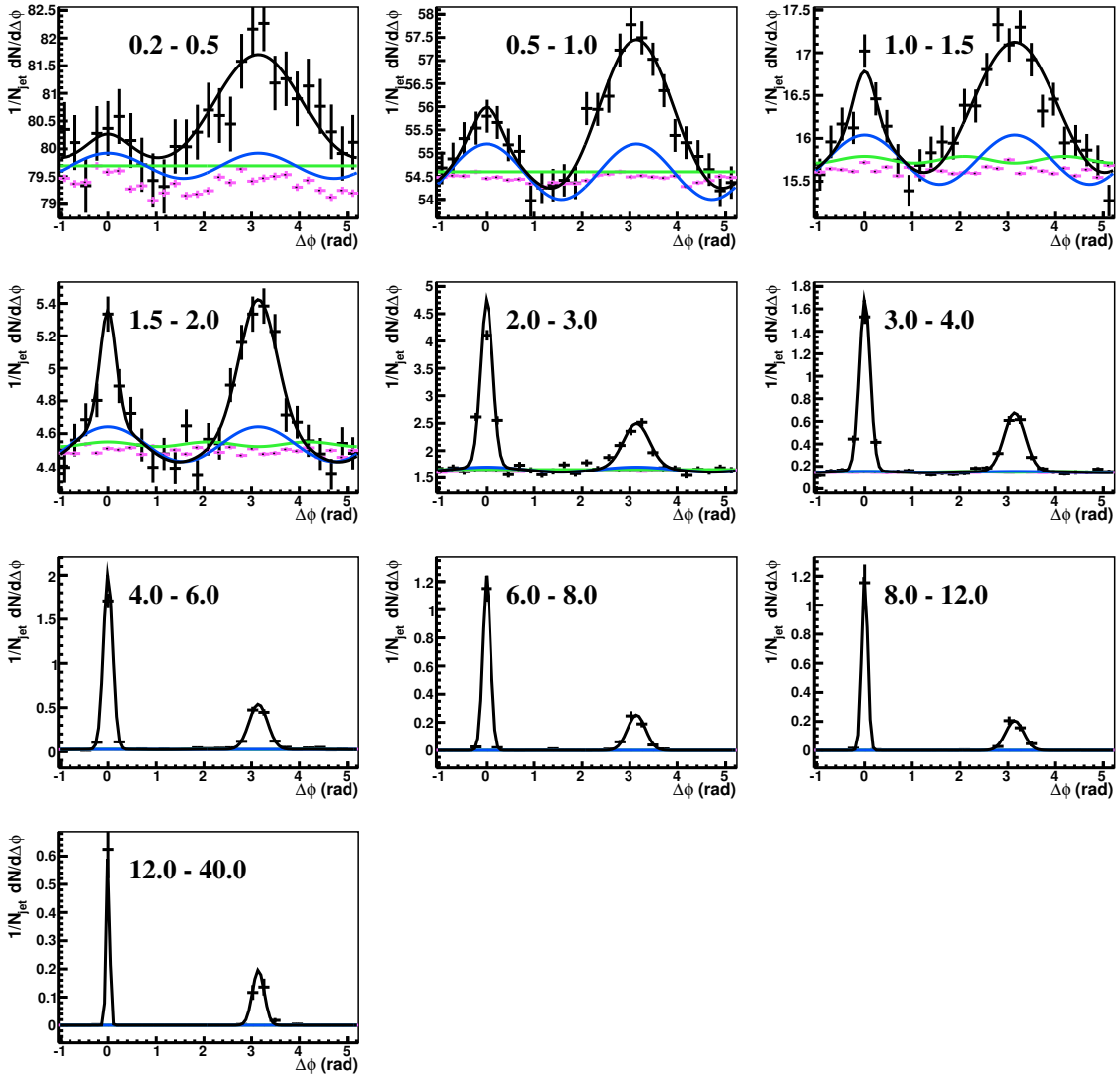

Figure B.18: $\Delta\phi$ correlations in Au+Au for $20 < p_{\mathrm{T}}^{jet,rec} < 40$ GeV/c with the *maximum* v_2 background assumption and nearside yield/width matching. The p_{T}^{assoc} values (in GeV/c) are shown in each panel. The fit to the points (Eq. 4.4) is shown by a black line, the v_2 and v_3 components of the fit are shown in blue and green, respectively. The mixed event background is shown in pink points, scaled up to the background level B.

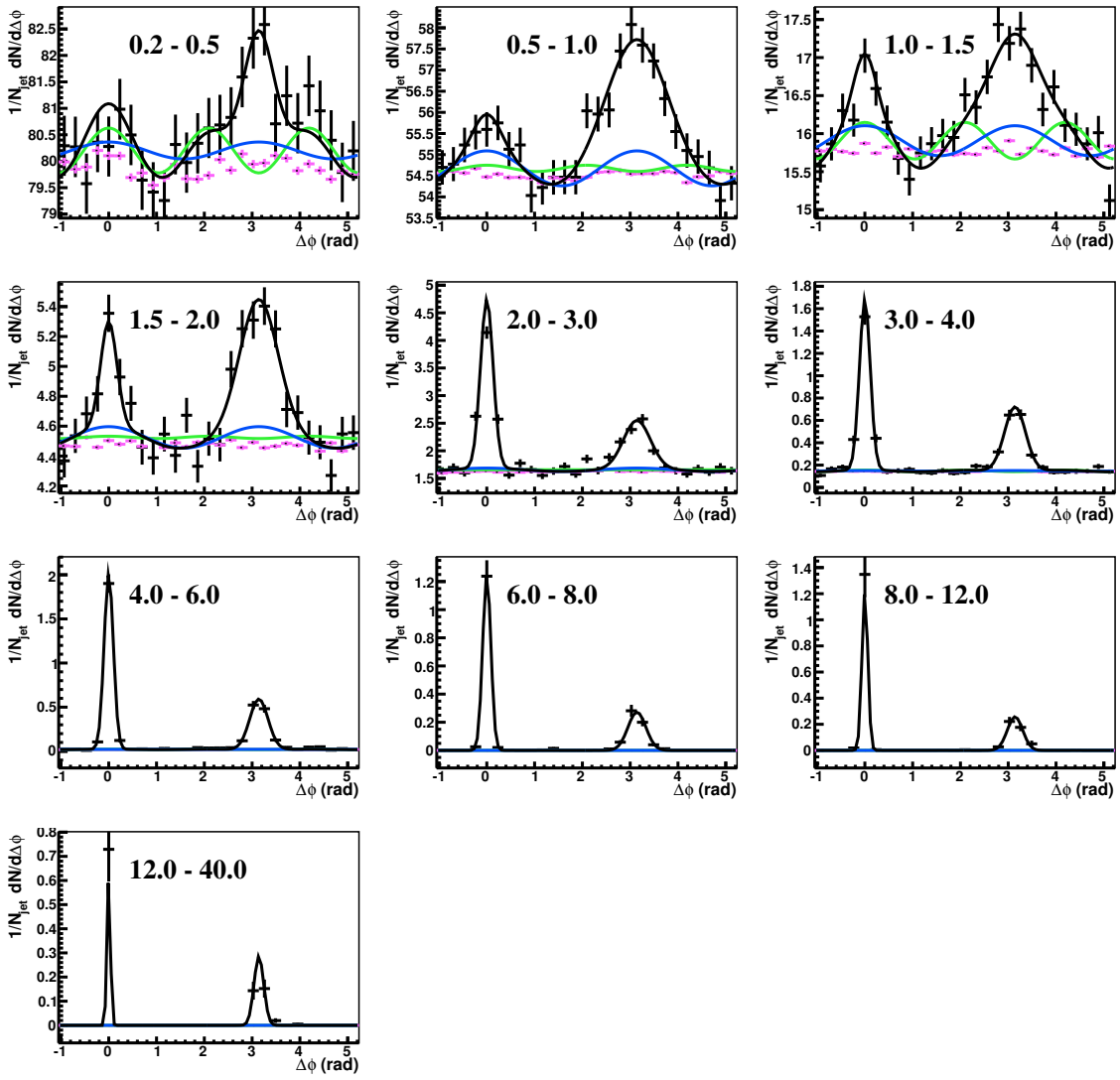

Figure B.19: $\Delta\phi$ correlations in Au+Au for $20 < p_{\mathrm{T}}^{jet,rec} < 40$ GeV/c with the mean v_2 background assumption and nearside yield/width matching *after the* ΔE *shift*. The p_{T}^{assoc} values (in GeV/c) are shown in each panel. The fit to the points (Eq. 4.4) is shown by a black line, the v_2 and v_3 components of the fit are shown in blue and green, respectively. The mixed event background is shown in pink points, scaled up to the background level B.

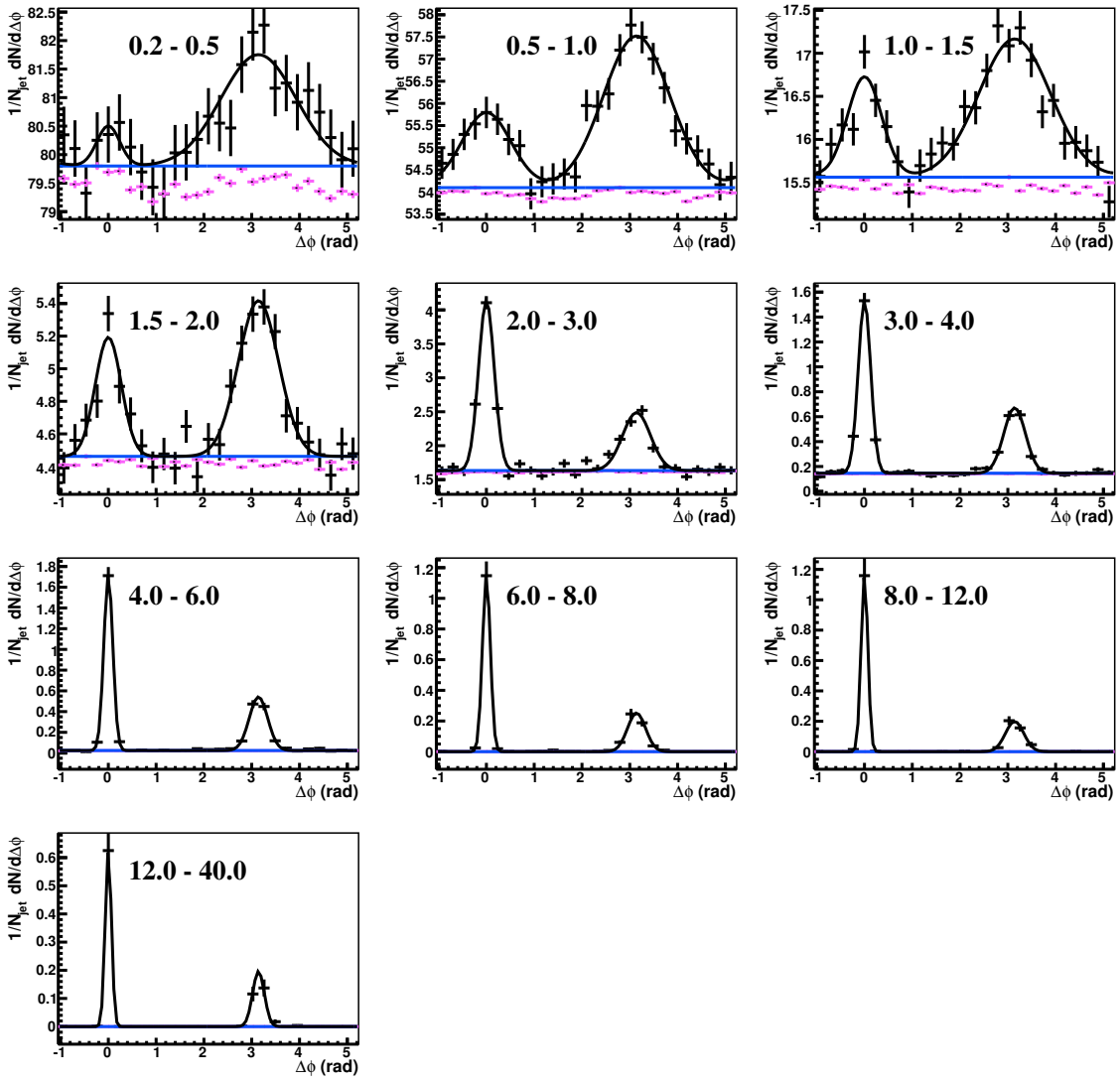

Figure B.20: $\Delta\phi$ correlations in Au+Au for $20 < p_{\mathrm{T}}^{jet,rec} < 40$ GeV/c with the *zero* v_2 background assumption. The p_{T}^{assoc} values (in GeV/c) are shown in each panel. The fit to the points (Eq. 4.4) is shown by a black line, the flat background is shown in blue. The mixed event background is shown in pink points, scaled up to the background level B.

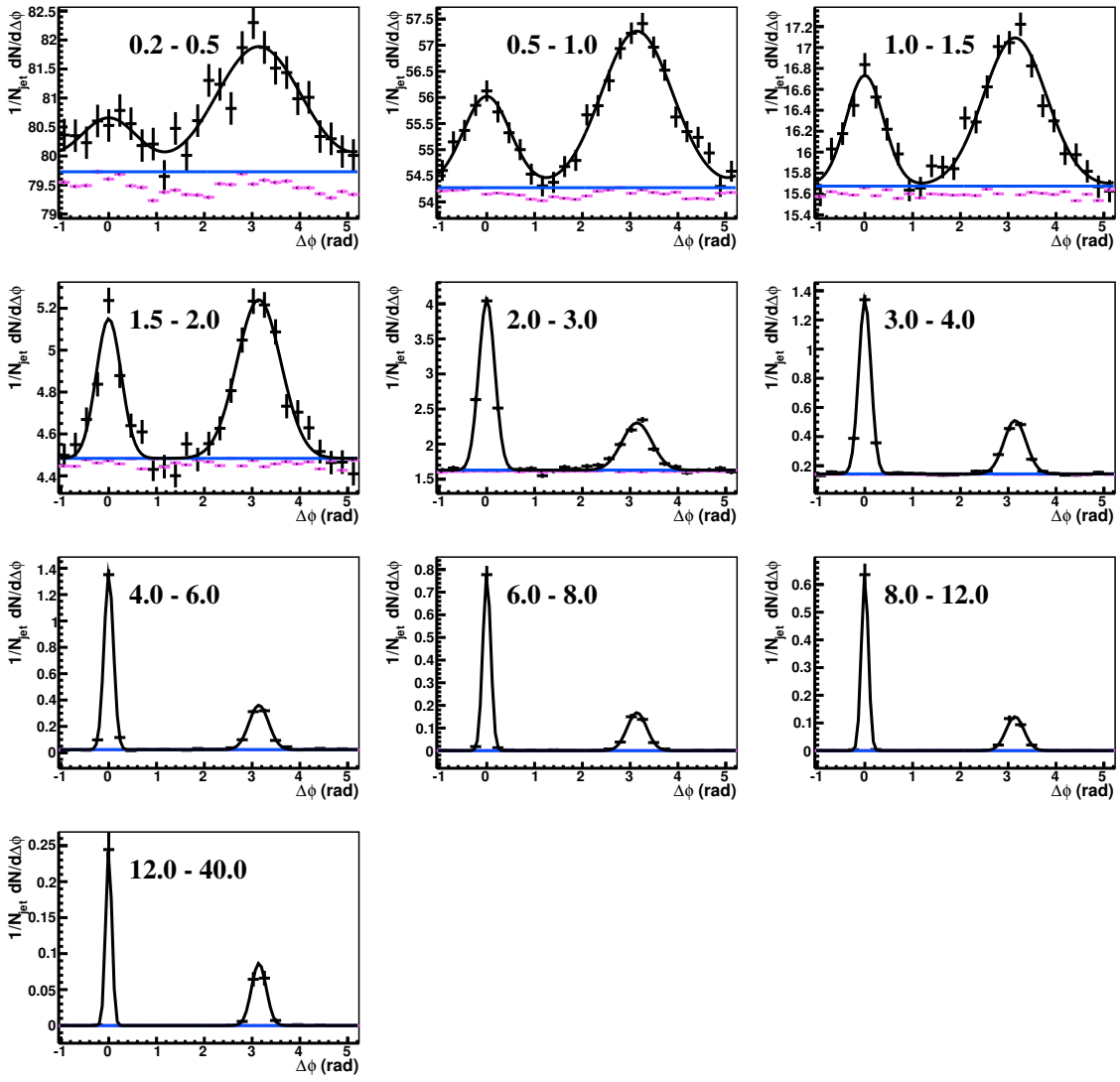

Figure B.21: $\Delta\phi$ correlations in Au+Au for $20 < p_{\mathrm{T}}^{jet,rec} < 40$ GeV/c with the zero v_2 background assumption *after the* ΣD_{AA} *shift*. The p_{T}^{assoc} values (in GeV/c) are shown in each panel. The fit to the points (Eq. 4.4) is shown by a black line, the flat background is shown in blue. The mixed event background is shown in pink points, scaled up to the background level B.

Bibliography

[1] D. Gross and F. Wilczek, *Ultraviolet Behavior of Nonabelian Gauge Theories*, Phys. Rev. Lett. **30**, 1343 (1973).

[2] H. D. Politzer, *Reliable Perturbative Results for Strong Interactions?*, Phys. Rev. Lett. **30**, 1346 (1973).

[3] S. Bethke, *Experimental tests of asymptotic freedom*, Prog. Part. Nucl. Phys. **58**, 351 (2007), `hep-ex/0606035`.

[4] J. Bjorken, *Asymptotic Sum Rules at Infinite Momentum*, Phys. Rev. **179**, 1547 (1969).

[5] M. Breidenbach, J. I. Friedman, H. W. Kendall, *et al.*, *Observed Behavior of Highly Inelastic Electron-Proton Scattering*, Phys. Rev. Lett. **23**, 935 (1969).

[6] J. C. Collins and M. Perry, *Superdense Matter: Neutrons Or Asymptotically Free Quarks?*, Phys. Rev. Lett. **34**, 1353 (1975).

[7] F. Karsch, *Lattice results on QCD thermodynamics*, Nucl. Phys. **A698**, 199 (2002), `hep-ph/0103314`.

[8] A. Bazavov *et al.*, *Equation of state and QCD transition at finite temperature*, Phys. Rev. **D80**, 014504 (2009).

[9] P. Petreczky, *Lattice QCD at non-zero temperature*, J. Phys. **G39**, 093002 (2012), `1203.5320`.

[10] A. Adare *et al.* (PHENIX), *Enhanced production of direct photons in Au+Au collisions at $\sqrt{s_{NN}}$=200 GeV and implications for the initial temperature*, Phys. Rev. Lett. **104**, 132301 (2010), `0804.4168`.

[11] A. Ali and G. Kramer, *Jets and QCD: A Historical Review of the Discovery of the Quark and Gluon Jets and its Impact on QCD*, Eur. Phys. J. **H36**, 245 (2011), `1012.2288`.

[12] B. Abelev *et al.* (STAR), *Longitudinal double-spin asymmetry and cross section for inclusive jet production in polarized proton collisions at $\sqrt{s}$=200 GeV*, Phys. Rev. Lett. **97**, 252001 (2006), `hep-ex/0608030`.

[13] A. Andronic, P. Braun-Munzinger, and J. Stachel, *Hadron production in central nucleus-nucleus collisions at chemical freeze-out*, Nucl. Phys. **A772**, 167 (2006), nucl-th/0511071.

[14] B. Alver *et al.* (PHOBOS), *System size, energy, pseudorapidity, and centrality dependence of elliptic flow*, Phys. Rev. Lett. **98**, 242302 (2007), nucl-ex/0610037.

[15] W. Broniowski, P. Bozek, and M. Rybczynski, *Fluctuating initial conditions in heavy-ion collisions from the Glauber approach*, Phys. Rev. **C76**, 054905 (2007), 0706.4266.

[16] G.-Y. Qin, H. Petersen, S. A. Bass, *et al.*, *Translation of collision geometry fluctuations into momentum anisotropies in relativistic heavy-ion collisions*, Phys. Rev. **C82**, 064903 (2010), 1009.1847.

[17] S. A. Voloshin, A. M. Poskanzer, and R. Snellings, *Collective Phenomena in Non-Central Nuclear Collisions*, SpringerMaterials - The Landolt-Börnstein Database **23**, 293 (2010), 0809.2949.

[18] C. Adler *et al.* (STAR), *Azimuthal anisotropy and correlations in the hard scattering regime at RHIC*, Phys. Rev. Lett. **90**, 032301 (2003), nucl-ex/0206006.

[19] S. Voloshin and Y. Zhang, *Flow study in relativistic nuclear collisions by Fourier expansion of Azimuthal particle distributions*, Z. Phys. **C70**, 665 (1996), hep-ph/9407282.

[20] A. P. Mishra, R. K. Mohapatra, P. S. Saumia, *et al.*, *Super-horizon fluctuations and acoustic oscillations in relativistic heavy-ion collisions*, Phys. Rev. **C77**, 064902 (2008), 0711.1323.

[21] P. Sorensen, *Implications of space-momentum correlations and geometric fluctuations in heavy-ion collisions*, J. Phys. **G37**, 094011 (2010), 1002.4878.

[22] B. Alver and G. Roland, *Collision geometry fluctuations and triangular flow in heavy-ion collisions*, Phys. Rev. **C81**, 054905 (2010), 1003.0194.

[23] A. Adare *et al.* (PHENIX), *Measurements of Higher-Order Flow Harmonics in Au+Au Collisions at* $\sqrt{s_{NN}}$ *= 200 GeV*, Phys. Rev. Lett. **107**, 252301 (2011), 1105.3928.

[24] K. Aamodt *et al.* (ALICE), *Higher harmonic anisotropic flow measurements of charged particles in Pb-Pb collisions at* $\sqrt{s_{NN}}$ *= 2.76 TeV*, Phys. Rev. Lett. **107**, 032301 (2011), 1105.3865.

[25] K. Aamodt *et al.* (ALICE), *Harmonic decomposition of two-particle angular correlations in Pb-Pb collisions at $\sqrt{s_{NN}}$ = 2.76 TeV*, Phys. Lett. **B708**, 249 (2012), 1109.2501.

[26] A. Adare *et al.* (PHENIX), *Scaling properties of azimuthal anisotropy in Au + Au and Cu + Cu collisions at $\sqrt{s_{NN}}$ = 200 GeV*, Phys. Rev. Lett. **98**, 162301 (2007), nucl-ex/0608033.

[27] B. Schenke, S. Jeon, and C. Gale, *Higher flow harmonics from (3+1)D event-by-event viscous hydrodynamics*, Phys. Rev. **C85**, 024901 (2012), 1109.6289.

[28] P. Kovtun, D. Son, and A. Starinets, *Viscosity in strongly interacting quantum field theories from black hole physics*, Phys. Rev. Lett. **94**, 111601 (2005), hep-th/0405231.

[29] J. Adams *et al.* (STAR), *Transverse momentum and collision energy dependence of high p_T hadron suppression in Au + Au collisions at ultrarelativistic energies*, Phys. Rev. Lett. **91**, 172302 (2003), nucl-ex/0305015.

[30] J. Adams *et al.* (STAR), *Evidence from d + Au measurements for final state suppression of high p_T hadrons in Au+Au collisions at RHIC*, Phys. Rev. Lett. **91**, 072304 (2003), nucl-ex/0306024.

[31] C. Adler *et al.* (STAR), *Disappearance of back-to-back high p_T hadron correlations in central Au + Au collisions at $\sqrt{s_{NN}}$ = 200 GeV*, Phys. Rev. Lett. **90**, 082302 (2003), nucl-ex/0210033.

[32] S. Catani, Y. L. Dokshitzer, M. Seymour, *et al.*, *Longitudinally invariant K_t clustering algorithms for hadron-hadron collisions*, Nucl. Phys. **B406**, 187 (1993).

[33] S. D. Ellis and D. E. Soper, *Successive combination jet algorithm for hadron collisions*, Phys. Rev. **D48**, 3160 (1993), hep-ph/9305266.

[34] M. Cacciari, G. P. Salam, and G. Soyez, *The Anti-k_t jet clustering algorithm*, JHEP **04**, 063 (2008), 0802.1189.

[35] Y. L. Dokshitzer, G. Leder, S. Moretti, *et al.*, *Better jet clustering algorithms*, JHEP **08**, 001 (1997), hep-ph/9707323.

[36] M. Wobisch and T. Wengler, *Hadronization corrections to jet cross-sections in deep inelastic scattering* (1998), hep-ph/9907280.

[37] M. Cacciari and G. P. Salam, *Dispelling the N^3 myth for the k_t jet-finder*, Phys. Lett. **B641**, 57 (2006), hep-ph/0512210.

[38] M. Cacciari, G. P. Salam, and G. Soyez, *The Catchment Area of Jets*, JHEP **04**, 005 (2008), 0802.1188.

[39] M. Cacciari, G. P. Salam, and G. Soyez, *FastJet User Manual*, Eur. Phys. J. **C72**, 1896 (2012), 1111.6097.

[40] H. Hahn, E. Forsyth, H. Foelsche, *et al.*, *The RHIC design overview*, Nucl. Instrum. Meth. **A499**, 245 (2003).

[41] K. Ackermann *et al.* (STAR), *STAR detector overview*, Nucl. Instrum. Meth. **A499**, 624 (2003).

[42] M. Anderson, J. Berkovitz, W. Betts, *et al.*, *The Star time projection chamber: A Unique tool for studying high multiplicity events at RHIC*, Nucl. Instrum. Meth. **A499**, 659 (2003), nucl-ex/0301015.

[43] M. Beddo *et al.* (STAR), *The STAR barrel electromagnetic calorimeter*, Nucl. Instrum. Meth. **A499**, 725 (2003).

[44] K. Ackermann, F. Bieser, F. Brady, *et al.*, *The Forward time projection chamber (FTPC) in STAR*, Nucl. Instrum. Meth. **A499**, 713 (2003), nucl-ex/0211014.

[45] C. Adler, A. Denisov, E. Garcia, *et al.*, *The RHIC zero-degree calorimeters*, Nucl. Instrum. Meth. **A499**, 433 (2003).

[46] G. Wang, *Correlations Relative to the Reaction Plane at the Relaticistic Heavy Ion Collider Based on Transverse Deflection of Spectator Neutrons*, Ph.D. thesis, Kent State University (2006).

[47] C. Amsler *et al.* (Particle Data Group), *Review of Particle Physics*, Phys. Lett. **B667**, 297 (2008).

[48] A. Pikin, J. G. Alessi, E. N. Beebe, *et al.*, *RHIC EBIS: basics of design and status of commissioning*, Journal of Instrumentation **5(09)**, C09003 (2010).

[49] B. Abelev *et al.* (STAR), *Azimuthal Charged-Particle Correlations and Possible Local Strong Parity Violation*, Phys. Rev. Lett. **103**, 251601 (2009), 0909.1739.

[50] M. Aggarwal *et al.* (STAR), *An Experimental Exploration of the QCD Phase Diagram: The Search for the Critical Point and the Onset of De-confinement* (2010), 1007.2613.

[51] L. Adamczyk *et al.* (STAR), *Observation of an Energy-Dependent Difference in Elliptic Flow between Particles and Antiparticles in Relativistic Heavy Ion Collisions*, Phys. Rev. Lett. **110**, 142301 (2013).

[52] L. Adamczyk *et al.* (STAR), *Elliptic flow of identified hadrons in Au+Au collisions at* $\sqrt{s_{NN}}$ *= 7.7 – 62.4 GeV*, Phys. Rev. **C88**, 014902 (2013).

[53] J. Dunlop, *2007 Au+Au run (run 7) Trigger FAQ*, http://www.star.bnl.gov/protected/common/common2007/trigger2007/triggers2007.html.

[54] J. Dunlop, *2006 p+p run (run 6) Trigger FAQ*, http://www.star.bnl.gov/protected/common/common2006/trigger2006/triggers2006.html.

[55] T. Renk, *Through the blackness - high p_T hadrons probing the central region of 200 AGeV Au-Au collisions*, Phys. Rev. **C74**, 024903 (2006), hep-ph/0602045.

[56] K. Eskola, H. Honkanen, C. Salgado, *et al.*, *The Fragility of high-p_T hadron spectra as a hard probe*, Nucl. Phys. **A747**, 511 (2005), hep-ph/0406319.

[57] A. Dainese, C. Loizides, and G. Paic, *Leading-particle suppression in high energy nucleus-nucleus collisions*, Eur. Phys. J. **C38**, 461 (2005), hep-ph/0406201.

[58] T. Renk and K. J. Eskola, *Prospects of medium tomography using back-to-back hadron correlations*, Phys. Rev. **C75**, 054910 (2007), hep-ph/0610059.

[59] A. Drees, H. Feng, and J. Jia, *Medium induced jet absorption at RHIC*, Phys. Rev. **C71**, 034909 (2005), nucl-th/0310044.

[60] T. Renk, *Biased Showers - a common conceptual Framework for the Interpretation of High P_T Observables in Heavy-Ion Collisions*, submitted to Phys. Rev. C (2012), 1212.0646.

[61] M. Cacciari and G. P. Salam, *Pileup subtraction using jet areas*, Phys. Lett. **B659**, 119 (2008), 0707.1378.

[62] M. van Leeuwen, *v_2 overview Au+Au collisions*, http://www.star.bnl.gov/protected/jetcorr/mvl/v2_compare/auau_compare.html.

[63] J. Adams *et al.* (STAR), *Azimuthal anisotropy in Au+Au collisions at $\sqrt{s_{NN}}$ = 200 GeV*, Phys. Rev. **C72**, 014904 (2005), nucl-ex/0409033.

[64] N. Borghini, P. M. Dinh, and J.-Y. Ollitrault, *Flow analysis from multiparticle azimuthal correlations*, Phys. Rev. **C64**, 054901 (2001), nucl-th/0105040.

[65] L. Adamczyk *et al.* (STAR), *Third Harmonic Flow of Charged Particles in Au+Au Collisions at $\sqrt{s_{NN}}$ = 200 GeV*, Phys. Rev. **C88**, 014904 (2013), 1301.2187.

[66] M. Betancourt, A. Hoffman, A. Kocoloski, *et al.*, *2006 BEMC Tower Calibration Report*, STAR Technical Document (2009).

[67] T. Cormier, A. Pavlinov, M. Rykov, *et al.*, *STAR barrel electromagnetic calorimeter absolute calibration using 'minimum ionizing particles' from collisions at RHIC*, Nucl. Instrum. Meth. **A483**, 734 (2002), hep-ex/0107081.

[68] T. Renk, *Parton shower evolution in a 3-d hydrodynamical medium*, Phys. Rev. **C78**, 034908 (2008), 0806.0305.

[69] T. Renk, *A Comparison study of medium-modified QCD shower evolution scenarios*, Phys. Rev. **C79**, 054906 (2009), 0901.2818.

[70] T. Renk, *Pathlength dependence of energy loss within in-medium showers*, Phys. Rev. **C83**, 024908 (2011), 1010.4116.

[71] T. Renk, *Using Hard Dihadron Correlations to constrain Elastic Energy Loss*, Phys. Rev. **C84**, 067902 (2011), 1110.2313.

[72] F. Loshaj and D. E. Kharzeev, *LPM effect as the origin of the jet fragmentation scaling in heavy ion collisions*, Int. J. Mod. Phys. **E21**, 1250088 (2012), 1111.0493.

[73] T. Renk, *Theoretical assessment of jet-hadron correlations*, Phys. Rev. **C87**, 024905 (2013), 1210.1330.

[74] D. E. Kharzeev and F. Loshaj, *Jet energy loss and fragmentation in heavy ion collisions* (2012), 1212.5857.

[75] A. Majumder and M. Van Leeuwen, *The Theory and Phenomenology of Perturbative QCD Based Jet Quenching*, Prog. Part. Nucl. Phys. **66**, 41 (2011), 1002.2206.

[76] X.-N. Wang, *Jet quenching and azimuthal anisotropy of large p_T spectra in noncentral high-energy heavy ion collisions*, Phys. Rev. **C63**, 054902 (2001), nucl-th/0009019.

[77] A. M. Poskanzer and S. A. Voloshin, *Methods for analyzing anisotropic flow in relativistic nuclear collisions*, Phys. Rev. **C58**, 1671 (1998), nucl-ex/9805001.

[78] T. Sjöstrand, S. Mrenna, and P. Skands, *PYTHIA 6.4 Physics and Manual*, JHEP **05**, 026 (2006), hep-ph/0603175.

[79] T. Sjöstrand, S. Mrenna, and P. Skands, *A Brief Introduction to PYTHIA 8.1*, Comput. Phys. Commun. **178**, 852 (2008), 0710.3820.

[80] B. Abelev *et al.* (STAR), *Systematic Measurements of Identified Particle Spectra in pp, d^+ Au and Au+Au Collisions from STAR*, Phys. Rev. **C79**, 034909 (2009), 0808.2041.

[81] R. S. Bhalerao and J.-Y. Ollitrault, *Eccentricity fluctuations and elliptic flow at RHIC*, Phys. Lett. **B641**, 260 (2006), nucl-th/0607009.

[82] J.-Y. Ollitrault, A. M. Poskanzer, and S. A. Voloshin, *Effect of flow fluctuations and nonflow on elliptic flow methods*, Phys. Rev. **C80**, 014904 (2009), 0904.2315.

[83] J. Alme, Y. Andres, H. Appelshauser, *et al.*, *The ALICE TPC, a large 3-dimensional tracking device with fast readout for ultra-high multiplicity events*, Nucl. Instrum. Meth. **A622**, 316 (2010).

[84] K. Aamodt *et al.* (ALICE), *Elliptic flow of charged particles in Pb-Pb collisions at 2.76 TeV*, Phys. Rev. Lett. **105**, 252302 (2010), 1011.3914.

[85] K. Aamodt *et al.* (ALICE), *Centrality dependence of the charged-particle multiplicity density at mid-rapidity in Pb-Pb collisions at* $\sqrt{s_{NN}}$ *= 2.76 TeV*, Phys. Rev. Lett. **106**, 032301 (2011), 1012.1657.

[86] S. A. Voloshin, A. M. Poskanzer, A. Tang, *et al.*, *Elliptic flow in the Gaussian model of eccentricity fluctuations*, Phys. Lett. **B659**, 537 (2008), 0708.0800.

[87] B. Alver, B. Back, M. Baker, *et al.*, *Importance of correlations and fluctuations on the initial source eccentricity in high-energy nucleus-nucleus collisions*, Phys. Rev. **C77**, 014906 (2008), 0711.3724.

[88] G. Aad *et al.* (ATLAS), *Observation of a Centrality-Dependent Dijet Asymmetry in Lead-Lead Collisions at* $\sqrt{s_{NN}}$ *= 2.76 TeV with the ATLAS Detector at the LHC*, Phys. Rev. Lett. **105**, 252303 (2010), 1011.6182.

[89] S. Chatrchyan *et al.* (CMS), *Observation and studies of jet quenching in PbPb collisions at nucleon-nucleon center-of-mass energy = 2.76 TeV*, Phys. Rev. **C84**, 024906 (2011), 1102.1957.

[90] G. Aad *et al.* (ATLAS), *Measurement of the Azimuthal Angle Dependence of Inclusive Jet Yields in Pb+Pb Collisions at* $\sqrt{s_{NN}}$*= 2.76 TeV with the ATLAS detector*, submitted to Phys. Rev. Lett. (2013), 1306.6469.

[91] G. Aad *et al.* (ATLAS), *Measurement of the jet radius and transverse momentum dependence of inclusive jet suppression in lead-lead collisions at* $\sqrt{s_{NN}}$*= 2.76 TeV with the ATLAS detector*, Phys. Lett. **B719**, 220 (2013), 1208.1967.

[92] S. Chatrchyan *et al.* (CMS), *Azimuthal anisotropy of charged particles at high transverse momenta in PbPb collisions at* $\sqrt{s_{NN}}$ *= 2.76 TeV*, Phys. Rev. Lett. **109**, 022301 (2012), 1204.1850.

[93] J. Bielcikova, *Latest results on spectra, correlations and jets from STAR*, http://ipht.cea.fr/Pisp/francois.gelis/Workshops/Trento2013/Talks/Bielcikova.pptx (2013), talk at h3QCD.

[94] R. Reed (ALICE), *Full Jet Reconstruction in 2.76 TeV pp and Pb-Pb collisions in the ALICE experiment*, proceedings of HQ 2012, to be published (2013), 1304.5945.

[95] S. Chatrchyan *et al.* (CMS), *Studies of jet quenching using isolated-photon+jet correlations in PbPb and pp collisions at* $\sqrt{s_{NN}}$*=2.76 TeV*, Phys. Lett. **B718**, 773 (2013), 1205.0206.

[96] M. Nguyen (CMS), *b-jet Identification in PbPb Collisions with CMS*, Nucl. Phys. **A904-905**, 705c (2013), 1211.5285.

[97] A. Adare *et al.* (PHENIX), *Medium modification of jet fragmentation in Au+Au collisions at* $\sqrt{s_{NN}}$ *= 200 GeV measured in direct photon-hadron correlations*, accepted by Phys. Rev. Lett. (2012), 1212.3323.

[98] M. B. Tonjes, *Inclusive jet and charged hadron nuclear modification factors in PbPb collisions at 2.76 TeV with CMS*, Nucl. Phys. A **904905(0)**, 713c (2013).

[99] A. Angerami, *Measurements of Jet Suppression with ATLAS*, Nucl. Phys. A **904905(0)**, 709c (2013).

[100] A. Timmins, *Primary track and V0 Efficiencies in p+p 200 GeV collisions*, http://www.star.bnl.gov/protected/lfspectra/atimmins/pp200GeV/ppJets/Efficiencies/page.html.

[101] L. Huo, *In-Jet Tracking Efficiency Analysis for the STAR Time Projection Chamber in Polarized Proton-Proton Collisions at* $\sqrt{s}$ *= 200GeV*, Master's thesis, Texas A&M University (2011).

[102] M. Horner, *Efficiency Parameterisations for RIV*, http://www.star.bnl.gov/protected/highpt/mhorner/RIVEfficiencies.shtml.

[103] M. Horner, *Systematic Studies of Low- and Intermediate-*p_T *Correlated Angular Distributions in Au+Au Collisions at* $\sqrt{s_{NN}}$ *= 200 GeV from the STAR Experiment*, Ph.D. thesis, University of Cape Town (2007).

[104] J. Dunlop, *200 GeV FAQ*, http://www.star.bnl.gov/protected/common/common2004/trigger2004/200gev/200gevFaq.html.

[105] A. Timmins, *Centrality in Year 7 Au+Au 200 GeV*, http://www.star.bnl.gov/protected/lfspectra/atimmins/AuAu200GeV/Centrality/page.html.